國立臺灣大學工學院分子科學與技術國際研究生博士學位學程

博士論文

International Graduate Program of Molecular Science and Technology

College of Engineering

National Taiwan University

Doctoral Dissertation

碲化銅中增強的波動狀電荷密度波序化促進電子的加速與輕化

The Growing Charge-Density-Wave Order in CuTe Lightens and Speeds up Electrons

汪奕達

I-Ta Wang

指導教授: 陳俊維 博士
朱明文 博士

Advisor: Chun-Wei Chen, Ph.D.
Ming-Wen Chu, Ph.D.

中華民國 113 年 12 月

December 2024

doi:10.6342/NTU202404787

國立臺灣大學博士學位論文
口試委員會審定書

PhD DISSERTATION ACCEPTANCE CERTIFICATE
NATIONAL TAIWAN UNIVERSITY

The Growing Charge-Density-Wave Order in CuTe Lightens and Speeds up Electrons

本論文係汪奕達(D08551001)在國立臺灣大學分子科學與技術國際研究生博士學位學程完成之博士學位論文，於民國 113 年 12 月 19 日承下列考試委員審查通過及口試及格，特此證明。

This is to certify that the PhD dissertation above is completed by I-Ta Wang (D08551001) during his studying in the International Graduate Program of Molecular Science and Technology, National Taiwan University, and that the oral defense of this thesis is passed on 2024/12/19 in accordance with decisions of the following committee members:

口試委員/Committee members:

陳俊維　呂欽山　薛丞中

(指導教授/Advisor)

[illegible]　羅志偉

系主任/所長(Department Chair/Program Director)：工學院分子科學與技術學程主任 康敦彥

誌謝

能夠完成這篇論文有太多人需要感謝，首先最感謝的就是我的兩位指導教授，陳俊維老師和朱明文老師，兩位老師在我博士班遇到重大變故時，給予了我很大的幫助，讓我有能力能夠將博士研究這條路走完。朱明文老師無論是實驗抑或是價值觀，都給予我很多的建議，讓我可以在一邊做研究的同時，一邊好好思考未來的人生，並且不斷修正自身的缺點，如果沒有朱明文老師的指導，可能我沒有信心能夠博士班畢業，真的非常感謝能夠在求學的最後一段路接受朱明文老師的指導，能夠被朱明文老師指導是非常非常幸運的一件事，真的很感謝老師。陳俊維老師則是給予我許多的幫助，從一開始的學程推薦，到後來不斷的鼓勵我，都讓我在博士班的生活中獲得安心的力量，在次感謝兩位老師在博士班研究的歲月中所帶給我滿滿的支持，謝謝兩位老師。

除了兩位老師外，實驗室的各位同仁也在這段時間內幫助我很多，從一開始跟著周大磊博士一起儀器的學習，到後來合作做出精彩的結果，非常感謝有學長的協助和合作；李明浩學長大大小小事情的幫助，無論是儀器的維護或是一邊閒談中的指導，都讓我獲益良多，平常跟學長的聊天總是可以在輕鬆的氛圍下學到很多人生不同的知識，如果沒有李明浩學長，我的博士班之路應該會走得非常艱辛；妤珈學姐的各種幫忙，讓我在研究艱難的過程中，可以不用花多餘的心思處理這些行政相關的事情，可以說是最令人安心的大姊頭；祉穎在加入實驗室之後的陪伴，不論是學術方面的討論，還是平常的開心聊天，總是在平常的相處中給予我很多的能量，可以說博士班的最後一里路能夠順利走完，日常生活中幾乎都是學妹的影子；士捷和 Bird 平常一起努力相處的情形也都歷歷在目，希望 Bird 在明年也能夠順利畢業，還有太多需要感謝的人和事情，讓我在博士研究的生涯中，雖然有時會想要放棄，但正因為有大家的協助，我才能夠在一次又一次的打擊中堅持下來，真的非常謝謝大家。

doi:10.6342/NTU202404787

摘要

隨著量子材料的出現，越來越多有趣的性質開始被大家研究並檢視。近年來，擁有在對稱保護下表現線性色散能帶的拓樸半金屬引起了大家的注意，這樣特殊的能帶結構，會造成特別的電荷屏蔽效應。我們利用電荷響應函數(Charge Response Function)去計算電磁易感率(Susceptibility)特別是電荷密度波(CDW)存在於材料中的情況，可幫助我們了解拓樸量子材料中有趣的電子結構。在本論文中，我們利用動量解析電子能量損失光譜(q-EELS)以及古典電漿子(plasmon)色散關係去偵測並且計算材料中載子的有效質量和費米速度，我們發現在碲化銅(CuTe)中，載子的有效質量和費米速度隨著電荷密度波序化的增強而分別變輕和增快，這與一般擁有電荷密度波的材料所表現的行為相反，也是本論文想要探討的主要目標。

在第一章中，我們對於量子材料和電荷屏蔽效應進行簡單的介紹，我們藉由對稱性的觀點切入量子材料，分別由反對稱中心和時間反演對稱中心以及破壞對於狄拉克(Dirac)和外爾(Weyl)費米子進行探討；我們也在電荷屏蔽的章節裡，簡單介紹電荷密度波、電漿子以及德汝德-勞倫茲模型(Drude-Lorentz Model)。在第二章，我們詳細的闡述掃瞄式穿透電子顯微鏡以及動量解析電子能量損失光譜的原理和應用。在第三章中，我們討論了關於碲化銅在動量解析電子能量損失光譜的結果，在不同動量空間下的光譜中，我們可以利用電漿子的色散關係得到相關載子的有效質量和費米速度，在碲化銅中，主要載子來源於線性色散能帶的輕電子以及與其垂直方向的重電洞。

在第四章中，我們探討在不同溫度下的動量解析電子能量損失光譜的實驗結果，因為隨著溫度低於電荷密度波相轉變溫度，電荷密度波序化會隨著溫度降低而增強，我們可以觀察電荷密度波序化增強與載子的關係。在室溫時，線性色散能帶的電子，同時也是與電荷密度波序化相關的載子，其有效質量約為 0.28 倍的電子靜止質量(m_0)，而其費米速度則約為光速的 0.005 倍。隨著溫度的降低和電荷密度波序化的增強，我們發現輕

doi:10.6342/NTU202404787

電子的有效質量變得更輕並且費米速度變得更快。在溫度到 100 K 時，載子的有效質量和費米速度相對於室溫時，變輕和增快約百分之 20。我們推測，造成這樣的原因，是因為線性色散的能帶在低溫下進行能帶的重整化(Band Renormalization)，使得能帶變的更陡峭，進而導致載子的有效質量變輕，以其費米速度增快。

電荷密度波隨著不同溫度下的序化現象在材料中有著重要的地位，碲化銅是一個適合針對電荷密度波以及弱相關系統進行研究的材料，而在適當的條件下，動量解析電子能量損失光譜更可以助於我們瞭解材料內的物理現象以及計算重要的物理參數，我們期待在更多擁有豐富物理性質的材料上，利用動量解析電子能量損失光譜獲得更加有趣的實驗結果。

關鍵字: 碲化銅(CuTe)，電荷密度波(Charge Density Wave)，電漿子色散關係，介電函數，德汝德-勞倫茲模型(Drude-Lorentz Model)，動量解析電子能量損失光譜

doi:10.6342/NTU202404787

Abstract

With the rapid advances discovery in various systems, quantum materials have aroused lots of attention in the field. Recently, topological semimetals featuring symmetry-protected crossing of linearly dispersing bands in the bulk electronic structure has gained growing attentions in the investigation of the electronic screening due to a finite density of states. Those unique material systems become interested with the concept of the matters susceptible to electronic ordering, where charge density waves (CDWs) are pervasive orders in the systems. The capability to probe the carrier density near the Fermi level inside the CDW systems in topological quantum matters allows a direct unveiling observation of the electronic structure.

This Ph.D. thesis has been dedicated to the momentum-dependent electron energy loss spectroscopy (q-EELS) on probing the effective mass and the Fermi velocity without further experiment setup. The reduced effective mass and the enhanced Fermi velocity in our CuTe system with CDW order growing exhibits an inverse result to the usual CDW systems.

A general introduction to the quantum materials and the charge response phenomena is presented in Chapter 1 and the experimental elucidation is addressed in Chapter 2. In Chapter 3, we show the q-EELS experimental result on the CuTe crystal, where we can obtain the effective mass and the Fermi velocity using the classical plasmon dispersion relation. We can simultaneously capture the effective mass and the Fermi velocity of the related, practically linearly dispersing electron and the counterpart of heavy-hole carrier.

In Chapter 4, we show the temperature dependent q-EELS experiment across the transition temperature 335 K ($T_{CDW,}$ CDW transition temperature) to help to observe the change followed the CDW order growth. The effective mass of practically linearly

doi:10.6342/NTU202404787

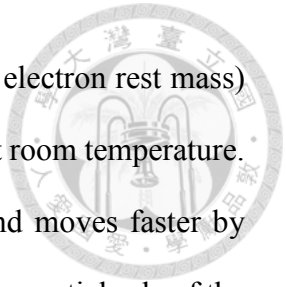

dispersing electron relating to CDW gap opening is 0.28 m_0 (m_0, the electron rest mass) and the Fermi velocity is approximate 0.005 c (c, the speed of light) at room temperature. Following the CDW order growth, the electrons becomes lighter and moves faster by ~20% toward to 100 K. Thorough inspection below T_{CDW} unveils the essential role of the increasing opening of the CDW gap. CuTe is a rich platform for the exploration of CDW and weak-coupled correlation physics with q-EELS as a useful tool for probing the associated fundamental properties.

Keywords: Copper Telluride (CuTe), Charge Density Wave, Plasmon Dispersion, Dielectric Function, Drude-Lorentz Model, Momentum-Dependent Electron Energy Loss Spectroscopy

doi:10.6342/NTU202404787

Content

doi:10.6342/NTU202404787

doi:10.6342/NTU202404787

doi:10.6342/NTU202404787

List of Figures

doi:10.6342/NTU202404787

doi:10.6342/NTU202404787

doi:10.6342/NTU202404787

doi:10.6342/NTU202404787

doi:10.6342/NTU202404787

doi:10.6342/NTU202404787

doi:10.6342/NTU202404787

List of Tables

doi:10.6342/NTU202404787

Chapter 1 Introduction

1.1 Quantum Materials

Quantum materials represent an exciting frontier in condensed matter physics, where the behaviors governed by quantum mechanical effects have quite difference properties than classical physics. Usually, quantum materials includes topological insulators [1-4], high-temperature superconductors [5-8], quantum magnets [9-12], and low-dimensional materials with symmetry breaking. For example, topological insulators are the systems protected by time-reversal symmetry, which makes the surface state residing in the bulk-insulating gap [4]. The iron-based superconductor are a potential material exhibiting high-temperature superconducting for hosting intrinsic time-reversal-invariant helical topological properties [6,7]. In addition, exploration of the novel relationship between magnetic order and topological semimetal has received lot of interests [10,12].

Each category of quantum materials demonstrates unique phenomena that challenge our understanding of many-body physics. Generally, the defining feature of quantum materials is that they exhibit collective behaviors that cannot be captured by classical models of matter. These behaviors are often a direct consequence of quantum effects such as wave-particle duality [13], quantum entanglement [13,14], and symmetry breaking, which are involved by complicated interaction between different kinds of particles, such as electrons, photons, and phonons.

Symmetry, in its universal understanding, refers to the invariance under certain transformational manipulations. Additional, inversion symmetry corresponds to the invariance of a system under spatial inversion, where the coordinates are transformed into their minus form, from (x, y, z) to (-x, -y, -z). On the other hand, time-reversal symmetry is the invariance of a system under the reversal of time, effectively changing the direction

doi:10.6342/NTU202404787

of motion and spin of particles inside the materials. When these two kinds of symmetries are present, they impose strict constraint on the electronic, magnetic, and optical properties of a material. Conversely, their breaking leads to emergent phenomena and exotic phases of materials [12]. At the subsequent content, we will introduce the inversion symmetry [15] and time-reversal symmetry and their breaking, which are central to the study of quantum materials. By focusing on these symmetries, we aim to illuminate the mechanisms resulting in the unique states of quantum materials.

doi:10.6342/NTU202404787

1.1.1 Inversion symmetry and its breaking

Inversion symmetry is a fundamental spatial symmetry in many crystal structures. Its presence or absence has profound consequences for the electronic and structural properties of a system [16,17]. For example, topological insulators have a great relationship to the inversion symmetry. Some topological insulators with inversion symmetry exhibit no edge or surface mode, but they exhibit protected modes in the entanglement spectrum[16.17]. If a material has both inversion symmetry and time-reversal symmetry, every electronic state at momentum k has a degenerate counterpart at k, which is the Kramers degeneracy[18,19]. Breaking inversion symmetry lifts these degeneracies in combination with spin-orbit coupling, leading to effects of spin splitting[19,20]. This spin splitting creates spin-polarized bands where the spin direction is locked to the momentum, an effect widely studied for spintronic application.

The breaking of inversion symmetry is often found in non-centrosymmetric crystals, which gives rise to a variety of novel phenomenon. For example, in materials like $BaTiO_3$, the absence of inversion symmetry allows a nonzero electric polarization to form[21-24]. This polarization can be reversed by an external electric field, making certain kind of materials useful in memory devices. Another effect resulting from the inversion symmetry breaking is the asymmetric spin-orbit coupling. The inversion symmetry breaking induced spin-orbit coupling may cause the topological phase transition[25-27]. The lack of inversion symmetry in certain superconductors and semiconductors introduces asymmetric spin-orbit interactions, which are crucial to the phenomena like the spin Hall effect and topological spin textures[27,28]. For example, with the inversion symmetry breaking, the system with spin-cluster phase is magnetically disordered but exhibiting a nonzero spin Hall conductivity[27]. In addition, the broken of inversion symmetry can ve employed to stabilize magnetic textures, such as the spin helices and skyrmions[27-30].

doi:10.6342/NTU202404787

The schematic illustration of inversion symmetry is shown in Fig. 1-1.

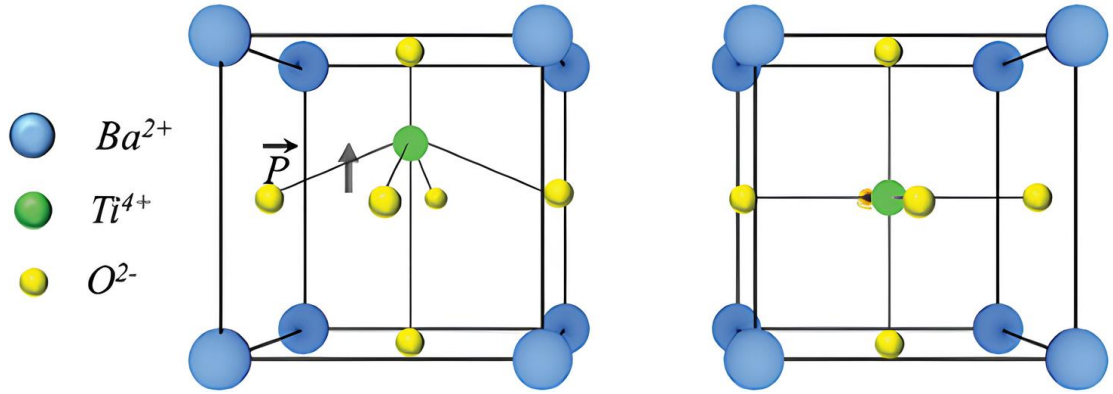

Figure 1-1 The schematic $BaTiO_3$ to illustrate inversion symmetry breaking. The left figure shows the inversion symmetry breaking resulting in ferroelectric property[24].

doi:10.6342/NTU202404787

1.1.2 Time-reversal symmetry and its breaking

Time-reversal symmetry relates to the properties of a system under the reversal of time, which means t to –t. This operation flips the momentum, k to –k, and spin direction of particles. Time-reversal symmetry also impose fundamental constraints on electronic, magnetic, and topological properties[16-18,31,32]. Usually, when time-reversal symmetry is preserved, the magnetism is absent in materials system. The electronic band structure is symmetric with respect to momentum space, at k point and –k point. Because of the time-reversal symmetry presence, the spin-degenerate states arise naturally, unless lifted by spin-orbit coupling broken inversion symmetry. In topological insulators, time-reversal symmetry protects surface states through spin-momentum locking, where the spin of an electron is tied to its momentum. As exhibiting spin-momentum locking, the topological protection prevents electron from coherent backscattering as long as the time-reversal symmetry is preserved[33,34]. This feature ensures that these states are robust against scattering from nonmagnetic impurities as well.

Talking to time-reversal symmetry breaking, often caused by magnetic order or external magnetic fields, will disrupt these constrains and cause to some exiting phenomenon. For example, in magnetic topological insulators, time-reversal symmetry breaking introduces a nonzero Chern number, resulting in quantized Hall conductance without an external magnetic field, which is so called quantum anomalous hall effect[35-40]. Generally, the quantum spin Hall state of matter is usually considered to be protected by time-reversal symmetry. However, with presence an exchange field, quantum spin Hall effect can be characterized by nonzero Chern number when time-reversal symmetry is broken. Additional, time-reversal symmetry breaking is essential for ferromagnetic and antiferromagnetic orders, where spins align or alternate in a specific direction[41,42]. Also, in certain unconventional superconductors, time-reversal symmetry breaking results in

doi:10.6342/NTU202404787

chiral pairing symmetries, where the superconducting order parameter acquires a complex phase structure[42]. This leads to edge current and other unique signatures. In Fig. 1-2, we use topological insulator to illustrate the time-reversal symmetry breaking. With magnetic doping, the band structure will open up a min-gap and lead to many exotic quantum phenomena.

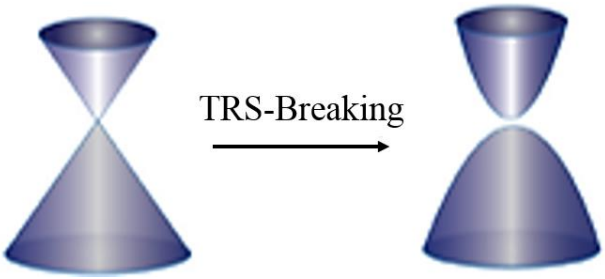

Figure 1-2 The schematic illustration of time-reversal symmetry breaking of topological insulators band structure[37].

doi:10.6342/NTU202404787

1.1.3 Dirac and Weyl fermions in quantum materials

Dirac and Weyl fermions are quasiparticles that arise as low-energy excitations in materials with specific symmetry properties and electronic structures[1]. Their existence is linked to the solutions of the Dirac equation (for Dirac fermions) and the Weyl equation (for Weyl fermions) in relativistic quantum mechanics, but in quantum materials, they manifest as emergent phenomena in the electronic band structure.

Dirac fermions occur at Dirac points in the band structure, where two doubly degenerate bands touch at discrete points in momentum space[43-45]. These degeneracies are protected by specific symmetries, including time-reversal symmetry, inversion symmetry, and also crystalline symmetries. At the Dirac points, because of the massless property, the dispersion follows the linearly relation as $\hbar v_F \mathrm{k}$, and causes the Dirac cone. Weyl fermions arise when the degeneracy of a Dirac point is split into two distinct points, called Weyl nodes, with opposite chirality[46-48]. This splitting occurs when either time-reversal symmetry and inversion symmetry is broken. Weyl fermions are associated with topological charges and lead to unique physical phenomena, such as Fermi arcs on the material's surface.

From the above content, we can understand that the transition from Dirac to Weyl fermions is directly tied to the breaking of specific symmetries. When breaking inversion symmetry, such as in TaAs or NbAs[49,50], lifts the degeneracy of the Dirac point, separating it into two Weyl nodes of opposite chirality. This splitting creates a pair of Weyl points in momentum space, which acts as monopole-like sources and sinks of Berry curvature. These materials exhibit phenomena such as the chiral anomaly, which is a unique transport signature where charge carriers flow preferentially along magnetic field lines. We can classify those materials as Weyl semimetals.

Other kinds of Weyl semimetals comes from the breaking of time-reversal symmetry.

doi:10.6342/NTU202404787

Breaking time-reversal symmetry through magnetic ordering also lifts the degeneracy of Dirac points, leading to Weyl nodes. The resulting material may exhibit magnetically tunable surface states and quantize anomalous Hall effects due to the time-reversal symmetry breaking[37,40].

The combination of inversion symmetry and time-reversal symmetry is important in shaping the behavior of quantum materials. When both inversion symmetry and time-reversal symmetry are present, materials can exhibit robust topological states, such as those in three-dimensional topological insulators, where the bulk bands are inverted at specific points in momentum space. For example, graphene 2D Dirac system follows the both symmetries preserved. When either symmetry is broken, the Dirac fermions may transform into Weyl fermions and lead to several exotic quantum phenomena.

doi:10.6342/NTU202404787

1.1.4 Summary

Inversion symmetry and time-reversal symmetry are fundamental to understanding the physics of quantum materials. Their presence imposes constraints that define material properties, while their breaking leads to novel phases and phenomena. The interplay between these symmetries is particularly significant in topological insulators, Weyl semimetals, and unconventional superconductors, where they shape the emergence of robust surface states, chiral transport, and exotic superconducting phases. By exploring the relation of Dirac fermions and Weyl fermions, we can have a deep understanding on the connection between the symmetry properties of materials and their electronic topology.

Quantum materials have attracted lots of attention in the modern physics. In order to gain a deeper understanding in the quantum materials field, figuring out the fundamental properties of the materials is quite important. If we can obtain the respective effective mass, carrier density, fermi velocity, and so on of the materials, we may take more steps to learn more in this field. In this thesis, we provide the method to help to obtain those essential properties, and try to explore the physics inside.

doi:10.6342/NTU202404787

1.2 Fundamental in Charge Screening

Charge screening is a cornerstone concept in the study of many-body-systems, describing how mobile charges in a medium rearrange themselves to neutralize the effects of external electric fields. This phenomenon has wide-ranging implications, from stabilizing the Coulomb interaction in dense plasmons to defining the collective behavior of electrons in metals and semiconductors. Screening is central to understanding fundamental properties of condensed matter systems, such as electrical conductivity plasmonic excitations, and the behavior of quasiparticles like excitons.

In a quantum mechanical framework, the behavior of electrons in response to external perturbations, such as an external electric field, is governed by their collective interaction with both the external and internal field. The Lindhard response function provides a rigorous theoretical picture for analyzing charge screening in such system, especially in the context of the electron gas model. This function extends classical approaches by accounting for quantum effects such as the Pauli Exclusion Principle, the discreteness of energy levels, and the wave-like nature of electrons.

doi:10.6342/NTU202404787

1.2.1 Charge screening and the Lindhard response function

Charge screening occurs when mobile charges redistribute in order to reduce the net electric field when the external perturbation exists. In classical sense, this redistribution would minimize the potential energy of the system, effectively screening the long-range Coulomb interaction. Screening is especially significant in systems with high charge density, such as metals and plasmons, where collective effects dominate.

Charge screening can be understood through the concept of the screened potential:

$$\varphi_{screened}(r) = \varphi_0(r)e^{-\kappa r} \tag{1.1}$$

where $\varphi_0(r)$ is the unscreened Coulomb potential, and κ is the screening wave vector. The exponential factor reflects the suppression of the potential over distances larger than the screening length, which is κ^{-1}.

The Lindhard response function provides a quantum-mechanical description of how electron gas responds to an external perturbation[51,52]. Developed in the framework of linear response theory, it offers a microscopic derivation of the dielectric function in terms of the electronic structure of the system.

Consider an external perturbation $\varphi_{ext}(r,t)$ applied to electron gas. The total potential φ_{tot} experienced by electrons is a combination of the external potential and the induced potential φ_{ind}, which arises from the redistribution of charges:

$$\varphi_{tot}(r,t) = \varphi_{ext}(r,t) + \varphi_{ind}(r,t) \tag{1.2}$$

The induced potential is related to the induced charge density ρ_{ind}, which in turn depends on the external potential. This relationship is mediated by the susceptibility $\chi(q,\omega)$, which describes how charge density responds to an external perturbation in frequency and wave vector space:

$$\rho_{ind}(q,\omega) = -\chi(q,\omega)\varphi_{ext}(q,\omega) \tag{1.3}$$

doi:10.6342/NTU202404787

The dielectric function $\varepsilon(q,\omega)$ connects the external and total potentials:

$$\varphi_{tot}(q,\omega) = \frac{\varphi_{ext}(q,\omega)}{\varepsilon(q,\omega)} \tag{1.4}$$

where $\varepsilon(q,\omega)$ is related to susceptibility by:

$$\varepsilon(q,\omega) = 1 + \chi(q,\omega) \tag{1.5}$$

For a non-interacting electron gas, the susceptibility $\chi(q,\omega)$ can be derived using first-order perturbation theory. The Lindhard respond function is given by[51]:

$$\varepsilon(q,\omega) = 1 + \lim_{\tau\to\infty} \frac{4\pi e^2}{q^2\Omega} \sum_k \frac{f(E_k) - f(E_{k+q})}{E_{k+q} - E_k - \hbar\omega + i\hbar/\tau} \tag{1.6}$$

Following the equation (1.6), the Lindhard susceptibility can be written as:

$$\chi(q,\omega) = \frac{4\pi e^2}{q^2\Omega} \sum_k \frac{f(E_k) - f(E_{k+q})}{E_{k+q} - E_k - \hbar\omega} \tag{1.7}$$

where the $f(E_k)$ is the Fermi-Dirac distribution in thermodynamic equilibrium, E_k is the energy dispersion, $\frac{4\pi e^2}{q^2}$ is the Fourier transform of the Coulomb potential, and Ω is the system volume. In the static limit, which ω = 0, the Lindhard function can be simplifies to[51]:

$$\chi(q,\omega) = \frac{4\pi e^2}{q^2\Omega} \sum_k \frac{f(E_k) - f(E_{k+q})}{E_{k+q} - E_k} \tag{1.8}$$

doi:10.6342/NTU202404787

1.2.2 Static limit and Charge Density Wave (CDW)

Static screening of the Lindhard function, which refers to the condition of $\omega = 0$, means that the redistribution of charges in equilibrium under the influence of a stationary test charge. In this regime, the screening length and dielectric response depend solely on the density of states at the Fermi level and the interaction length.

Charge density wave (CDW) is at the static limit of the Lindhard response function with a fixed $q = 2k_F$, where the k_F is the Fermi wave vector[53-56]. Fig. 1-3 shows the schematic illustration of CDW under static limit.

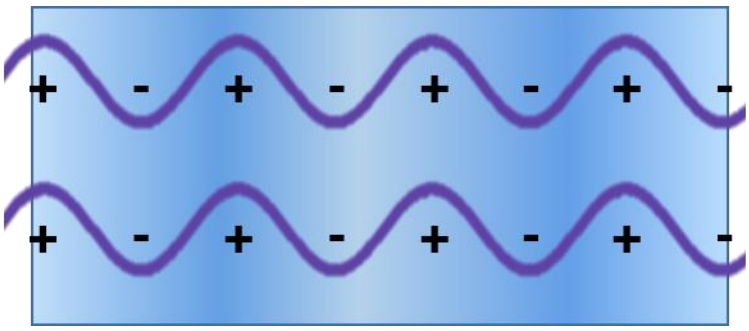

Figure 1-3 The schematic illustration of CDW under static limit[53].

CDWs were expected to exist in low dimensional materials by Peierls and Fröhlich in 1950s[57]. A CDW state can be characterized by a periodic modulation of the electronic charge density within a material. This modulation is typically accompanied by a corresponding distortion of the lattice structure, resulting in a complex interplay between electronic and lattice degrees of freedom. If the wavelength of the CDW is the simple fraction of the lattice parameter, then the CDW is called commensurate. Otherwise, the CDW is called incommensurate[54]. CDWs can be understood as a collective state of

doi:10.6342/NTU202404787

electrons that arises due to the electron-phonon interactions, leading to a lower energy configuration. The periodicity of the charge density wave is often commensurate or incommensurate with the underlying lattice, and this relationship plays a crucial role in determining the physical properties of the material. CDWs are typically observed in low-dimensional systems, such as quasi-one-dimensional conductors and layered materials, where the reduced dimensionality enhances the electron-phonon coupling, making the formation of CDWs more favorable.

CDWs are of significant interest in condensed matter physics due to their rich and complex behavior, which provides insights into fundamental interactions between electrons and the lattice. The study of CDWs has revealed a variety of intriguing phenomena, including the competition between CDWs and superconductivity, and the role of disorder and impurities in pinning CDWs. These interesting phenomena have implications for understanding the electronic properties of materials and for the development of novel electronic devices. Moreover, CDWs serve as a prototype for studying other collective electronic states, such as spin density waves and superconductivity, making them a valuable model system for exploring the interplay between electronic correlations and lattice dynamics. The continued investigation of CDWs promises to advance our understanding of complex materials and contribute to the development of new technologies based on the unique properties of these systems.

One of the primary mechanisms driving the formation of CDWs is electron-phonon interactions. In the CDW system, the coupling between electrons and lattice vibration, or phonons, plays a crucial role. When electrons in a materials interact with phonons, they can induce a distortion in the lattice structure, leading to a periodic modulation of the charge density. This interaction is particularly significant in low-dimensional systems, where the reduced dimensionality enhances the electron-phonon coupling, making the

doi:10.6342/NTU202404787

system more susceptible to instabilities that result in CDWs. The strength of this interaction can be quantified using parameters such as the electron-phonon coupling constant, which provides insights into the properties of a material of form CDWs. Understanding these interactions is essential for elucidating the conditions under which CDWs emerge and for predicting their properties in various materials.

As previous said, Peierls realized that the electron-phonon interaction in 1D metallic chain could cause the opening gap[57]. The instability of the 1D atoms towards the presence of the electron-phonon interaction is known as Peierls instability. Peierls instability arises when a one-dimensional metallic, or pseudo-1D, systems undergoes a spontaneous distortion of its lattice at low temperatures, leading to the opening of a gap at the Fermi surface. The distortion results in a lower energy state, making it energetically favorable for the system to transition into a CDW state. The Peierls transition is driven by the fact that the electronic energy gain from the opening of the gap outweighs the elastic energy cost of the lattice distortion. The usual schematic illustration is shown in Fig. 1-4.

In Fig. 1-4, when one of a 1D metallic chain with lattice constant a and a half filled band goes to low temperature, atoms will undergo a lattice distortion and make a new periodicity with 2a. Meanwhile, the charge density and the atom displacement will form into a sinusoidal wave and open a gap at the Fermi surface in order to lower the energy of the occupied state. The electron-band energy gain is enough to compensate the energy cost required by the CDW transition.

doi:10.6342/NTU202404787

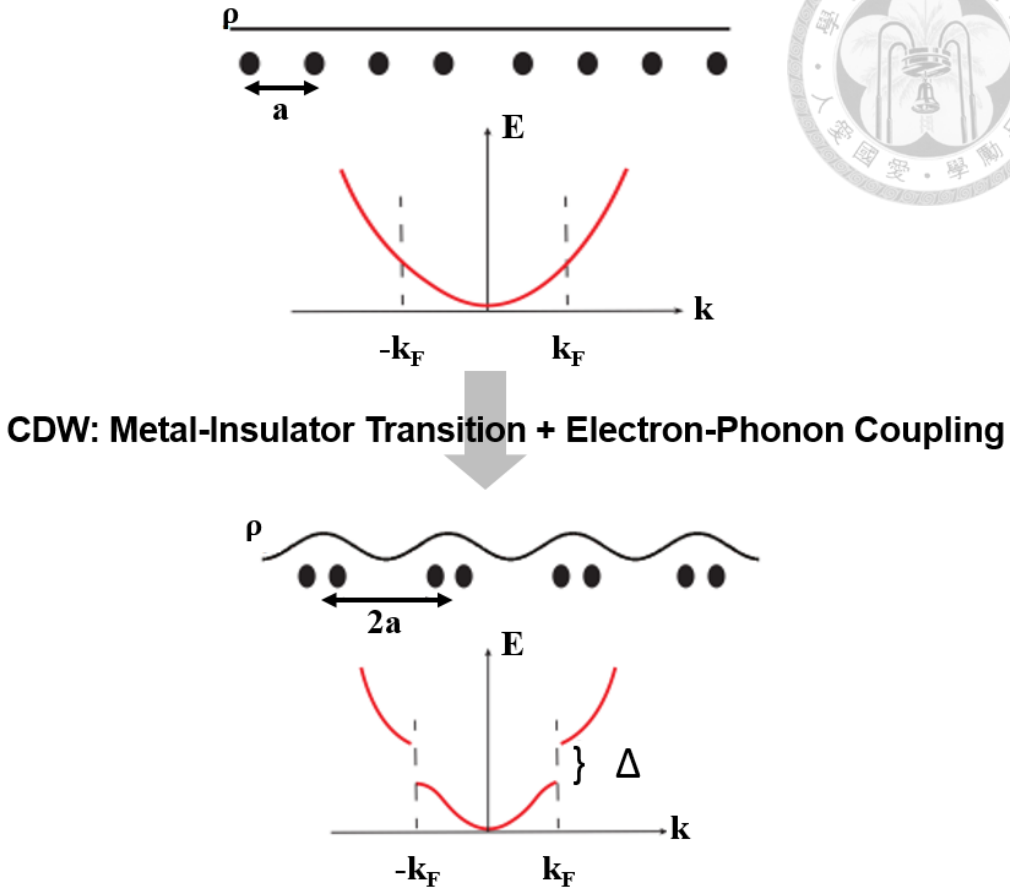

Figure 1-4 The schematic illustration of the Peierls instability and CDW forms by electron-phonon coupling[53].

The normal coordination that describe the ionic oscillation are $U_q = \left(\frac{\hbar}{2m\omega_q}\right)^{0.5}$ with m the ionic mass and U_q the displacement of the ionic atom. The ionic potential resulting from U_q and induce an electron charge density given by[53,54]:

$$\rho_q = \chi(q,T) \times g \left(\frac{2m\omega_q}{\hbar}\right)^{0.5} U_q \tag{1.9}$$

where $\chi(q,T)$ is the susceptibility, g is the electron-phonon coupling constant. With equation (1.9), we can introduce a renormalized phonon frequency at $q = 2k_F$ as[53,54],

$$\omega_{renorm} = \omega_{2k_F} - \frac{2g^2 n \omega_{2k_F}}{\hbar} \ln\left(\frac{1.14\epsilon_F}{k_B T}\right) \tag{1.10}$$

doi:10.6342/NTU202404787

In the presence of electron-phonon coupling, the frequency going to zero at a finite temperature can be define by[53]

$$k_B T_{CDW} = 1.14\epsilon_F e^{1/\lambda} \quad (1.11)$$

with $\lambda = \frac{g^2 n}{\hbar\omega_{2k_F}}$ and k_B the Boltzmann constant. The phonon dispersion is shown in Fig. 1-5. The strong renormalization of the phonon mode in 1D metal is also known as Kohn anomaly and it is the signature of a phase transition due the divergence of the electronic susceptibility[60]. When the temperature is lower than T_{CDW}, the phonon dispersion will drop to zero and $q = 2k_F$.

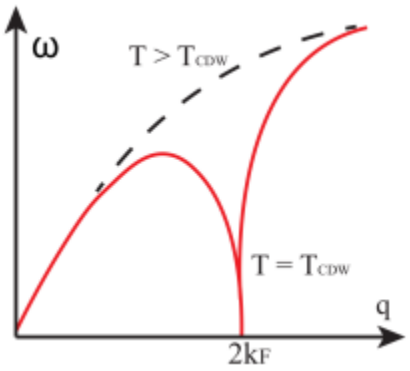

Figure 1-5 Phonon dispersion for 1D metal above and below T_{CDW}[53].

In addition to the Kohn anomaly, Fermi surface nesting is another critical mechanism that contributes to the formation of CDWs. Recall the equation (1.8), the response function diverges for $q = 2k_F$ in 1D system, which means that the system is unstable under an external perturbation, shown in Fig 1-6a. This perturbation could be presented by electron-phonon interaction or electron-electron interaction. In a 1D metal, the divergence of the electronic susceptibility depends on the topology of the Fermi surface, in particular to the so-called Fermi surface nesting[61]. The nesting describes the situation when identical portions of the Fermi surface can moved on top of each other by elastic scattering.

doi:10.6342/NTU202404787

The vector that connects the two portions is called nesting vector. In the case of 1D electron gas, the Fermi surface consists of two points connected by the nesting factor of $q = 2k_F$. The schematic illustration of Fermi surface nesting is shown in Fig. 1-6b[53,61]. When the Fermi surface nesting takes place, the electron on one band can be elastic scattered to another band on the Fermi surface and creates an electron-hole pair which strengthen the lattice distortion and amplifying the electron-phonon interactions. When the nesting vector matches the wave vector of the lattice distortion, it leads to a significant enhancement of the electronic susceptibility, promoting the formation of a CDW.

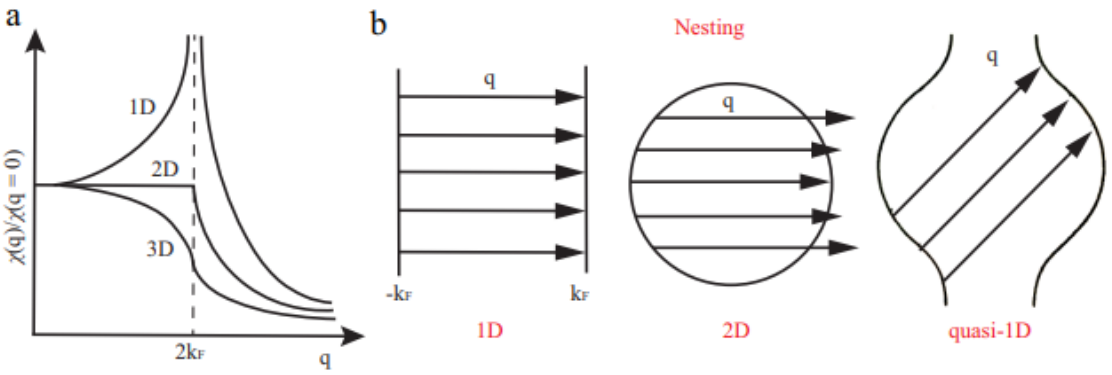

Figure 1-6 The response function and the schematic illustration of Fermi surface nesting. (a) The Lindhard response function for 1D, 2D, and 3D free electron gas at 0 K. (b) Fermi surface topology and nesting for 1D, 2D, and quasi-1D free electron gas. The arrow connect the empty and occupied states separated by $2k_F$[53].

CDWs existence in material system will affect electrical properties and conductivities. In condensed matter systems, the formation of a CDW can lead to a reduction in electrical conductivity due to the opening of a gap at the Fermi surface, which is called metal to insulator transition[62]. This gap effectively reduces the number of charge carriers

doi:10.6342/NTU202404787

available for conduction, thereby increasing the resistivity of material. In addition, the relationship between charge density wave and superconductivity is also significant in condensed matter physics. Both phenomena involve the collective behavior of the electrons and con coexist or compete within the same material. In some systems, the formation of a CDW can suppress superconductivity by opening a gap at the Fermi surface, which reduces the density of state available for Cooper pair formation[63-65].

In a brief summary, CDWs formation at the material system is a topic of important interest in condensed matter physics. With the aid of Fermi surface nesting, Peierls instability may cause the lattice distortion, which forms new periodicity of q_{CDW} in momentum space with gap opening at the Fermi surface. The corresponding phonon dispersion will show Kohn anomaly effect with electron-phonon coupling effect. It will be interesting to study physics of the quantum materials with CDWs presence.

doi:10.6342/NTU202404787

1.2.3 Long-wavelength limit and Plasmon

Recall the Lindhard response function in equation (1.6), in the contrast of static limit which $\omega \to 0$, the long-wavelength limit ($q \to 0$) would cause the plasmon in the material system[51]. The dielectric function can be simplified as

$$\varepsilon(\omega) = 1 - \frac{\omega_p^2}{\omega^2 + i\omega\gamma} \tag{1.12}$$

where ω_p is the plasmon frequency, γ is the damping constant.

Plasmons are collective oscillations of free electron density in a conductive material, often induced by electromagnetic radiation at optical frequencies[66-68]. These oscillations arise due to the coupling between the electromagnetic field and the free electrons in the material. The study of plasmons is central to the field of nanoplasmonics, which explores light-matter interactions at the nanoscale and has significant implications for areas such as nanophotonics, surface-enhanced spectroscopy, and optical sensing

At its core, a plasmon is a quantized excitation of the plasma state in a material[51,67]. In metals and certain semiconductors, the conduction electrons form a free electron gas, which can oscillate collectively when displaced from their equilibrium position. The displacement generates a restoring force due to the positively charged ionic lattice, resulting in coherent electron density waves. The frequency of these oscillation, known as the plasmon frequency, is a critical parameter for characterizing plasmon behavior and is given by[69],

$$\omega_p = \sqrt{\frac{4\pi n e^2}{m^* \varepsilon_\infty}} \tag{1.13}$$

where n is the carrier density, e is the elementary charge, m* is the effective mass, and the ε_∞ is the dielectric constant of free space. The plasmon frequency typically in the ultraviolet range for most metals, around 15 to 30 eV, indicating that materials can support plasmon oscillation under optical or near optical excitation. Fig. 1-7 shows a schematic

doi:10.6342/NTU202404787

illustration of plasmon in free electron gas model.

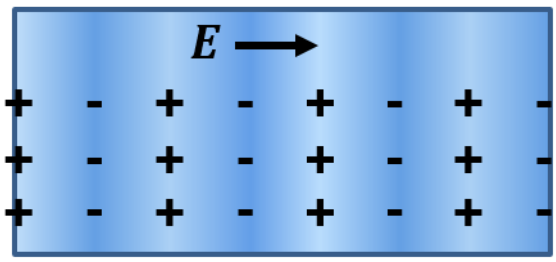

Figure 1-7 The schematic illustration of plasmon presence in material. With the external perturbation, plasmon will follow the response function to reduce the net electric field inside the material[70].

The behavior of plasmons can be rigorously described using Maxwell equations coupled with material-specific dielectric functions. For a metal characterized by the Drude model, the dielectric function is expressed as[71]:

$$\varepsilon(\omega) = \varepsilon_{\infty} - \frac{\omega_p^2}{\omega^2 + i\gamma\omega} \tag{1.14}$$

γ is the damping constant, representing energy losses due to electron scattering.

Plasmons occur at when $\varepsilon(\omega) = 0$. This happens at the plasmon frequency ω_p, where the collective oscillations of free electron dominate. Bulk plasmons are longitudinal modes and do not directly couple to transverse electromagnetic waves, making them in accessible via optical excitation. However, it is easily observable from electron energy loss spectroscopy (EELS), making EELS as a useful tool to probe plasmons in materials system.

Talking to the dielectric function dependent with momentum and frequency, it reflects the material's ability to polarize in response to an external field, which determines the nature of plasmon excitation. Dielectric function can be written as[72]:

doi:10.6342/NTU202404787

$$\varepsilon(\omega) = \varepsilon_1 + i\varepsilon_2 \tag{1.15}$$

where ε_1 is the real part of dielectric function, indicating whether the material supports or resists plasmon oscillations. Negative values correspond to a phase lag, which is essential for sustaining surface plasmon waves. ε_2 is the imaginary part of dielectric function, representing energy dissipation due to electron scattering or interband transitions, which cause the absorption of material. A high ε_2 results in significant damping, reducing the quality factor of the plasmon resonance.

We can go deeper at the reason why plasmon takes place at $\varepsilon(\omega) = 0$, or $\varepsilon_1 = 0$. It is because the condition signifies a resonance condition in which the collective oscillations of free electrons in a material are sustained without net restoring forces from the dielectric background. At this situation, the induced polarization perfectly cancels the external electric field with the material. The induced polarization is given by $\mathrm{P} = (\varepsilon - 1)E$, where E is the electric field. When $\varepsilon = 0$, the polarization P vanishes, meaning the restoring force from polarization no longer opposes the motion of free electrons. Without a net restoring force, the collective oscillations of the free electrons in response to the external field become self-sustaining. These oscillations propagate as density waves of the electron cloud.

With measuring the energy or the dispersion of plasmon, we can obtain more information correspond to the certain carrier at the momentum space. This can give us some important hints in the complicated material system.

doi:10.6342/NTU202404787

1.2.4 Drude model and Drude-Lorentz model

Drude and Drude-Lorentz (DL) model can give us some basic understanding from dielectric function and help us realize the properties of carrier inside the materials. The study of the interaction between electromagnetic waves and materials lies at the heart of condensed matter physics and materials science. Dielectric function can characterize how the material polarizes in response to the field. This polarization is influenced by the free and bound charges in the material and in central to understanding phenomena like electrical conductivity, optical absorption, and the propagation of electromagnetic waves in different media[51].

The Drude model and its extension, the Drude-Lorentz model (DL), form the foundational theories describing the dielectric properties of materials. These models provide a semiclassical framework to analyze the motion of charge carriers under external electric fields. The Drude model focuses on free electrons, treating them as classical particles subject to collisions, while the Drude-Lorentz model incorporates bound electron oscillations, introducing resonance phenomena that account for material-specific optical properties

The Drude model, introduced by Paul Drude in 1900, represents one of the earliest attempts to describe the electrical and thermal properties of metals[73,74]. It was inspired by the kinetic theory of gases and applies similar principles to the "electron gas" in metals. The model assumes that conduction electrons move freely within a lattice of positively charged ions and interact only through occasional collisions, akin to the behavior of gas molecules

The Drude model is based on the following key assumptions. The first assumption is that electrons in a metal are treated as a classical gas of non-interacting particles. These electrons are subject to a mean free path or mean collision time τ, during which they move

doi:10.6342/NTU202404787

freely between collisions with the lattice. The effect of collisions is modeled as a damping force proportional to the electron velocity. The interaction between electrons and the periodic potential of the lattice is neglected.

However, while the Drude model successfully explains the behaviors of free electrons in metals, it fails to account for the response of bound electrons. In real materials, the electronic response includes contributions from localized charges bound to atoms or ions, which can oscillate under the influence of an external field. These oscillations lead to resonance phenomena and frequency-dependent dielectric properties.

Here, we are going to use Maxwell's equations with material polarization to obtain the Lorentz model of dielectrics. Materials polarization is incorporated into constitutive relations given by[75,76]:

$$\vec{D} = \varepsilon_0 \vec{E} + \vec{P} \tag{1.16}$$

where the $\varepsilon_0 \vec{E}$ represents the response to free space, and the $\vec{P}$ represents the response of material. Constitutive relation in terms of relative permittivity and susceptibility is given by:

$$\vec{D} = \varepsilon_0 \tilde{\varepsilon}_r \vec{E} = \varepsilon_0 \vec{E} + \varepsilon_0 \chi \vec{E} \tag{1.17}$$

Comparing the equation 1.16 and 1.17, we can get:

$$\vec{P} = \varepsilon_0 \chi \vec{E} \tag{1.18}$$

and

$$\tilde{\varepsilon}_r = 1 + \chi \tag{1.19}$$

where $\tilde{\varepsilon}_r$ is the dielectric function of the material and χ is the susceptibility of the material.

The Lorentz model of electron motion can be applied by the Newton's second law by :

$$\mathrm{m}\frac{\partial^2 \vec{\mathrm{r}}}{\partial t^2} + \mathrm{m}\Gamma\frac{\partial \vec{r}}{\partial t} + m\omega_0^2 \vec{r} = -q\vec{E} \tag{1.20}$$

where the first term describes the acceleration force and the m is the mass of an electron.

doi:10.6342/NTU202404787

The second term describes the frictional force, which Γ denotes the damping rate. The third term describes the restoring force and the ω_0 represents the resonance frequency of the oscillator. The term on the other side of equation is the electric force.

We can bring time-harmonic fields into equation (1.20),

$$\vec{E}(\mathrm{t}) = \overrightarrow{E_0} e^{-i\omega t} \tag{1.21}$$

$$\vec{r}(\mathrm{t}) = \overrightarrow{r_0} e^{-i\omega t} \tag{1.22}$$

Then we can obtain:

$$\vec{r}(\omega) = -\frac{q}{m_e}\frac{1}{\omega_0^2 - \omega^2 - i\omega\Gamma}\vec{E}(\omega) \tag{1.23}$$

The displacement function $\vec{r}(\omega)$ will induce a dipole moment $\vec{\mu}(\omega)$, given by,

$$\vec{\mu}(\omega) = -\mathrm{q}\vec{r}(\omega) \tag{1.24}$$

where q is the charge and the $\vec{r}(\omega)$ represents the distance from center, then we can obtain dipole moment $\vec{\mu}(\omega)$,

$$\vec{\mu}(\omega) = \frac{q^2}{m_e}\frac{1}{\omega_0^2 - \omega^2 - i\omega\Gamma}\vec{E}(\omega) \tag{1.25}$$

After obtaining dipole moment function, we can get the Lorentz polarizability $\alpha(\omega)$ by,

$$\vec{\mu}(\omega) = \alpha(\omega)\vec{E}(\omega) \tag{1.26}$$

Then, Lorentz polarizability $\alpha(\omega)$ will be,

$$\alpha(\omega) = \frac{q^2}{m_e}\frac{1}{\omega_0^2 - \omega^2 - i\omega\Gamma} \tag{1.27}$$

We can define the polarization per unit volume by average dipole moment over all atoms in a material.

$$\vec{P}(\omega) = \mathrm{N}\langle\vec{\mu}(\omega)\rangle \tag{1.28}$$

Where N is the number of atoms per unit volume and $\langle\vec{\mu}(\omega)\rangle$ represents the statistical average of dipole moment.

doi:10.6342/NTU202404787

Here, we recall the equation 1.18, 1.26, and 1.27. The combination of these three equations can lead to an expression for the susceptibility by,

$$\chi(\omega) = \frac{N\alpha(\omega)}{\varepsilon_0} = \left(\frac{Nq^2}{\varepsilon_0 m_e}\right)\frac{1}{\omega_0^2 - \omega^2 - i\omega\Gamma} \tag{1.29}$$

then combine the equation 1.13 to 1.29, we can obtain the susceptibility:

$$\chi(\omega) = \frac{\omega_p^2}{\omega_0^2 - \omega^2 - i\omega\Gamma} \tag{1.30}$$

where ω_p is the plasmon frequency.

Then, we recall the equation 1.17, we can obtain the dielectric function by,

$$\tilde{\varepsilon}_r(\omega) = 1 + \frac{\omega_p^2}{\omega_0^2 - \omega^2 - i\omega\Gamma} \tag{1.31}$$

We can recall the equation 1.15 to split the dielectric function in to real and imaginary parts. We can obtain the real part ε_1 and the imaginary part ε_2 as,

$$\varepsilon_1(\omega) = 1 + {\omega_p}^2 \cdot \frac{{\omega_0}^2 - \omega^2}{({\omega_0}^2 - \omega^2)^2 + \omega^2\Gamma^2} \tag{1.32}$$

$$\varepsilon_2(\omega) = {\omega_p}^2 \cdot \frac{\omega\Gamma}{({\omega_0}^2 - \omega^2)^2 + \omega^2\Gamma^2} \tag{1.33}$$

Equation 1.32 and 1.33 will be the final form of dielectric function of Drude-Lorentz model.

In the other hand, we can also derive the dielectric function from Drude model. In metals, most electrons are free because they are not bound to a nucleus. For this simple simulation, the restoring force is negligible and there is no natural frequency.

doi:10.6342/NTU202404787

We can derive the Drude model for metals by assuming $\omega_0 = 0$, then we can obtain the dielectric function as[74],

$$\tilde{\varepsilon}_r(\omega) = 1 - \frac{\omega_p^2}{\omega^2 + i\omega\Gamma} \tag{1.34}$$

where the N in plasmon frequency is interpreted as electron density.

Hence, the real and imaginary part of dielectric function for Drude model will be,

$$\varepsilon_1(\omega) = 1 - \frac{{\omega_p}^2}{\omega^2 + \Gamma^2} \tag{1.35}$$

$$\varepsilon_2(\omega) = \frac{1}{\omega} \cdot \frac{{\omega_p}^2\Gamma}{\omega^2 + \Gamma^2} \tag{1.36}$$

Fig. 1-8 shows the theoretical illustration of the real and imaginary part of dielectric function from Drude and Drude-Lorentz model.

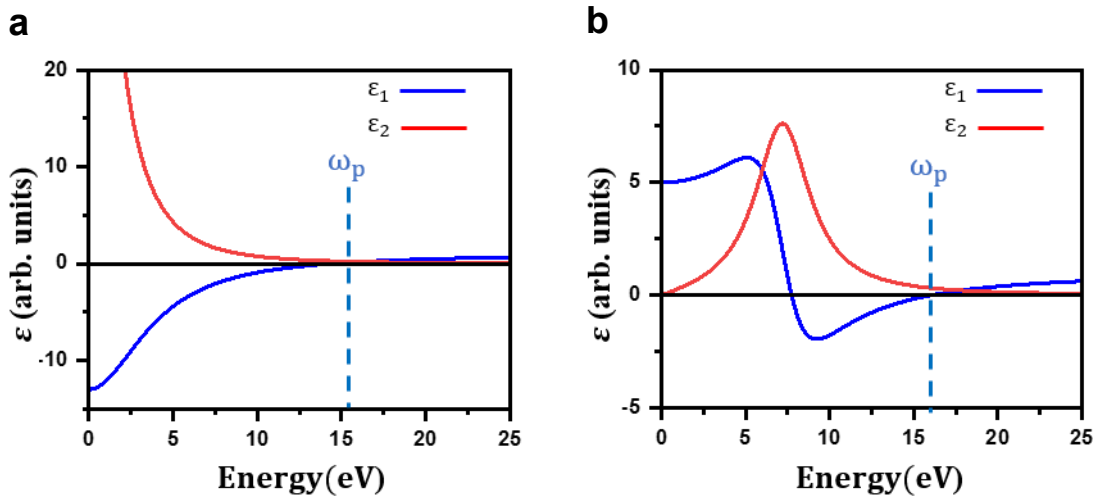

Figure 1-8 The theoretical illustration of (a) Drude and (b) Drude-Lorentz model. The plasmon frequency takes place at the condition of $\varepsilon_1(\omega) = 0$. The peak in Drude-Lorentz model represents a absorption which could result from the interband transition, intraband transition, or single-particle transition. In the real material system, the absorption peak in Drude-Lorentz model may screen the plasmon oscillation into higher or lower energy.

doi:10.6342/NTU202404787

Here, we combine Drude-Lorentz model to unify the free and bound electron responses[77]:

$$\tilde{\varepsilon}_r(\omega) = 1 - \frac{\omega_p^2}{\omega^2 + i\omega\Gamma} + \sum_j \frac{\omega_{p,j}^2}{\omega_{0,j}^2 - \omega^2 - i\omega\Gamma_j} \tag{1.37}$$

Hence, the first term describes free electrons behavior (Drude term), while the summation accounts for multiple Lorentz oscillators corresponding to different bound electron resonances, which can also be understood as the interband or intraband transition in the material systems.

The DL models provide essential frameworks for understanding the dielectric function of materials. While the Drude model effectively captures the response of free electrons, the DL model incorporates the critical contributions of bound electron oscillations. Together, these models offer insights into the optical, electronic, and plasmon properties of metals, semiconductors, and insulators.

doi:10.6342/NTU202404787

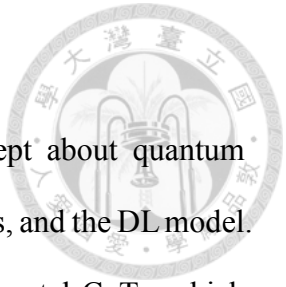

1.3 Summary

In the Chapter 1, we briefly introduce some important concept about quantum materials and the charge response behaviors including CDW, plasmons, and the DL model. With these concepts, they give us the clues to explore the target semimetal-CuTe, which owns the CDW under 335 K with practically-linearly dispersion band. By using those concepts mentioned in Chapter 1, we can obtain important factors, such as effective mass, carrier density correspond to CDW, Fermi velocity, and so on. With the aid to the momentum resolved EELS measurement, which will introduce in Chapter 2, we probe the respective plasmons dispersion and realize the surprising phenomena in CuTe.

doi:10.6342/NTU202404787

Chapter 2 Experimental method

2.1 Scanning Transmission Electron Microscopy (STEM)

2.1.1 Introduction to STEM

Scanning Transmission Electron Microscopy (STEM) is a powerful and versatile analytical technique that merges the capabilities of Transmission Electron Microscopy (TEM) with those of Scanning Electron Microscopy (SEM). By focusing a finely converged electron probe onto a specimen and scanning it point-by-point, STEM generates detailed high-resolution images, compositional analysis, and spectroscopic data from nanometer to sub-angstrom scales[78].

The principles of STEM are rooted in the interaction of high-energy electrons with matter and subsequent detection of scattered and transmitted electrons. In STEM, with the aid of aberration correction, STEM instrument can employ advanced optics to correct spherical aberrations, enabling probe size become smaller and enhance the atomic-resolution.

Generally, high-angle annular dark field (HAADF) imaging are the specialized STEM mode that collects electrons scattered incoherently to high angles using an annular detector. This technique offers direct atomic-resolution imaging with intensity proportional to the atomic number. When the focused electron beam interacts with the specimen, electrons are scattered elastically and incoherently to a wide range of angles. HAADF imaging isolates those scattered to high angles, and the intensity would proportional to atomic number. The Z-contrast mechanism results in images where heavier elements appear brighter than lighter ones, allowing clear differentiation atoms based on the atomic weight,

In Fig. 2-1, we show the schematic diagram of the mechanism of STEM[79]. The

doi:10.6342/NTU202404787

orange circular plate works as HAADF detector, which can help to obtain the incoherent thermal scattering electrons at high angles. In addition to the high-angle scattered electrons, STEM can simultaneously record the EELS spectrum, where the EELS entrance aperture is shown as the blue circular plate. When we are acquiring EELS spectrum, we need to make sure that EELS collection angle β needs to be larger than the convergence semi-angle α in order to prevent the diffraction information interference in EELS spectrum.

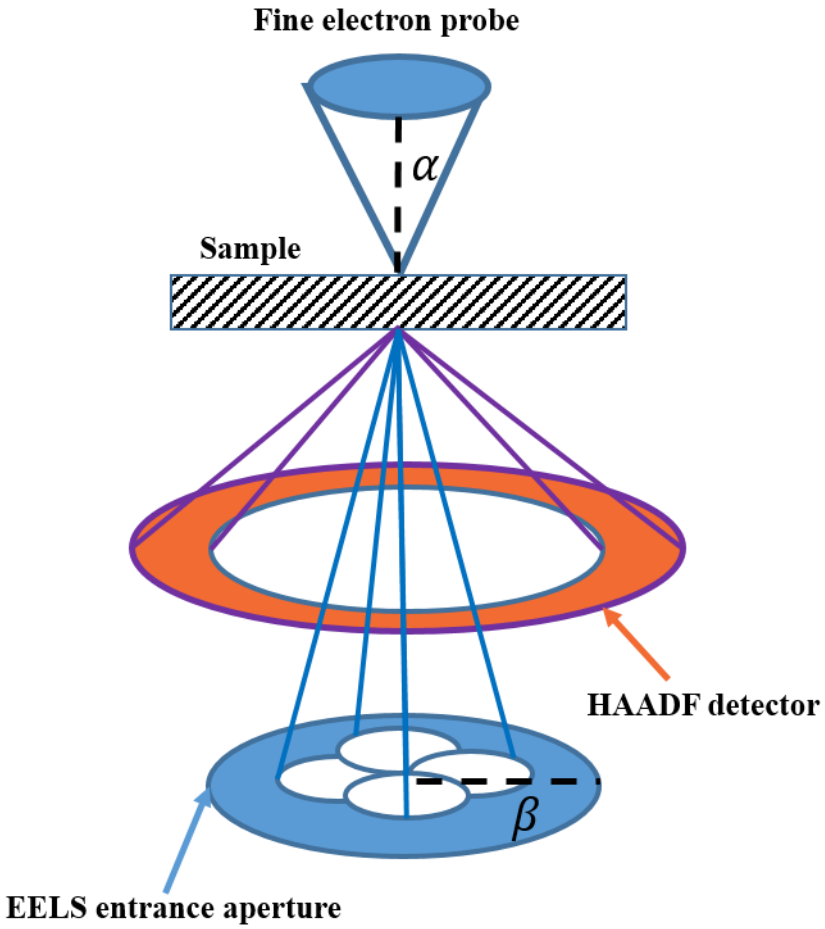

Figure 2-1 The schematic illustration of the mechanism of STEM with HAADF detector and the EELS spectrum acquisition[79].

doi:10.6342/NTU202404787

If we collect the spectrum at each pixel of scanned image, we can obtain a three-dimensional data cube which consists of both spectral and spatial information of the material, as shown in Fig. 2-2[80,81]. The x and y dimensions represents the spatial coordination when we acquire the STEM HAADF images. The third dimension ΔE is the EELS spectra at each pixel. We can select the energy window we want and the chemical mapping can be obtained.

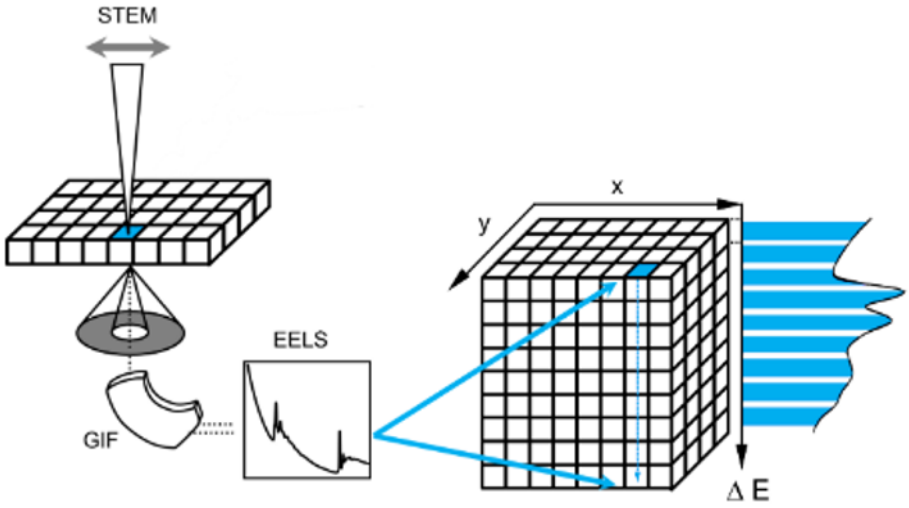

Figure 2-2 The schematic illustration of STEM spectrum imaging[70].

Spectrum imaging technique becomes a powerful tool of analyzing materials due to the improving computational software and the better digital recorded images. However, the spatial resolution of STEM spectrum imaging technique is limited to the minimum probe size and the acquiring efficiency of conventional spectrometers, which cause the long acquisition time[82]. The longer the acquisition time, the more mechanical instability presence in images. The spatial resolution can be improved by the spherical aberration correction (Cs-corrector), which will be introduced by next section.

doi:10.6342/NTU202404787

2.1.2 Spherical aberration correction (Cs-corrector)

Spherical aberration correction exists in every types of round lenses, including optical and electromagnetic lens in the microscope. The resolution of the electron microscope is affected by the spherical aberration coefficient and the point resolution (d_p) in TEM can be given by,

$$d_p = 0.65Cs^{1/4}\lambda^{3/4} \quad (2.1)$$

Where Cs is the spherical aberration of the objective lens, and λ is the wavelength of incident electron beam[83].

Therefore, in order to enhance the resolution in microscope, we can either decrease the wavelength of the electron beam or decrease the spherical aberration. We can increase the acceleration voltage to shorten the wavelength of electron beam, or use spherical aberration corrector (Cs-corrector) to reduce the aberration coefficient of objective lens in TEM.

The Cs-corrector is constituted of two hexapole electromagnetic lens and two double lens sets, as shown in Fig. 2-3[84]. We illustrate how the Cs-corrector works in Fig. 2-4[85]. With the existence of Cs-corrector, the electron beams passing through the electromagnetic lens focus on the same plane. Comparing to the situation without Cs-corrector, the electron beams cannot focus on the same point and hence cause the disk with a finite diameter of ~ 2 Å. With the Cs-corrector, the diameter of electron beam disk can reduced to 1 Å and the electron probe size will determine the spatial resolution in STEM.

With the help of Cs-corrector, we can obtain atomic-resolution spectrum imaging. We can minimize the pixel step range to make the simultaneously acquired HAADF images with atomic resolution. In this condition, we can clearly compare each EELS spectrum at certain pixel precisely to the atom positions, and reach to the chemical atomic

doi:10.6342/NTU202404787

mapping analysis.

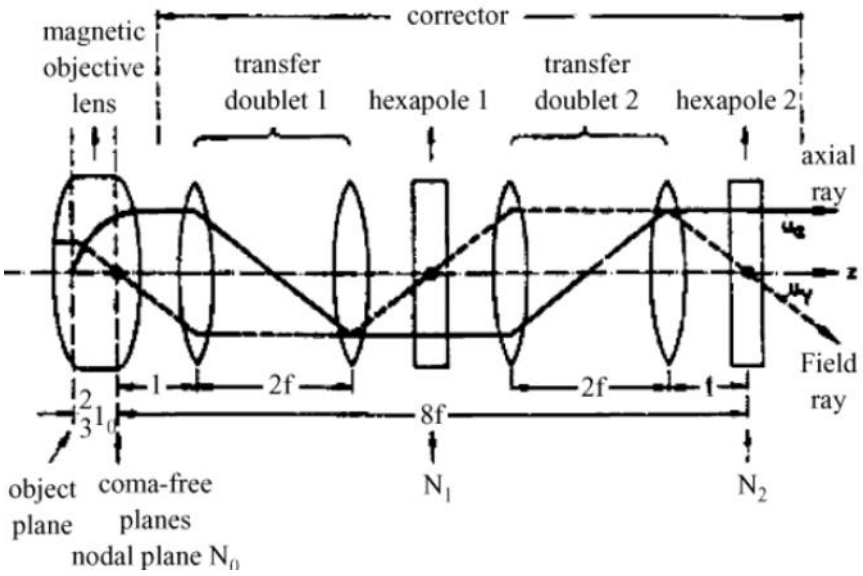

Figure 2-3 Structure of spherical aberration corrector[84].

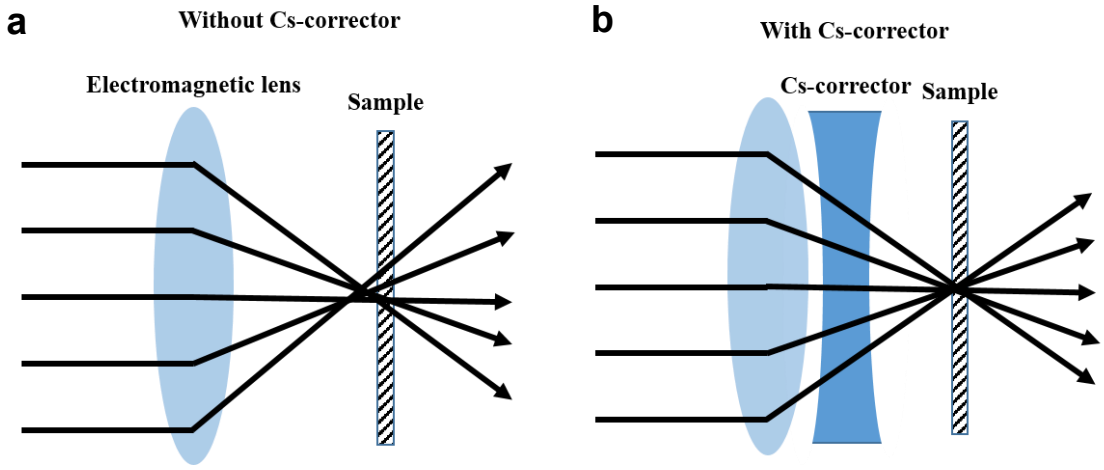

Figure 2-4 (a) The effect of spherical aberration and (b) the principle of Cs correction[85].

.

doi:10.6342/NTU202404787

2.2 Electron Energy Loss Spectroscopy (EELS)

Electron Energy Loss Spectroscopy (EELS) is a powerful and versatile analytical technique integrated into electron microscopy, enabling the study of the electronic, chemical, and structural properties of materials at atomic and sub-nanometer scales. EELS relies on the inelastic scattering of high-energy electrons as they interact with a specimen, resulting in a measurable loss of energy. By analyzing the energy distribution of these scattered electrons, EELS provides insights into the electronic structure, chemical composition, bonding states, and optical properties of the material[51,86-88].

EELS is based on the interaction of an incident electron beam with a material. When high-energy electrons pass through a thin specimen, they experience both elastic and inelastic scattering. While elastic scattering involves no energy transfer, inelastic scattering results in a loss of energy, with the magnitude of the loss determined by the nature of the interaction. The common interactions include phonon excitations, which electrons transfer energy to lattice vibration, resulting in low-energy losses. Then, plasmon excitations are the collective oscillations of free electrons in the material, typically seen in metals and semiconductors. Another interaction lies in interband transition. Energy transfer excites electrons from valence to conduction band. Core-level excitations are the electrons losing energy by exciting tightly bound core electrons to higher energy levels or the conduction bands.

In a typical EELS spectrum, it consists of distinct regions that correspond to various scattering processes. These regions provide complementary information to the materials. The first region is the zero-loss peak (ZLP). ZLP is a sharp peak near zero energy loss and represents electrons that have undergone 0 or minimal energy loss, which is elastic scattering. Its intensity and shape are used to calibrate the spectrum and determine the energy resolution. The second region is the loss-loss region. Low-loss region includes

doi:10.6342/NTU202404787

contribution from plasmon peaks and interband transitions, usually below 50eV. The last part is the core-loss region, which energy is above 50eV. The core-loss region contains ionization edges corresponding to the excitation of core electrons to the unoccupied states. The core-loss region peaks provide the unique signature for chemical analysis.

EELS is not only powerful for elemental analysis within core-loss region, but also capable of learning dielectric properties at the low-loss region. Due to the nature of the energy loss, the low-loss region EELS spectrum can be obtained from the loss function of dielectric function, which is the imaginary part of $(-1/\varepsilon(\omega))$, as[87]:

$$\text{Loss function } I = \frac{\varepsilon_2}{\varepsilon_1^2+\varepsilon_2^2} \tag{2.2}$$

EELS is essential tool for probing electronic, chemical, and structural properties of materials with atomic resolutions. Its ability to extract detailed information about bonding, electronic states, and compositional distribution makes it valuable in the characterization of advanced materials. By combining EELS with high-resolution imaging in STEM, we can achieve a comprehensive understanding of material properties at the nanoscale of material systems.

doi:10.6342/NTU202404787

2.3 Momentum-Dependent Electron Energy Loss Spectroscopy (q-EELS)

q-EELS is a special measurement dependent on the different momentum space to obtain EELS spectra at diffraction mode, and it is the most important method in our experiment. As indicated in Fig. 2-5, an incident beam with energy E_0 and momentum k_0 is subject to the inelastic scattering with the momentum q and energy (ΔE) transfer to the material. The scattering q can separated into $q_{\parallel}$ and $q_{\perp}$. The $q_{\parallel}$ is formulated by $q_{\parallel} = k_0\theta_{\Delta E}$, where the $\theta_{\Delta E}$ is the scattering angle being of $\theta_{\Delta E} = \frac{\Delta E}{2E_0}$. The $\theta_{\Delta E}$ is characteristically smaller and is much smaller than the Bragg's elastic scattering angle θ_B, which makes $q_{\parallel}$ to almost parallel to k_0. Therefore, $q_{\perp}$ is dominant for the scattering momentum q, which can be described as $q_{\perp} = k_0\theta$. The scattering momentum q will equal to $q = \sqrt{q_{\perp}^2 + q_{\parallel}^2}$.

The experimental setup for q-EELS is under the concept of obtaining the inelastically scattered electrons at the designated $q_{\perp}$, which between two Bragg's spots on the diffraction pattern. The chosen two Bragg's spots are determined by the crystal structure, which the symmetry line we are interested in reciprocal space. For ensuring the correct $q_{\perp}$ in the q-EELS probing, $q_{\perp}$ needs to be larger than the momentum resolution (Δq) limit of the instrument, meanwhile, Δq is also much larger than $q_{\parallel}$. In our experiment, the Δq is around 0.09 $Å^{-1}$ depending on the camera length and the EELS entrance aperture size. The EELS entrance aperture is a circular shape with the diameter 2.5 mm and the camera length (diffraction-pattern projection length) is 6.8m. In our CuTe material system, the $q_{\perp}$ is determined by 0.1 $Å^{-1}$ step along ΓX and ΓY. In this condition, $q = \sqrt{q_{\perp}^2 + q_{\parallel}^2}$ is nearly $q_{\perp}$ because $q_{\perp}$ is much larger than $q_{\parallel}$.

doi:10.6342/NTU202404787

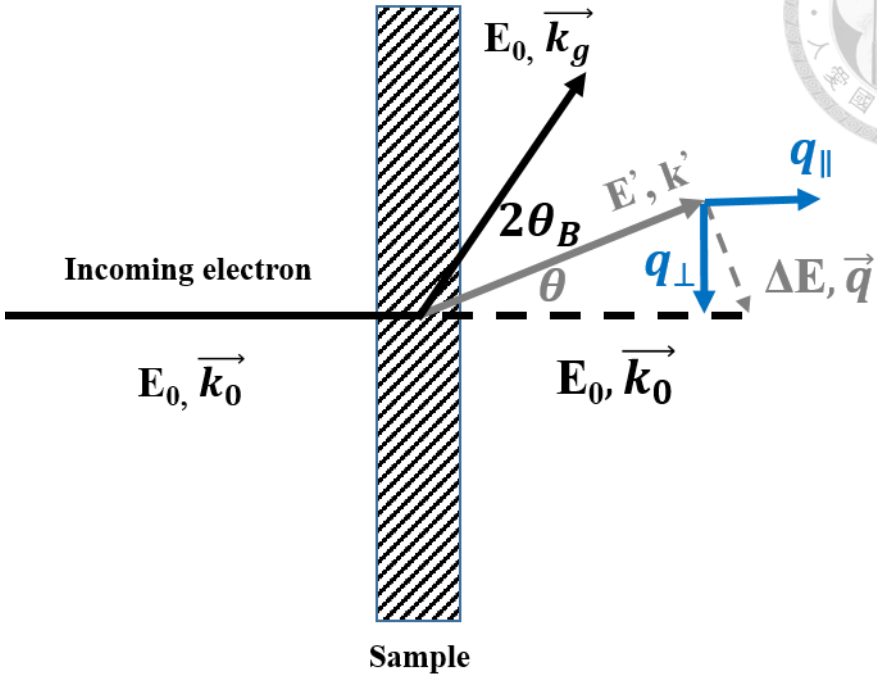

Figure 2-5 The inelastic electron scattering upon q-EELS. Because $q_\parallel$ is much smaller than $q_\perp$, $q_\perp$ is dominant the q in the q-EELS experiment.[87]

doi:10.6342/NTU202404787

Chapter 3 The Electronic Structure and the Momentum-Dependent Electron Energy Loss Spectroscopy (q-EELS) Probing on Copper Telluride (CuTe)

3.1 Introduction of CuTe

Copper telluride (CuTe) is a fascinating material that belongs to the family of metal chalcogenides, which have garnered significant attention due to their unique structural, electronic, and optical properties. As a compound of copper and tellurium, CuTe exists in various stoichiometric and non-stoichiometric forms, each exhibiting distinct properties that make it a versatile material for a wide range of applications. Its importance stems from its roles in thermoelectrics, optoelectronics, catalysis, and advanced energy storage systems[89-91].

The intrinsic properties of CuTe arise from the interplay between its crystal structure, electronic band structure, and chemical bonding. Copper telluride's ability to exhibit metallic, semiconducting, or even topological behavior under specific conditions highlights its potential for cutting-edge technologies. Additionally, the study of CuTe is enriched by its tunable electronic properties, achieved through doping, defect engineering, and variations in stoichiometry.

The electronic properties of CuTe are highly dependent on its stoichiometry and crystal structure. CuTe often exhibits semimetallic behavior with a high density of states near the Fermi level, contributing to enhanced electrical conductivity. CuTe typically crystallizes in a layered structure with weak van der Waals forces between layers and gives rise to unique anisotropic properties.

In Chapter 3, we report on the fundamental properties of CuTe including the crystal structure, electronic structure, and momentum-dependent electron energy loss

doi:10.6342/NTU202404787

spectroscopy (q-EELS) probing on the plasmons dispersion of different carriers along ΓX and ΓY with CDW presence[92-94]. With the theoretical calculation of energy loss function, we can simulate the plasmon dispersion and use the classical plasmon dispersion equation to calculate the effective mass and the Fermi velocity of the carriers near the Fermi level. Intriguingly, the result shows the obviously anisotropic properties of CuTe along ΓX and ΓY. The plasmon of carriers along ΓX exhibits a very light effective mass with the practically linearly dispersing band following the dispersion $\hbar v_{\mathrm{F}}\mathrm{q}$, influencing by the CDW presence[44,53]. In other hand, the heavy nature of the carriers along ΓY shows a thoroughly different plasmon dispersion, which proves the anisotropic phenomenon. The capability to obtain the effective mass and the Fermi velocity of the respective carriers simultaneously by q-EELS is exhaustively elucidated in the Chapter 3, where the method can give us more space to explore the quantum material systems.

doi:10.6342/NTU202404787

3.2 Experimental Procedure

3.2.1 Sample Preparation of CuTe

The CuTe crystals were grown by Professor C. S. Lue group. Single crystals of CuTe were grown by a Te self-flux method. The high-purity elements of Cu with concentration 99.99% and Te with 99.9999% were mixed with a molar ratio of 35% to 65%. The mixture was transferred to a fused quartz tube and sealed under vacuum. The quartz tube was heated up to 873 K for 10 hours, cooled to 703 K for 2 hours, and then slowly cooled down to 623 K at a rate of 1 K per hour. The excess flux was decanted with a centrifuge at 623 K and several platelet-like crystals with a typical size of $2 \times 3 \times 0.2\ mm^3$ were mechanically removed from the inner wall of quartz tube[95-98].

We used two steps preparing the TEM and q-EELS measurement samples of CuTe. First, we used the hand-polishing method with milling machine to make the sample surface smooth and reduce the roughness, as shown in Fig. 3-1(a) and 3-1(b), which photographs were taken under optical microscope. In Fig. 3-1(a), the surface of crystalline CuTe was roughness and crystal had several layers, which would prohibit our preparation procedure. Therefore, we milled the sample down to around 30 μm and polished to make the surface of crystal smooth, as shown in Fig. 3-1(b). When we take a closer look at Fig. 3-1(b), we can find the crystal of CuTe exhibits two different regions under optical microscope. One region contains purple stripes with purple arrows indicated in Fig. 3-1(b), and the other one are the general CuTe crystal. The stripe like regions have a different stoichiometry with Te loss and make the crystal as $Cu_{2.86}Te_2$ from CuTe.

After polishing the crystal of CuTe, we used tape to exfoliate the crystal. Usually, we use precision ion polishing system (PIPS) to final polish the crystal CuTe to thin enough sample. However, in our observation, we found that the CuTe crystal would transfer into the phase $Cu_{2.86}Te_2$ after PIPS procedure. Thanks to the layer structure of

doi:10.6342/NTU202404787

CuTe, we can use exfoliate method to reduce the thickness of the CuTe sample. After 50 times of exfoliation, the CuTe sample was thin enough to be observed under TEM and q-EELS experiment.

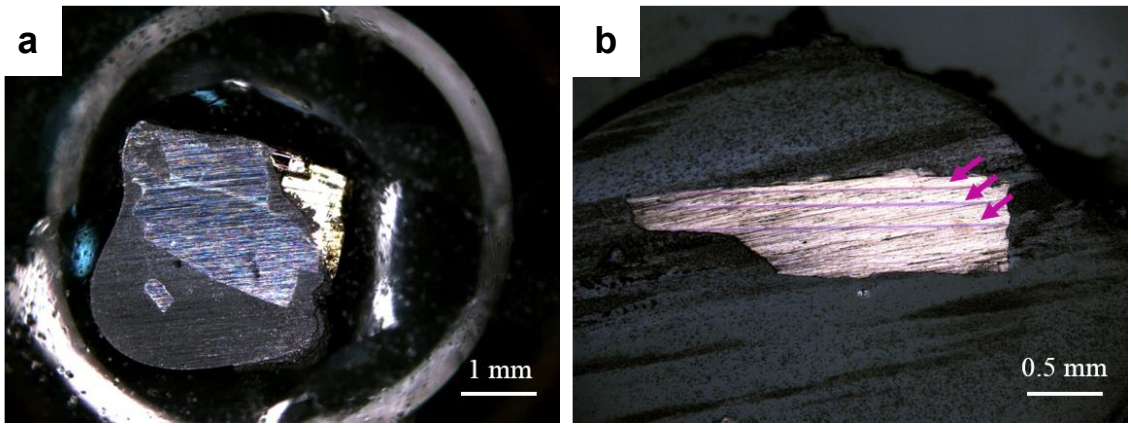

Figure 3-1 The photograph of CuTe crystal for TEM and q-EELS sample preparation. (a) CuTe crystal before mechanical milling. (b) CuTe crystal after mechanical milling. The purple arrows indicate the purple stripe phase of $Cu_{2.86}Te_2$[95].

doi:10.6342/NTU202404787

3.2.2 Atom Displacement Calculation by Atomap

As mentioned in the section 1.2.2, CDWs formation is simultaneously accompanied with the lattice distortion. The lattice distortion causes the periodic atom displacement, which causes the new modulation and the charge density wave. Therefore, calculating the atom displacement can provide us a deeper understanding of CDWs with the technique of HAADF images. Thanks to the Cs-corrector HAADF image, we have the atomic resolution to help us directly observe the modulation of lattice distortion.

We use the Atomap to calculate the atom displacement of CuTe structure. Atomap is a Python library for analyzing atomic resolution STEM images. It relies in fitting 2D Gaussian functions to every atomic column in an HAADF image, and automatically find all major symmetry axes. In this section, we will use $SrTiO_3$ (STO) as a standard example to elucidate the process of calculating the atom displacement in HAADF images[99-101].

The first step in using Atomap to analyze atomic resolution HAADF images is to find the position of the atomic columns in the image. In order to find the position of the atomic columns, we will need to find the feature separation. In Fig. 3-2, we demonstrate the process of feature separation. Fig. 3-2(a) is a STO image with the range 0.033 nm per pixel. Atomap finds initial atomic columns position by using a peak-finding algorithm from the Python package. The algorithm needs to know the smallest peak separation. By determining the smallest peak separation, Atomap will try to determine the position of atomic columns, shown as those red dots in Fig. 3-2(b).

doi:10.6342/NTU202404787

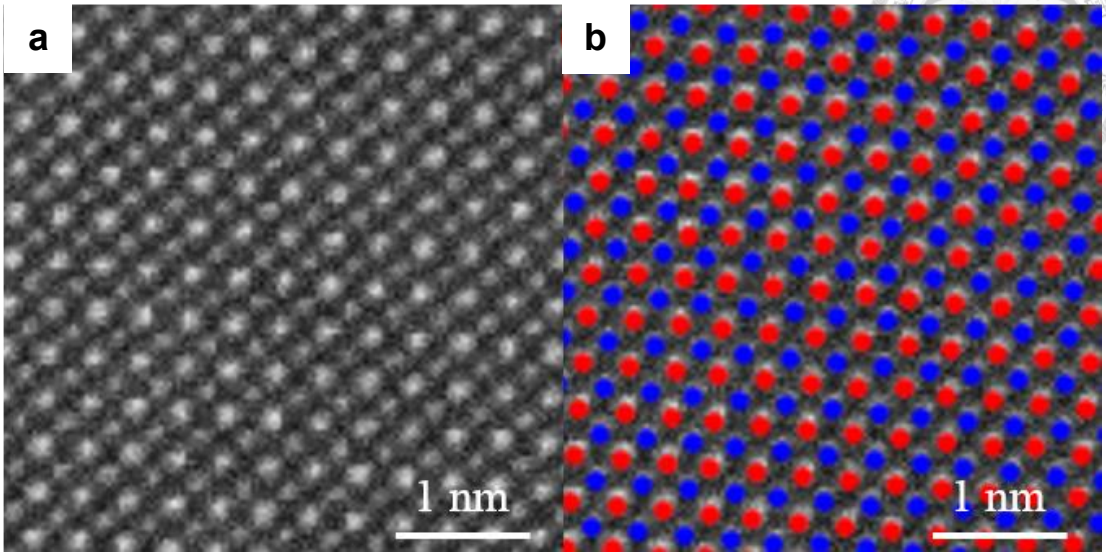

Figure 3-2 STEM HAADF images of STO. (a) The HAADF image of STO with the range 0.033 nm per pixel. (b) The HAADF image with defining the position of Sr and Te atomic columns. Red dots construct the Sr sublattice and blue dots construct the Te sublattice.

After having found the optimal feature separation, Atomap will help us to generate the initial atomic position. Those atomic positions will generate a list of x and y coordinates of initial atom position, which can help us form a sublattice in the HAADF images. In our example, we first locate the Sr atoms with feature separation, then Atomap will produce the coordinates of each red dots on the HAADF image and this will be the Sr atom sublattice. Once constructing the Sr sublattice, Atomap can help us remove the intensity of Sr sublattice in the corresponding HAADF image. The sublattice-removed image is shown in Fig. 3-3. Using the Fig. 3-3, we can easily define the position of Te atomic columns and construct the Te sublattice. The Te sublattice is defined as the blue dots on the Fig. 3-2(b).

doi:10.6342/NTU202404787

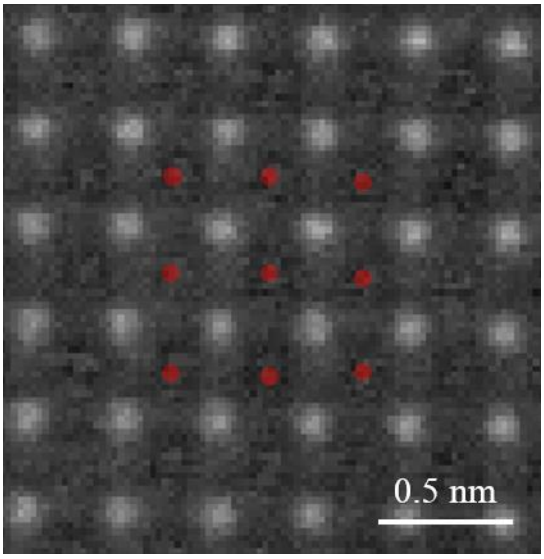

Figure 3-3 The Sr sublattice removed HAADF image. Red dots represent the Sr sublattice structure. The remain atomic columns construct the Te sublattice.

The above paragraphs illustrate the step to identify the position of the atomic columns on the HAADF images. Therefore, we can use the technique to calculate the atom displacements in the CDW system. Because of the CDW formation, the lattice distortion creates a new periodic modulation, which causes the superlattice spots on the diffraction pattern. In Fig. 3-4, we show the Fast Fourier Transform (FFT) of the HAADF image of CuTe. We can observe the superlattice points between the Bragg's spots. We can use the "mask" operation from the DigitalMicrograph (DM) to select the certain diffraction spots on the FFT pattern to reconstruct the HAADF image. Fig. 3-4(a) is the FFT from the HAADF image, and Fig. 3-4(b) is the FFT pattern applied with masks of specific diffraction spots we want.

doi:10.6342/NTU202404787

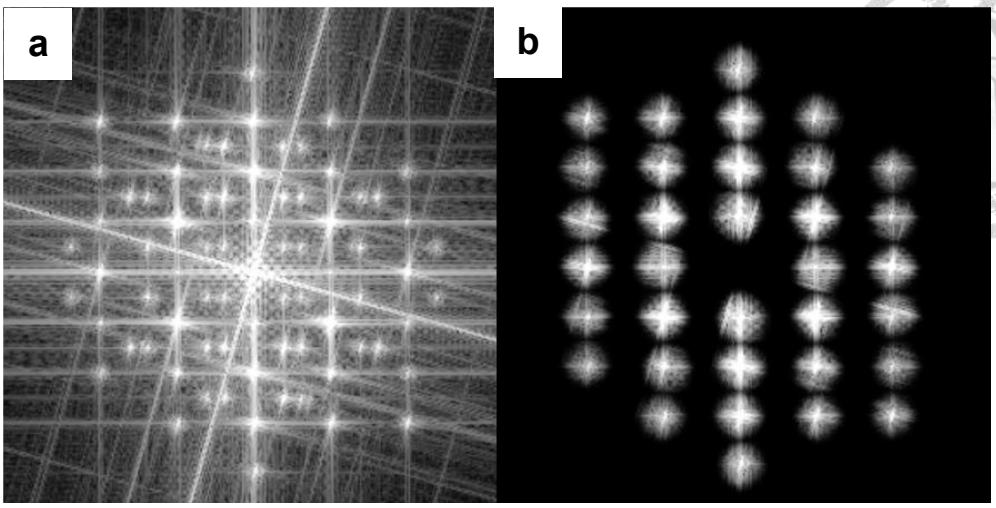

Figure 3-4 The FFT pattern of HAADF image of CuTe. (a) The FFT pattern from the HAADF image. (b) The FFT pattern with the circular masks applied on certain diffraction spots.

We can reconstruct the HAADF image from the masked FFT pattern. The image reconstructed from Fig. 3-4(b) only contains the information of Bragg's spots, which exclude the interference from superlattice spots. We can regard the reconstructed image as the reference image. Then, we reconstruct the HAADF image with all the diffraction spots, containing superlattice spots, which obtain the information of CDW formation and periodic modulation. Subsequently, we use Atomap to define the position of Te atomic columns in two reconstructed images, respectively. Finally, the difference between the positions of Te atomic columns is the lattice displacement with CDW formation.

doi:10.6342/NTU202404787

3.2.3 q-EELS Experiment Setup

The fundamental of q-EELS measurement is illustrated on section 2.4. Here, we will go through the details of the experimental setup. Fig. 3-5 shows the schematic illustration of our q-EELS probing on CuTe sample.

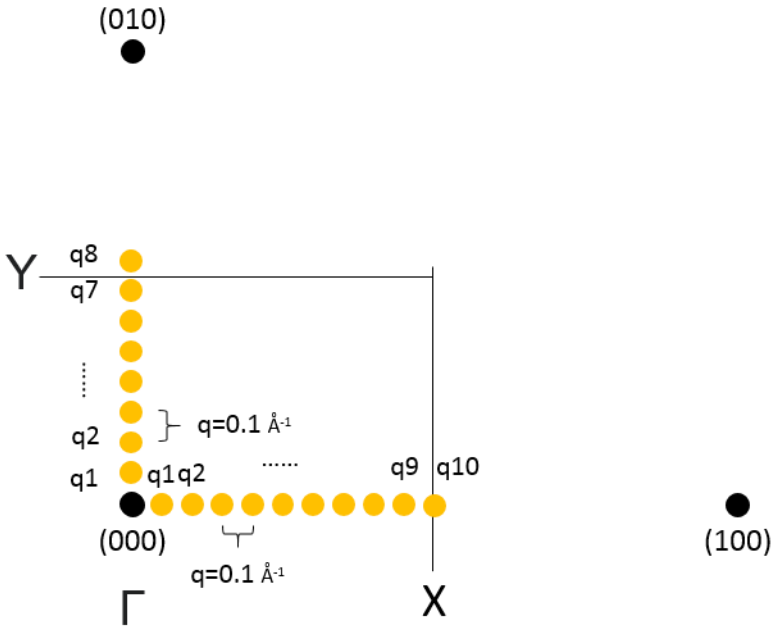

Figure 3-5 The schematic illustration of q-EELS experimental setup.

In the Fig. 3-5, we use q-EELS probing the CuTe along ΓX and ΓY. The black dots are the Bragg's spots of the CuTe. The Γ, X, and Y denote the specific symmetry point in the momentum space as the Brillouin zone boundary. The yellow circles in Fig. 3-5 are the positions where we acquire the EELS spectra with the step of 0.1 $Å^{-1}$. The momentum resolution under the camera length (diffraction-pattern projection length), which is 6.8m, is around 0.09 $Å^{-1}$ with the EELS entrance aperture 2.5 mm in diameter.

doi:10.6342/NTU202404787

We use diffraction pattern to help us control the incident beam at the momentum position we want. There are 10 spots and 8 spots along ΓX and ΓY, respectively. At each spot, we acquire nine spectra to increase the signal to noise ratio and the peak intensity. After acquiring nine spectra, we use ZLP to align and then sum them together. All the spectra in the chapter 3 and 4 follow the acquisition condition.

doi:10.6342/NTU202404787

3.3 Results and Discussion

3.3.1 The Crystalline and Electronic Structure of CuTe

CuTe has been proved as a unique charge density wave (CDW) system with the CDW transition temperature (T_{CDW}) at 335K. CuTe has an orthorhombic crystal structure with space group Pmmn and lattice parameter which a = 3.149, b = 4.086, and c = 6.946 Å[96]. CuTe has drawn attention because of its two-dimensional (2D) layered structure owning quasi-one-dimensional (quasi-1D) CDW order. When the temperature is above T_{CDW}, CuTe maintains orthorhombic structure with weakly binding along c axis. When CuTe turns into CDW state, only the distortion of Te-atom chains along a axis involve the CDW formation. Fig. 3-6(a) shows the unit cell (gray rectangle) of CuTe in the non-CDW (normal) state consisting of Te atoms along a axis and the zig-zag like Cu nets in the ab-plane.

Fig. 3-6(b) demonstrates the atomic-scale image of CuTe at CDW state under 300K using scanning transmission electron microscopy (STEM). We specifically put the attention on the Te atoms displacements which take the dominant role on the CDW order. The inset of the Fig. 3-6(b) shows the displacements length of the Te atoms which the red (blue) arrows indicate up-pointing (down) inside the characteristic 5a × 2c superlattice (white rectangle in the Fig. 3-6(b)) corresponding to the CuTe $q_{CDW} = [0.4a^*, 0, 0.5c^*]$[96-97,102-105]. By classifying the red and blue arrows, we can separate the STEM image into sets of trapezoids. The two neighbored trapezoids show the anti-phase displacement direction consisting to the sinusoidal waves demonstrating the CDW order and suggest the condensed soft phonon mode[103].

In Fig. 3-6(b), the periodicity of the displacements (arrows) do not repeat perfectly every 5a × 2c superlattice is due to the effects of noised and the stability of the TEM. The finite sample drifts and mechanical vibration are the origins of the imperfection of the

doi:10.6342/NTU202404787

images acquisition. Our picometer-level evaluations of the atomic displacements cause these effects of small mechanical noises. However, these noises do not influence the present of the characteristic q_{CDW} = [0.4a*, 0, 0.5c*] of the image.

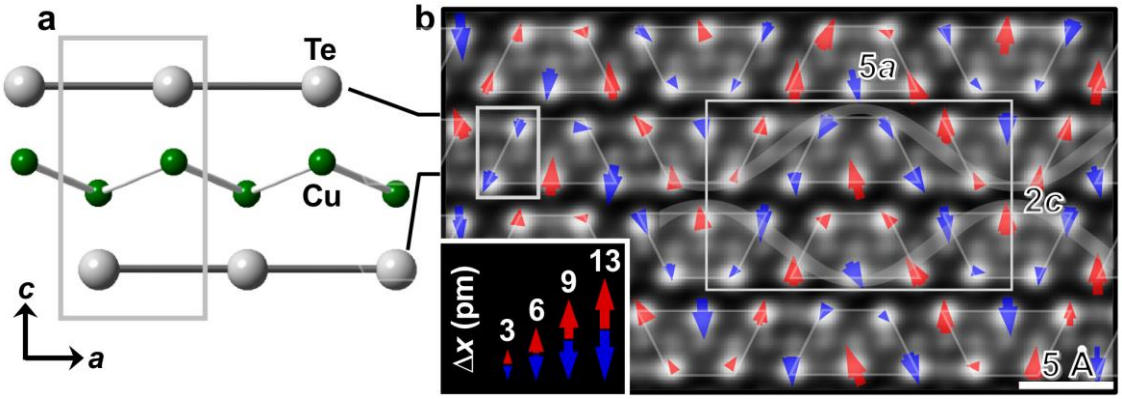

Figure 3-6 Lattice of structures of normal state and CDW state CuTe. (a) b-projected crystal structure in the normal state. The gray rectangle indicated the unit cell of CuTe. (b) STEM imaging of the CDW-state of CuTe at 300 K. The gray thin rectangle indicated the CDW supercell of 5a × 2c with systematic Te displacements (Δx, calculated Te displacements using atomic coordination by Atomap). The displacements can be separated into rows of trapezoids along a axis which show anti-phase direction in one trapezoid compared to the neighboring one, causing the sinusoidal wave-like pattern following the periodicity of 5a. Except along a axis, the Te displacements along c axis are also inversed which lead to the 2c periodicity.

In Fig. 3-7(a), we show the element-, orbital-decomposed band diagram of the normal state CuTe. There are three dispersive bands crossing the Fermi level which are denoted as Te-p_x, p_y and p_z orbital, in the color of red, blue, and yellow respectively[106-110,]. The black solid curves underneath, which are more flat below 2 eV, are contributed by the Cu 3d states. We can realize that the band dispersion is dominated by the Te-p_x and p_y bands

doi:10.6342/NTU202404787

near the Fermi level.

Fig. 3-7(b) and 3-7(c) are the enlarge images from the Fig. 3-7(a) which represent the CDW-state CuTe band structure along ΓX and ΓY, respectively. Fig. 3-7(b) and 3-7(c) comes from the light and heavy gray rectangle in the Fig. 3-7(a), respectively. In the Fig. 3-7(b), we can see that the one of the two practically linearly dispersing Te-p_x bands dominates the CDW-gap opening at the Fermi level. Fig. 3-7(d) denotes the high-symmetry points at the momentum space and the Fig. 3-7(e) displays the Femi surface (FS) of the normal-state CuTe. The quasi-1D arrangement of Te atoms results in anisotropic dispersion of the metallic bands, which are near the Fermi level. The weakly bonding along c* axis causes the dispersion is strongly reduced. The quasi-1D like FS, which is parallel to the ΓY direction, is contributed by the Te quasi-1D chain. In the 3D view, it becomes two-sheet like FS parallel to the b*-c* plane cover the whole Brillouin zone. From the sheet-like FS toward the face of the Brillouin zone along a* direction, there are two quasi-2D cylindrical FS centered around the X point. Other further applications, such as exchange-correlation functional, local field effects, and on-site Coulomb repulsions have slight impacts on these electronic structures[106], which reveals the weak-correlation properties of CuTe.

doi:10.6342/NTU202404787

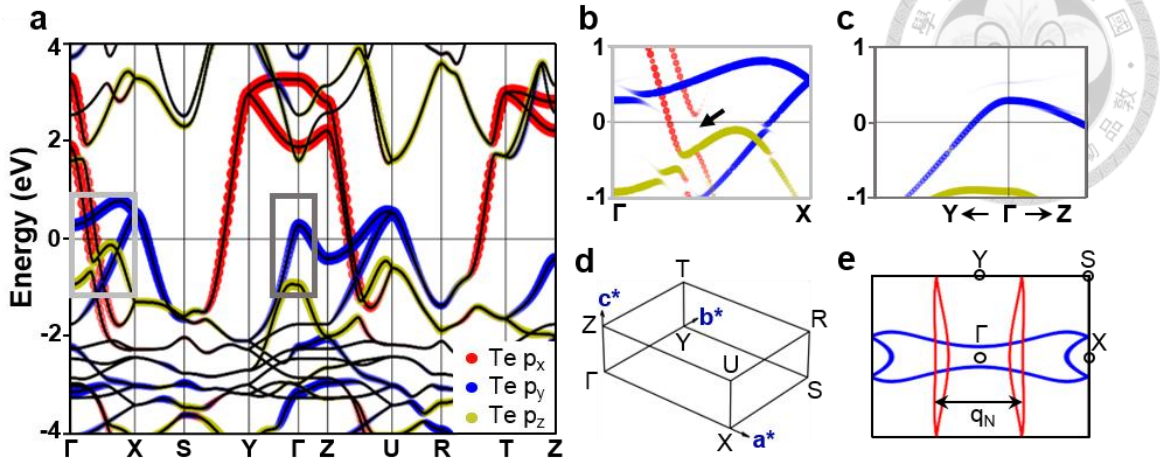

Figure 3-7 Electronic structures of normal- and CDW-state CuTe. (a) Electronic structure of normal-state CuTe. Color with black solid curves underneath represent the orbital decomposed Te-p bands, Black solid curves without color overlays are Cu 3d bands. Fermi level locates at energy 0 eV. (b) and (c) Blowups of the CDW-state electronic structure along ΓX (the light gray rectangle in (a)) and ΓY (the dark gray rectangle in (a)). The arrow in (b) indicates that CDW-gap opening is dominated by the practically linearly-dispersing Te-p_x band. (d) The high-symmetry points and the directions in the reciprocal space. (e) FS projection onto the X-Γ-Y plane at c* = 0. The Te-p_x bands (red) are two sheet-like across the Γ point and are prone to cause FS nesting by q_N = 0.78 Å^{-1}. The Te-p_y bands (blue) are cylindrical across the X point and form a hole pocket[106-108].

As mentioned above, the electronic characteristic behavior of CuTe is predominantly by the Te-p_x practically linearly-dispersing band (red band in Fig 3-7(a)), signifying to the weak correlations and small effective mass (m*) of carriers[106,111-112]. On the other hand, the parabolic Te-p_y bands (blue) near the Fermi level indicates the carrier has sufficient effective mass. Indeed, Te-p_x (p_y) bands are suggested to carry an electron (hole) character with a light (heavy) band mass. Around the Fermi level, the CDW gap opens at certain Te-p_x state, while the Te-p_y bands remain intact. In additional, the FS nesting vector, q_N, matches the projected a* vector of q_{CDW}, which strengthens the FS nesting phenomenal

doi:10.6342/NTU202404787

in the CDW-state of CuTe[96]. Therefore, the Te-p_x light electron carriers are crucial to the CDW and we are going to elaborate on m* and v_F of the light electron plasmons along the ΓX direction. As a comparison group, the heavy hole plasmons along ΓY direction is also investigated.

doi:10.6342/NTU202404787

3.3.2 Capturing Effective Mass (m*) and Fermi Velocity (v_F) of the Te-p_x Light Electrons and the Te-p_y Heavy Holes.

In Fig. 3-8(a), we show the selected-area electron diffraction (SAED) of CuTe in the ΓX-ΓY plane of the CDW-state at 300K, with the Brillouin zone boundary X of ~1.0 $Å^{-1}$ and Y of ~0.77 $Å^{-1}$. The CDW wave vector, q_{CDW}, is also shown, of which the length is 0.4 a* projected along ΓX direction. Because the CDW wave vector has the component of 0.5 c*, the q_{CDW} locates at the 0.5 c* plane next to this plane resulting in the weak and streaky line in the SAED pattern due to the electron Ewald sphere intercepting. Therefore, the q_{CDW} can be clearly seen at the SAED pattern from the viewing direction along b*, as shown in Fig. 3-8(b). The superlattice points in the Fig. 3-8(b) is sharp without clear stripe are because the Ewald sphere intersects the q_{CDW} more specifically along b* direction. For Fig. 3-8(c), it is the power spectrum of the parent image comprising of Fig. 3-6(b). We can see the sharp and obvious superlattice points in Fig. 3-8(c) which represents that the CDW periodicity is solid to 5a × 2c although there are unavoidable noises when acquiring STEM images.

doi:10.6342/NTU202404787

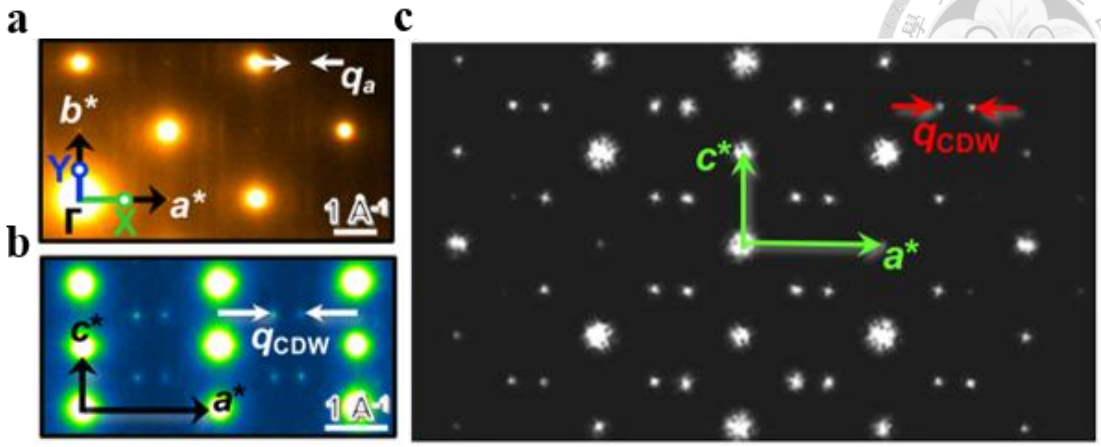

Figure 3-8 The SAED pattern of CDW-state CuTe. (a) The SAED pattern incident along c* direction. X and Y represent the first Brillouin zone boundary. q_a is the projected a-component of q_{CDW} onto the plane. (b) The SAED pattern incident along b* direction with the directly observation of q_{CDW}. (c) The power spectrum of the parent image of Fig. 3-6(b) which displays the clear and sharp superlattice points, just like (b). Even though the mechanical instability and noises persist when acquiring STEM images, the 5a × 2c q_{CDW} is still robust appearing on the image. Our picometer-level evaluation of the atomic displacements makes these effects observable by the imperfection periodicity of arrow in trapezoids in Fig 3-6(b).

Electron energy loss spectroscopy (EELS) probes electronic excitations and the loss function, $\mathrm{Im}\left\{\frac{-1}{\varepsilon(\omega,q)}\right\}$ with $\varepsilon(\omega,q)$ being the frequency (ω) - and momentum (q) - dependent complex dielectric function. The loss function will diverge when dielectric function equals to zero, which means $\varepsilon_1 = 0$ and meanwhile the frequency depicts the initiation of the collective electron excitation, namely plasmon frequency (ω_p)[69,113]. Generally, the plasmon excitation frequency in bulks can be written as equation (3.1),

$$\omega_p = \sqrt{\frac{4\pi ne^2}{m^*\varepsilon_\infty}} \tag{3.1}$$

where n is the bulk carrier density, e is the electron charge, m* is the effective mass, and the ε_∞ is the screening dielectric constant by the presence of single-particle transitions

doi:10.6342/NTU202404787

above the plasmon. Through using EELS, we can get the plasmon frequency resulting in resolving m* by knowing the temperature-dependent n and the dielectric constant are known[114-116].

Using momentum-resolved EELS (q-EELS) at 300K, we observed the Te-p_x light-electron plasmon at 2.85 eV along ΓX at q = 0.1 $Å^{-1}$ and the Te-p_y heavy-hole plasmon at 1.86 eV along ΓY, as shown in Fig. 3-9(a) and 3-9(b). The light-electron and heavy-hole plasmons along ΓX and ΓY are observable at q = 0.1 $Å^{-1}$, instead of q = 0 $Å^{-1}$. The reason is because the zero loss peak at q = 0 $Å^{-1}$ has a strong tail which intensity buries the plasmons peak inside the low-loss region.

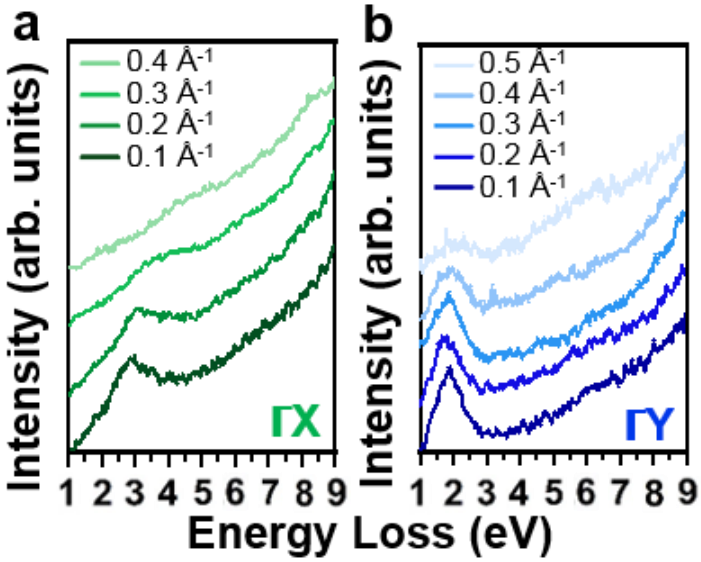

Figure 3-9 q-EELS along ΓX and ΓY of CDW-state CuTe. (a) and (b) q-EELS measurements of the dispersion of Te-p_x light-electron (Te-p_y heavy-hole) plasmon along ΓX (ΓY).

doi:10.6342/NTU202404787

Fig. 3-10 shows the theoretical calculated complex dielectric function and the EELS loss function of the CDW-state CuTe along ΓX and ΓY at c. The insets in Fig. 3-10(a) and 3-10(b) are the enlarge images of dielectric function near the bulk plasmon frequency around 17 eV. Both EELS results along ΓX and ΓY follow the same trend of the loss function calculated by the RPA complex dielectric functions. We can observe that the ε_1 equals to zero two times in the Fig. 3-10(a) and 3-10(b). For Fig, 3-10(a), ε_1 equals to zero at around 3 eV and 17 eV, which relates to the Te-p_x light-electron plasmon and the bulk plasmon, respectively. The same phenomenal also takes place along ΓY with Te-p_y heavy-hole plasmon and the bulk plasmon as well.

doi:10.6342/NTU202404787

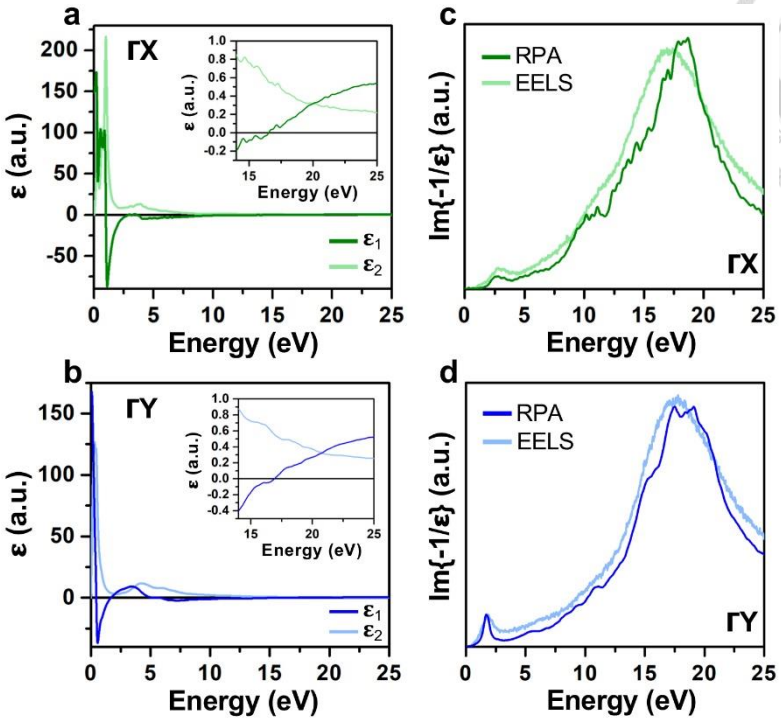

Figure 3-10 Theoretical complex dielectric function and EELS loss function of the CDW-state of CuTe. (a) and (b) The complex dielectric functions ($\varepsilon = \varepsilon_1 + i\varepsilon_2$) calculated within the framework of RPA at q = 0.1 $Å^{-1}$ along ΓX and ΓY, respectively. Insets, blowups of the bulk plasmon region, which display that there is no remarkable single-particle transition above the collective-excitation onset at $\varepsilon_1 = 0$. (c) and (d) The comparison between the loss function from dielectric function and the experimental EELS spectra at q = 0.1 $Å^{-1}$ along ΓX and ΓY, respectively.

A recent theoretical work suggests that the Te-p_x light-electron (Te-p_y heavy-hole) plasmon peak located at ~2.9 eV (~1.9 eV) around q = 0.1 $Å^{-1}$, which is caused from the intraband transition of the Te-p_x (Te-p_y) states. Fig. 3-11 shows the impact of intraband transitions with the light-electron and heavy-hole plasmons[106]. We decompose the electronic band structure into three categories: fully occupied bands (FO, red), partially occupied or partially unoccupied bands (PO or PU, blue), and the fully unoccupied bands (FU, green). In Fig. 3-11(a), we show four different kinds of single-particle transition by

doi:10.6342/NTU202404787

the arrows at the right side. Cyan arrow, the interband transition from FO to PU states. Purple arrow, the interband transition from PO to FU states. Dark green arrow, the interband transition from FO to FU states. Light olive arrow, the intraband transition from PO to PU states. For Fig. 3-11(b) and 3-11(c), we demonstrate ε_1, four kinds of single-particle transition, and EELS spectra times 100 in order to make it observable in the same scale at q = 0.1 $Å^{-1}$ of CDW-state CuTe along ΓX and ΓY, respectively. As mentioned above, the collective plasmon excitation takes place at $\varepsilon_1 = 0$. From Fig. 3-11(b) and 3-11(c), we find out the light-electron plasmon and heavy-hole plasmon are mainly related to the respective intraband transition (light-olive curve) of Te-p_x and Te-p_y bands. The corresponding ε_1 (light-olive curve) represents the only component which does not cross the $\varepsilon_1 = 0$ is in support of plasmon excitation. The other three interband-transition (cyan, purple, and dark green curves) ε_1 components are responsible for the screening of intraband transition (light-olive curve), resulting in the total electronic contributions (black curve) cross the $\varepsilon_1 = 0$ at a much lower energy than only consider intraband transition effect.

doi:10.6342/NTU202404787

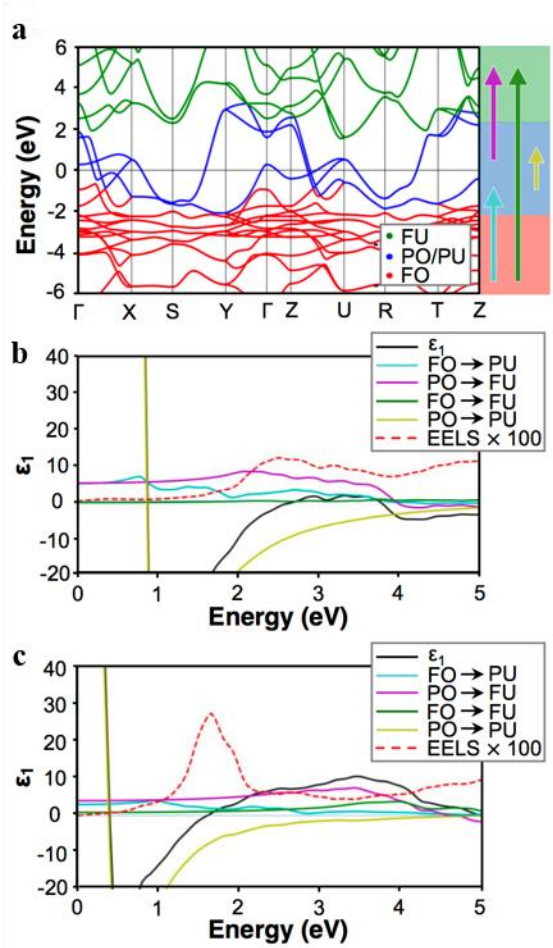

Figure 3-11 Correlations of intraband transitions with the light-electron and heavy-hole plasmons. (a) Decomposing the electronic structure into three categories: FO, PO/PU, and FU. (b) Breakdowns of the real part of the complex dielectric function (ε_1, black curve) along ΓX into individual contributions from the interband and intraband transition (same color codes in Fig. 3-11(a)). (c) Same as (b) while along the ΓY direction.[58-60]

In order to resolve the m* of the Te-p_x light electrons, we need to first obtain the ε_∞ of the light-electron plasmon in both the CDW-state and normal-state using Drude-Lorentz (DL) model of the theoretical dielectric function, as shown in Fig 3-12[117]. Using DL model to simulate the RPA theoretical dielectric function can help us obtain the theoretical plasmon frequency and consider the single-particle transition screening impact on the dielectric function.

doi:10.6342/NTU202404787

The equation (3.2) used to simulate is[114]:

$$\varepsilon(\omega) = 1 - \frac{\omega_P^2}{\omega^2 + i\gamma_P\omega} - \frac{\omega_\Delta^2}{\omega^2 - \omega_\Delta^2 + i\gamma_\Delta\omega} - \sum_{l=1}^{4} \frac{\omega_{T,l}^2}{\omega^2 - \omega_{T,l}^2 + i\gamma_{T,l}\omega} \quad (3.2)$$

The second term of the equation represents the free-electron-gas (FEG) Drude component, with ω_p and γ_P denoting as plasmon frequency and damping constant, respectively. The third term is the single-particle Lorentz contribution due to the excitation across the CDW gap opening (Δ), with ω_Δ being the corresponding CDW gap opening size and γ_Δ being the corresponding damping constant. The forth term is responsible for the Lorentz contribution of three absorptions below 2 eV in RPA calculation and one single-particle excitation above the plasmon energy, with $\omega_{T,l}$ denoted as oscillator strength and $\gamma_{T,l}$ denoted as damping constant. All the parameter fitting to the theoretical RPA ε_2 using equation (3.2) for the normal-state and CDW-state are listed in Table 3.1.

Table 3-1 The physical parameters for the DL modeling of $\varepsilon(\omega)$ for the normal-state (335 K) and the CDW-state (300 K). All units in eV.

Phase	ω_P	γ_P	ω_Δ	γ_Δ	ω_{T1}	γ_{T1}	ω_{T2}	γ_{T2}	ω_{T3}	γ_{T3}	ω_{T4}	γ_{T4}
Normal	3.25	0.01	0	0.2	0.27	0.2	0.59	0.25	0.92	0.11	4.5	5.5
CDW	3.15	0.01	0.05	0.2	0.27	0.1	0.66	0.4	0.99	0.2	4.5	6.3

doi:10.6342/NTU202404787

The inset of Fig 3-12 shows the ε_2 of RPA calculation and the DL model fitting in the 0 to 3 eV energy region. Using the result obtained by the DL model, the corresponding loss function are examined with the RPA theoretical calculated loss function and the representative EELS spectra at CDW- 300 and normal- 335K along ΓX at q = 0.1 $Å^{-1}$. The consistency among the three indicates the satisfactory of DL model.

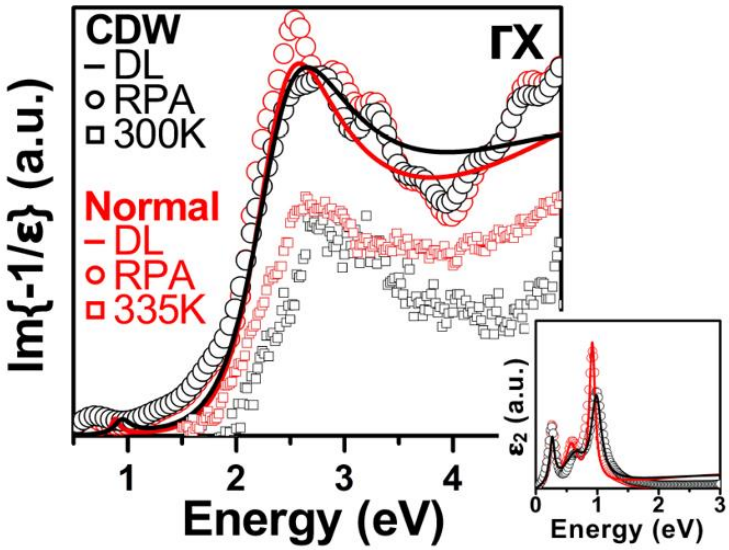

Figure 3-12 The DL model-derived loss function compares with RPA theoretical calculation and the corresponding EELS spectra of normal- 335 ad CDW- 300 K along ΓX at q = 0.1 $Å^{-1}$. The RPA-theoretical loss function of the Te-p_x light-electron plasmon along ΓX in the normal state (red) and the CDW-state (black). Open circles are the RPA calculations. Open squares are the EELS spectra at 335 K (red) and 300 K (black). Inset, the corresponding imaginary part of dielectric function (ε_2) is predominated by the three absorptive peaks under 2 eV. Black and red lines inside the figure and inset are the DL model fitting using the parameters in the Table 3-1.

doi:10.6342/NTU202404787

Via the aid of DL model fitting result, we obtain the Drude-ω_p component value as 3.25 eV in normal-state and 3.15 eV in CDW-state of CuTe along ΓX at q = 0.1 Å^{-1}. By following the equation (3.3) below, we can obtain the ε_∞[69].

$$\omega_P^{q\to 0} = \frac{\omega_P}{\sqrt{\varepsilon_\infty}} \tag{3.3}$$

The $\omega_P^{q\to 0}$ represents the linearly extrapolated value of plasmon frequency at q = 0 Å^{-1}. The ω_P is the result we obtain in DL model fitting, then we can get the ε_∞. The methodology of capturing $\omega_P^{q\to 0}$ and the corresponding ε_∞, m*, n, and v_F is demonstrated below. Actually, the momentum-dependent plasmon dispersion can obtain the Fermi velocity, effective mass, and carrier density. However, many q-EELS literatures do not tell this information[118-128]. The method is shown below.

In a bulk material with dense carrier density, the kinetic energy of electrons ($E_F \sim n^{2/3}$) dominates the inter-particle potential energy and the charges move like a free electron gas (FEG)[113]. RPA in this FEG contexts describing the plasmon dispersion, with the factor of v_F by the equation (3.4)[69,113],

$$\omega^2 = \omega_p^2 + \frac{3}{5} v_F^2 q^2 \tag{3.4}$$

Generally, equation (3.4) is derived for classical, massive electron system with the parabolic band-dispersion which $E = \frac{\hbar^2 k^2}{2m^*}$, relating to the Fig. 3-7(a) to 3-7(c)[130]. Considering the massless condition, such as Dirac fermion which located at the crossed nodal point of the linearly-dispersion bands with dispersion $\hbar v_F q$ [130-132], the corresponding long-wavelength ω_P at q = 0 Å^{-1} becomes non-classical and will be proportional to $1/\sqrt{\hbar}$. However, the plasmon dispersion still follow the q^2 dependence. Talking to CuTe condition, its unique electron band structure only has the linearly-dispersing bands instead of linearly-band crossing which is rather designated for the characteristically small m* of Te-p_x light-electron plasmon than a massless

doi:10.6342/NTU202404787

character[106,111-112]. Hence, the finite small m* of Te-p_x light-electron plasmon and the Te-p_y heavy-hole plasmon are suitable to use equation (3.4) to describe the plasmon dispersion.

In particular, the slope (A) of $\omega^2 - q^2$ scaling of equation (3.4) is proportional to v_F^2, which gives us the important clue to probe v_F. Meanwhile, the intercept to q = 0 $Å^{-1}$, which gives the clue to $\omega_P^{q\to 0}$ is a function of m*. By transforming the equation (3.1), we can get

$$m^* = \frac{4\pi n e^2}{\omega_p^2 \varepsilon_\infty} \tag{3.5}$$

Then we can consider the Fermi velocity in the 3D system by the equation,

$$v_F = \frac{\hbar(3\pi^2 n)^{1/3}}{m^*} \tag{3.6}$$

where $\hbar$ is the Plank constant and the n is the carrier density.

Using the proportional relation from A to v_F^2, we can obtain the carrier density by the equation,

$$n \sim \frac{\omega_p^3 \cdot \varepsilon_\infty^{3/2}}{A^{3/4}} \tag{3.7}$$

By resolving the carrier density n, we can yield m* directly and v_F becomes accessible.

In Fig. 3-13(a), we show the $\omega^2 - q^2$ scaling of the dispersions of Te-p_x light-electron, Te-p_y heavy-hole, ΓX bulk, and ΓY bulk plasmons from the Fig. 3-13(b), 3-13(c), 3-13(d), and 3-13(e). With the proportional relation between the slope (A) and the v_F^2 by equation (3.4), the linearity relation in Fig. 3-13(a) $\omega^2 - q^2$ scaling shows that those plasmons follow the FEG character despite the CDW order. These FEG character also satisfies the weak-correlation relation as mentioned in Fig 3-7.

Using the experimental slope A we obtain from Fig. 3-13(a) of the light-electron plasmon along ΓX, we can get the carrier density n = 2.01 × 10^{21} cm^{-3} of the Te-p_x light

doi:10.6342/NTU202404787

electrons. Following the intercept of extrapolation, the $\omega_P^{q\to 0}$ is 2.65 eV when q = 0 Å^{-1}. By using the equation (3.3), we can use $\omega_P^{q\to 0}$ and the ω_P from DL model calculating the ε_∞ for Te-p_x light-electron plasmon, which is about 1.41. After that, we can obtain the m* = 0.28 m_0 afterwards. With the known m* and n, the fermi velocity v_F = 1.61 × 10^8 cm s^{-1} and the Fermi energy E_F ~ 2.07 eV are derived as summarized at Table 3-2, with the same results calculated for Te-p_y heavy-hole plasmon. For the heavy-hole plasmon, we can also adopt ε_∞ = 1.41 owing to the likewise appearance of interband transitions above the plasmon, seen in Fig. 3.5d. The valence electrons for the isotropic ΓX and ΓY bulk-plasmon dispersion are of m* = 1.12 m_0 with n = 2.37 × 10^{23} cm^{-3} in average.

Table 3-2 The physical parameters of Te-p_x light-electron and Te-p_y heavy-hole plasmons from the respective dispersion at CDW-state 300 K.

Physical Parameters	Te-p_x light electrons	Te-p_y heavy holes
Effective mass m* (m_0)[I]	0.28	3.41
Carrier density n (cm^{-3})	2.01 × 10^{21}	1.19 × 10^{22}
Carrier density n, Hall (cm^{-3})[II]	7.34 × 10^{21} (//a)	1.16 × 10^{22} (//b))
Fermi velocity v_F (cm s^{-1})	1.61 × 10^8	0.24 × 10^8
Fermi wave vector k_F (Å^{-1})	0.39	0.71
Critical wave vector q_c (Å^{-1})	0.3	1.39
Fermi Energy E_F (eV)	2.07	0.56

[I] The intercepted $\omega_P^{q\to 0}$ of the Te-p_y heavy-hole plasmon is 1.85 eV.

[II] Result from the Hall measurements, shown in Fig. 3-14. The positive sign of carrier density along both ΓX and ΓY direction represents the hole carrier takes predominant contribution in transport properties.

doi:10.6342/NTU202404787

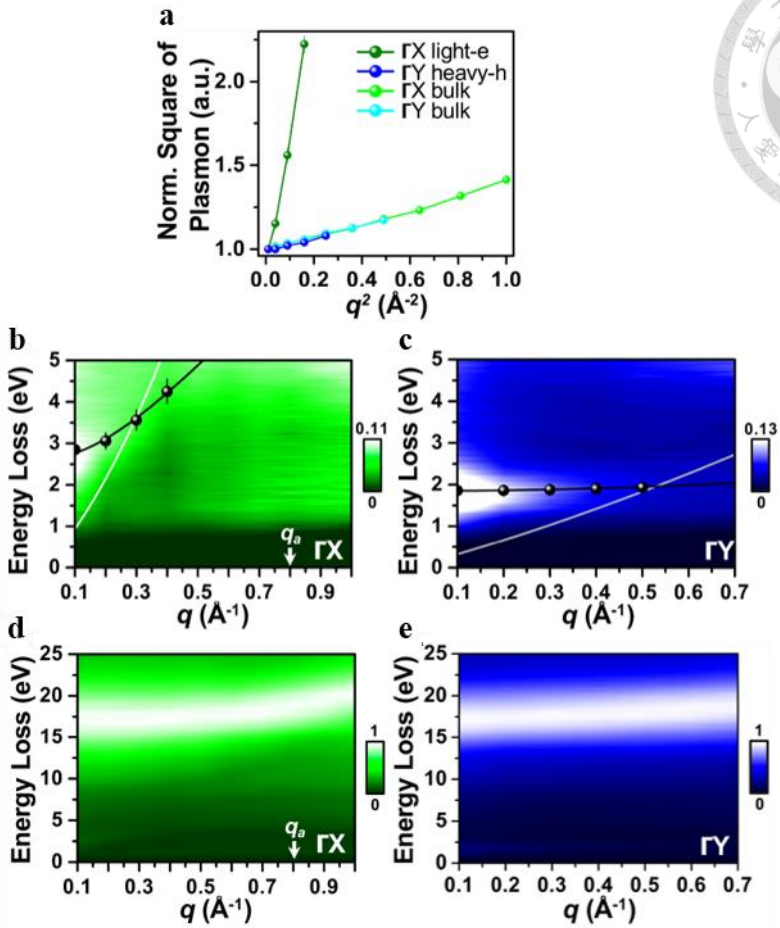

Figure 3-13 q-EELS investigations of plasmon dispersions in the CDW-state of CuTe at 300K. (a) The $\omega^2 - q^2$ scaling of the dispersion of ΓX light-electron, ΓY heavy-hole, ΓX bulk, and ΓY bulk plasmons, with the value from Fig. 3-13(b) to 3-13(e). In order to make a direct comparison of four plasmons, all the data normalizes to the $q^2 = 0.01$ Å^{-2} excitation. (b) and (c) The plasmon-dispersion maps corresponding to Fig. 3-9(a) and 3-9(b), respectively, and further extending the spectra to the zone boundary. The black dots represent the light-electron and heavy-hole plasmon peaks with the error bars, standard errors in fitting. (d) and (e) The bulk-plasmon dispersion maps along ΓX and ΓY, respectively.

doi:10.6342/NTU202404787

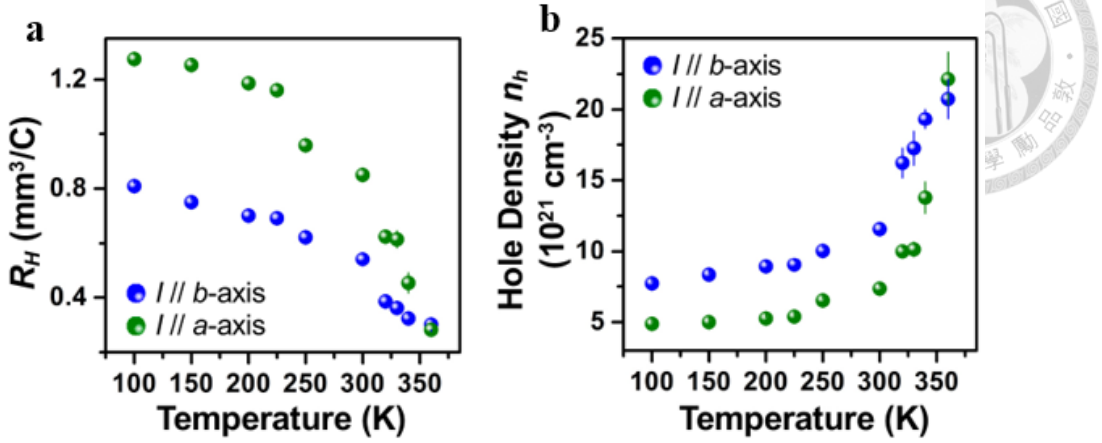

Figure 3-14 Hall measurement of CuTe. (a) Hall coefficient measured with the current flowing along a- and b-axes, respectively. The positive sign represents the predominant hole contribution. (b) The estimated carrier hole density along a- and b-axes.

Our experimental condition for acquiring EELS spectra along ΓX and ΓY has the momentum resolution around 0.09 $Å^{-1}$, with the camera length 4 m. In this momentum resolution, we can obtain every 0.1 $Å^{-1}$ step without overlapping each other. In the Fig. 3-13(b), the black dots represent the Te-p_x light-electron plasmon peak position from q = 0.1 $Å^{-1}$ to q = 0.4 $Å^{-1}$, where the light-electron plasmon peak vanished and decays electron-hole pairs because of Landau damping, the same phenomenal taking place at Fig. 3-13(c) while the range from q = 0.1 $Å^{-1}$ to q = 0.5 $Å^{-1}$. We can notice that the color map is almost dark at the region where the energy is between 0 to 1 eV in Fig. 3-13(b) and 3-13(c). The reason is because the tail of zero loss peak (ZLP) of the EELS spectra causes the complexity to light-electron and heavy-hole plasmons peak shape and intensity. By using the functions inside the DigitalMicrograph, we first measured a ZLP at empty space as a pre-measured ZLP, then we can extract the ZLP out in each EELS spectra on every q point. The method we used to extract ZLP is called “Fit Pre-measured Zero-loss” in Digital Micrograph. “Fit Pre-measured Zero-loss” is the method we used to remove the

doi:10.6342/NTU202404787

ZLP from the EELS spectra. This routine fits a user specified zero-loss spectrum to the zero-loss peak of the selected spectrum. The method is relatively simplistic and robust. It first needs to specify a reference zero-loss peak, which we acquire in the same condition as we obtain the EELS spectra. The reference zero-loss peak needs to be a single spectrum only containing the zero-loss peak and needs to have the same dispersion as the target low-loss spectra. Then, the reference zero-loss peak is aligned with the target low-loss spectra using sub-channel interpolation. After alignment, we need to specify the fitting range above the zero loss maximum for ZLP tail fitting, which we choose the energy starting from the full-width at half-maximum (usually 0.3 eV), and finishing at the energy of one in a thousand of the maximum intensity of the reference zero-loss peak. After determining the fitting range, the target low-loss spectra is separated in to two parts, the fitted zero-loss peak and inelastic spectrum. The inelastic spectrum will be the EELS spectrum with removal of ZLP.Therefore, the intensity in the region where energy below 1eV is almost near to zero. Extracting ZLP plays an important role on the next step of fitting the Te-p_x light-electron and Te-p_y heavy-hole plasmons peak position.

Fig. 3-15 shows the experimental EELS spectra of Te-p_x light-electron and Te-p_y heavy-hole plasmons of q = 0 and 0.1 $Å^{-1}$ at 300K. At q = 0 $Å^{-1}$ point, the intense quasi-elastic tail due to dynamic nature of electron scattering and also the finite momentum resolution of our apparatus, which is approximate 0.09 $Å^{-1}$, buries the Te-p_x light-electron and Te-p_y heavy-hole plasmons peaks that are essentially an order of magnitude weaker than bulk valence plasmon dispersion from ~ 17 eV[121-122,133-134]. Upon the off-q setup, such as at q = 0.1 $Å^{-1}$ where still preserve the same momentum resolution as q = 0 $Å^{-1}$, the dynamical nature of electron scattering will be broken. Therefore, the intense tails of ZLP can be significantly reduced and the Te-p_x light-electron and Te-p_y heavy-hole plasmons peaks can be observable. The persistent ZLP at q = 0.1 $Å^{-1}$ and also at larger q's is assisted by

doi:10.6342/NTU202404787

the electron-phonon scattering, which maintains throughout the entire Brillouin zone.

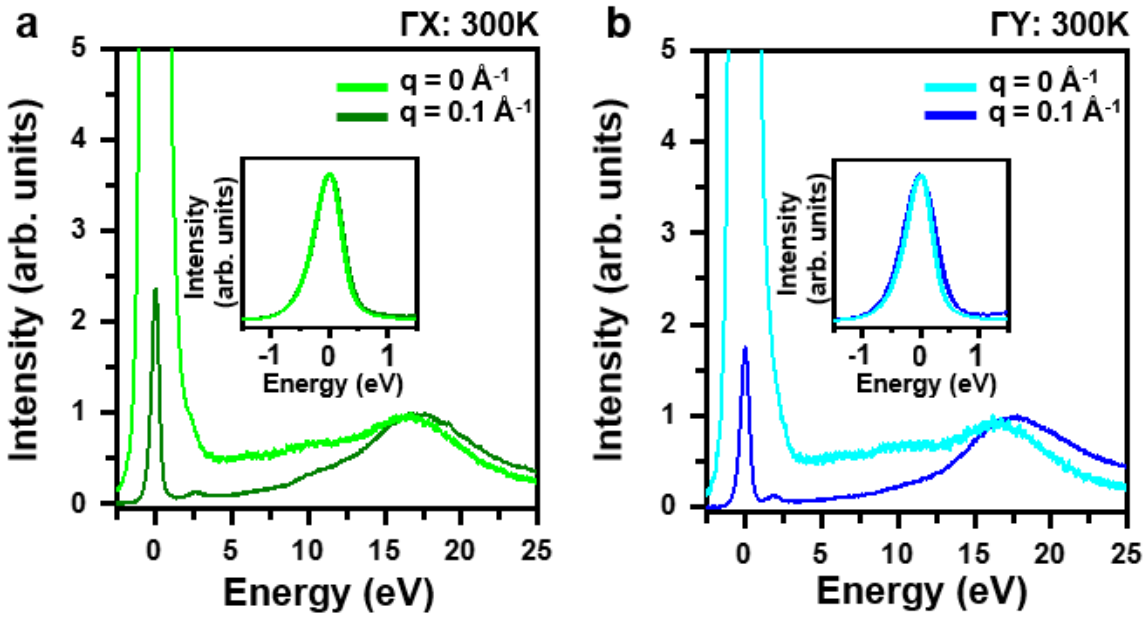

Figure 3-15 The ΓX light-electron and ΓY heavy-hole plasmons at q = 0 and 0.1 $Å^{-1}$ at 300K. (a) and (b) are the EELS spectrum along ΓX and ΓY, respectively. We compare two spectrum at q = 0 and 0.1 $Å^{-1}$ and normalize at valence bulk plasmons intensity. We find out that the dynamical inelastic electron scattering at q = 0 $Å^{-1}$ causes the ZLP tails burying the Te-p_x light-electron and Te-p_y heavy-hole plasmons peaks in the 0 to 5 eV range, and make those plasmons peaks unresolvable. The inset in (a) and (b) shows the resolution of ZLP almost the same at q = 0 and 0.1 $Å^{-1}$ even with the longer acquisition time at q = 0.1 $Å^{-1}$ due to the weaker plasmon excitation.

doi:10.6342/NTU202404787

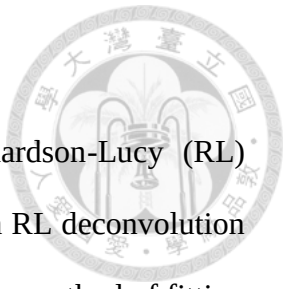

Another common used method of removing ZLP is the Richardson-Lucy (RL) deconvolution[134-136]. In Fig. 3-16, we show the comparison between RL deconvolution and the pre-measured ZLP removal method. The ZLP removal buy the method of fitting pre-measured ZLP for the respective Te-p_x light-electron and Te-p_y heavy-hole plasmons peak at q = 0.1 $Å^{-1}$ is shown in Fig. 3-16(a) and 3-16(c). Both the minimal overlap for the ZLP tail with the Te-p_x light-electron and Te-p_y heavy-hole plasmons peaks (insets) and the robustness of the plasmon-peak positions to the ZLP removal can be observed. The plasmon peaks maintain at the same position after ZLP removal. The comparison of RL deconvoluted and the original spectra of the respective Te-p_x light-electron and Te-p_y heavy-hole plasmons at q = 0.1 $Å^{-1}$, with the spectral-intensity normalizations to the bulk-plasmon excitations, are shown in Fig. 3-16(b) and 3-16(d). The deconvoluted spectra are shifted downwards for the clarity of presentations. The RL deconvolutions have been conducted in DigitalMicrograph. In Fig. 3-16(b) and 3-16(d), we can find out that the RL deconvolutions are able to improve the energy resolution of ZLP from ~0.54 eV to ~0.45 eV and sharpen the Te-p_x light-electron and Te-p_y heavy-hole plasmons peaks, however, the respective plasmons peaks remain at the same position (see the inset in Fig. 3-16(b) and 3-16(d)). Nonetheless, the wavy spectral-ripple artifacts (arrows shown in Fig. 3-16(b) and 3-16(d)) degrade the overall quality of the RL deconvolutions and RL method is not adopted in this experimental.

doi:10.6342/NTU202404787

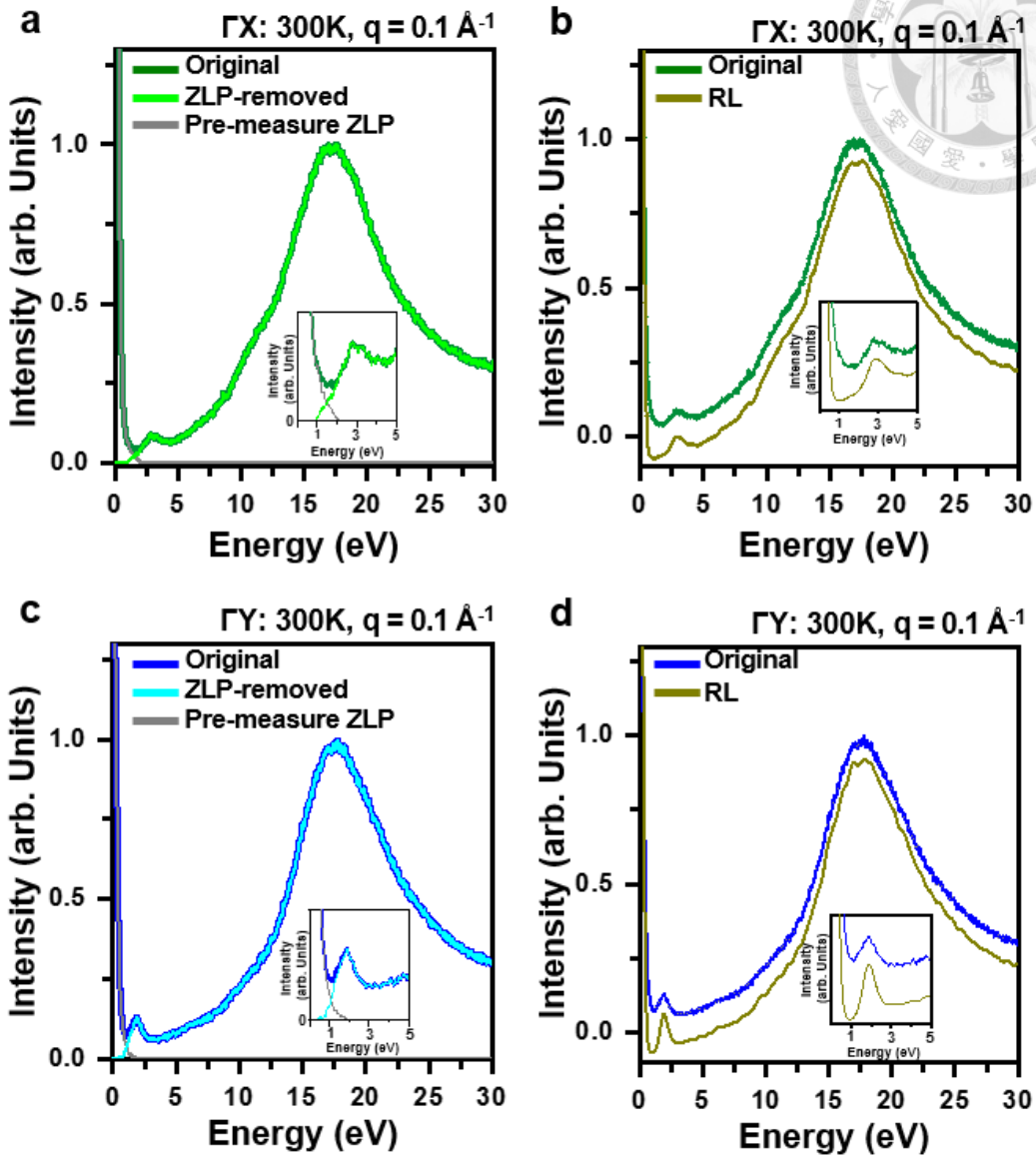

Figure 3-16 The comparison of pre-measured ZLP method and the RL deconvolution of removal ZLP of Te-p_x light-electron and Te-p_y heavy-hole plasmons at q = 0.1 $Å^{-1}$ at 300 K. (a) and (b) show the pre-measured ZLP removal and the RL deconvolution of Te-p_x light-electron plasmon, respectively. (c) and (d) show the pre-measured ZLP removal and the RL deconvolution of Te-p_y heavy-hole plasmon, respectively. The insets are the enlarged version of the respective plasmons peak positions.

doi:10.6342/NTU202404787

We use pseudo-Voight function to fit the plasmon peak position and the full width at half maximum (FWHM) for light-electron and heavy-hole plasmons. The peak positions are the black dots in the Fig. 3-13(b) and 3-13(c), and the FWHM versus q relation for light-electron and heavy-hole plasmons are in the Fig. 3-17(a) and 3-17(b), respectively.

Pseudo-Voight function is an approximation for the Voight function, which is a convolution of Gaussian and Lorentz function. It is often used as a peak profile fitting where neither a pure Gaussian nor a pore Lorentz function can appropriately describe a peak. Instead of convoluting two functions, which is Voight function, the pseudo-Voight function is defined as the sum of a Gaussian peak (G(x)) and a Lorentz peak (L(x)), weighted by a certain parameter η which shifts the profile more towards to pure Gaussian peak or pure Lorentz peak when the parameter equals to 1 or 0, respectively. The pseudo-Voight function can be written as:

$$pV(x) = \eta G(x) + (1-\eta)L(x) \tag{3.8}$$

Both Gaussian and Lorentz function share three parameters: intensity (the intensity of the peak at the maximum), peak center (position of the maximum) and FWHM of the peak. Fig. 3-17 shows the pseudo-Voight function fitting results of light-electron and heavy-hole plasmons at CDW-state of CuTe at 300K.

In Fig. 3-17, no matter the light-electron plasmon or the heavy-hole plasmon peak are fitted with three pseudo-Voight peaks denoting as red, cyan, and blue color at the 1 to 9 eV range. The red pseudo-Voight peak is to fit the light-electron and heavy-hole plasmons in Fig. 3-17(a) and 3-17(b), respectively. White triangles locate the peak positions of light-electron and heavy-hole plasmons at 300K. The gray curves are the experimental EELS spectra with q = 0.1 $Å^{-1}$ to q = 0.4 $Å^{-1}$ and q = 0.1 $Å^{-1}$ to q = 0.5 $Å^{-1}$ for light-electron and heavy-hole plasmons, respectively. The black curves are the fitted spectra of three pseudo-Voight peaks. The cyan and blue curves are the high-energy interband transition

doi:10.6342/NTU202404787

above the respective plasmons.

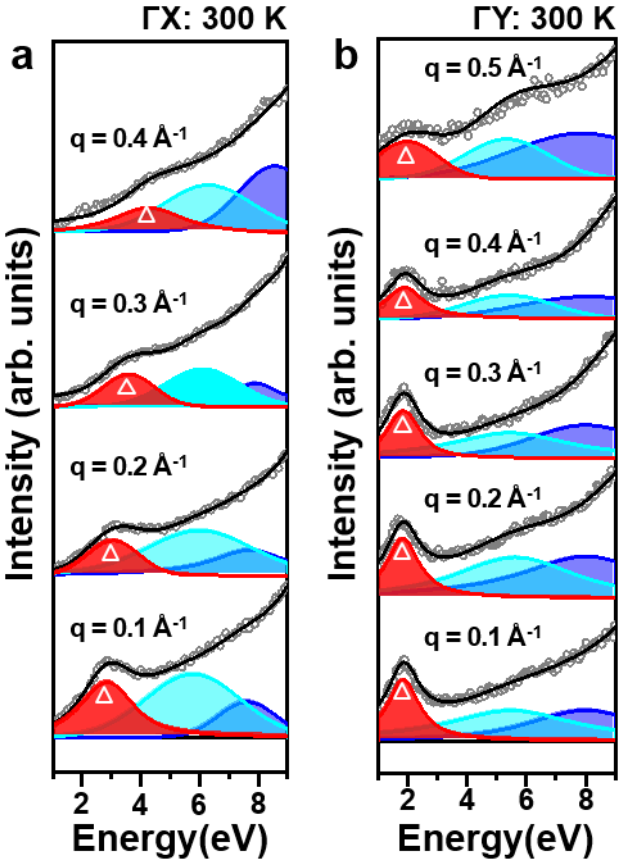

Figure 3-17 The pseudo-Voigt fitting plasmon peaks in CuTe. (a) The fitted Te-p_x light-electron and (b) Te-p_y heavy-hole plasmons of CuTe at 300 K as a function of q.

Using the equation (3.4) and the v_F in Table 3-2, we can calculate the dispersions of Te-p_x light-electron and Te-p_y heavy-hole plasmons which are the black curves in Fig. 3-13(b) and 3-13(c), respectively. In other hands, the black dots in the Fig. 3-13(b) and 3-13(c) are originated from the pseudo-Voigt peak fitting from the Fig. 3-17(a) and 3-17(b). We find a remarkable consistency in these two results. The white curve in Fig. 3-13(b) and 3-13(c) is the respective single-particle continua; $\frac{\hbar^2(q^2+2qq_c)}{2m^*}$ with the critical wave

doi:10.6342/NTU202404787

vector q_c[69,113].

$$q_c = \frac{\omega_p}{v_F} \quad (3.9)$$

The critical wave vector q_c is listed in the Table 3-2 for Te-p_x light-electron and Te-p_y heavy-hole plasmons. Beyond the single-particle crossovers at 0.29 Å^{-1} in Fig. 3-13(b) and 0.52 Å^{-1} in Fig 3-13(c), the respective Te-p_x light-electron and Te-p_y heavy-hole plasmons are to be subject to the Landau damping and decay into electron-hole pairs[63,113-114]. With the momentum exceeding the critical wave vector q_c, the plasmons gain sufficient momentum and thus decay into electron-hole pair. Once the plasmons decay into electron-hole pair, the Te-p_x light-electron and Te-p_y heavy-hole plasmons peak will become broaden and damped due to less plasmons existed. In the momentum resolved EELS experiment, we observe that Te-p_x light-electron plasmons are appreciably broadened and weakened when $q > 0.3$ Å^{-1} as shown in Fig. 3-13(b) and 3-17(a), and also for the Te-p_y heavy-hole plasmons when $q = 0.5$ Å^{-1}, shown in Fig. 3-13(c) and 3-17(b). The derived $k_F \sim 0.39$ Å^{-1} of the Te-p_x light-electron plasmons corresponds to $2k_F = q_N \sim 0.78$ Å^{-1}, matching $q_N \sim 0.8$ Å^{-1} in Fig. 3-7(e)[96]. All these fundamental agreements highlights the consistence in our plasmon-dispersion methodology for effective mass and fermi velocity.

Fig. 3-18 shows the full width at half maximum (FWHM) and fitted peak-intensity maxima of Te-p_x light-electron and Te-p_y heavy-hole plasmons at 300K. The observed plasmons broadening in Fig. 3-18(a) and 3-18(b) is consistent with the respective Landau damping illustrated in Fig. 3-13(b) and 3-13(c). The concomitant plasmon weakening is also consistent with classical physics for damped collective plasmon excitation.

doi:10.6342/NTU202404787

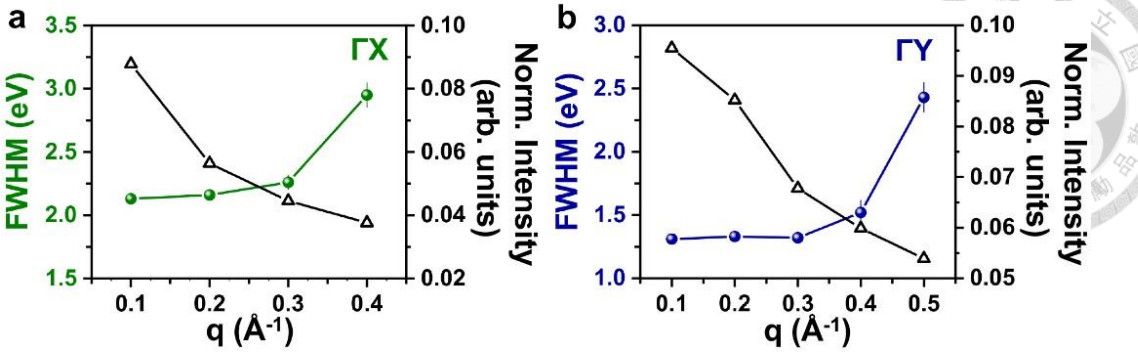

Figure 3-18 The full width and half maximum (FWHM) and fitted peak-intensity maxima of the plasmons at 300 K along ΓX and ΓY. (a) The fitted FWHM linewidths (green) of the Te-p_x light-electron plasmons shown in Fig. 3-13(b) (300 K; black dots) as a function of q and derived from the pseudo-Voigt peak fitting from Fig. 3-17(a). The intensity of plasmon peak (black) is normalized to the valence bulk-plasmon intensity which is acquired in the same time at q = 0.1 $Å^{-1}$, and obtained from the Fig. 3-17(a) as well. (b) The fitted FWHM linewidths (blue) of the Te-p_y heavy-hole plasmons shown in Fig. 3-13(c) (300 K; black dots) and the normalized peak-intensity maxima (black) obtained from the Fig. 3-17(b) as a function of q. Error bars, standard errors in the associated plasmon-peak fitting by the pseudo-Voigt method.

doi:10.6342/NTU202404787

3.4 Conclusion

In summary, we introduce the crystal structure and electronic structure of CuTe with the interesting practically linearly dispersing band in CDW state. CuTe shows the lattice distortion with periodic modulation in HAADF image with calculating the atom displacement by Atomap. CuTe also owns the gap-opening phenomenon at the practically linearly dispersing band along ΓX direction. The Fermi surface nesting and Kohn anomaly are shown in the CuTe CDW state as well, which give us the thorough evidence of CDW formation.

In addition, we use q-EELS experiment to probe the Te-p_x light-electron and Te-p_y heavy-hole plasmons along ΓX and ΓY direction, respectively. By using the classical 3D plasmon dispersion equation, we can obtain the effective mass and Fermi velocity of Te-p_x light-electron and Te-p_y heavy-hole plasmons. With the aid of pseudo-Voigt fitting on the EELS spectra, we can define the peak position of plasmon and the result from experiment and theoretical calculation have great accordance. The effective mass of Te-p_x light-electron with only 0.28 m_0 has large difference with that of Te-p_y heavy-hole, which demonstrate the anisotropic property of CuTe.

doi:10.6342/NTU202404787

Chapter 4 The Temperature Dependent q-EELS Measurement and STEM-EELS Chemical Analysis on CuTe

4.1 introduction

The study of CDW systems at different temperature is critical for unraveling the intricate interplay between electronic, lattice, and quantum effects that govern their behavior. Temperature acts a crucial parameter influencing the stability of the CDW phase, the nature of phase transitions, and the coupling between competing electronic orders. Cooling a CDW system to cryogenic temperatures reveals detailed insights into its intrinsic properties by suppressing thermal fluctuations and emphasizing quantum phenomena. Therefore, we conduct the temperature dependent q-EELS measurement of CuTe to observe the effective mass and Fermi velocity change.

Generally, the formation of a CDW state typically occurs via a phase transition at a critical temperature, T_{CDW}, which is 335 K in CuTe system. At $T > T_{CDW}$, thermal fluctuations destabilize the periodic order of the charge density. When $T < T_{CDW}$, the suppression of thermal energy enhances the influence of quantum fluctuations. These fluctuations are particularly relevant in quasi-one-dimensional and two-dimensional materials where the reduced dimensionality amplifies correlation effects. Low temperature plays a crucial role in suppressing thermal fluctuation, which otherwise disrupt the uniformity of the charge modulation and lattice distortion. In addition to the thermal fluctuations, temperature also influences the gap-opening phenomenon. Below T_{CDW}, the gap increases in magnitude as the system cools, following a mean-field-like behavior for weak-coupled system. The CDW order, which is the opening gap size, will follow the BCS theory for the weak-coupling electron correlation CDW system[53,62].

doi:10.6342/NTU202404787

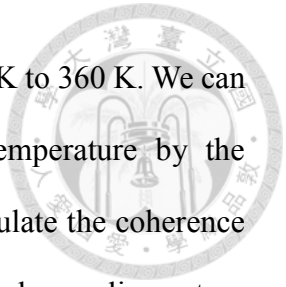

In this chapter, we use q-EELS probing the CuTe crystal from 100 K to 360 K. We can obtain the effective mass and the Fermi velocity at different temperature by the calculation illustrated at previous chapter. Furthermore, we also calculate the coherence of CuTe to observe how the CDW changes with order growth. The weak-coupling nature and weak charge localizations of CuTe make the gap-opening phenomenon follows the BCS theory. In addition, we also use STEM-EELS analysis to help us detect the charge distribution due to CDW presence. At last, we propose the possible mechanisms of the phenomena about the decreased effective mass and the enhanced Fermi velocity, which is contrast to the general CDW systems.

doi:10.6342/NTU202404787

4.2 Experimental procedure

The growth of CuTe is the same as illustrated at the section 3.2.1. The temperature dependent q-EELS measurement is conducted at 100 K, 150 K, 200 K, 250 K, 300 K, 335K, and 360 K. The temperature range includes the low temperature limit of our apparatus and the temperature above the transition temperature, T_{CDW}. At each temperature, we acquired EELS spectra along ΓX and ΓY with step 0.1 $Å^{-1}$ and summarized with nine individual spectrum.

The atomically resolved STEM-EELS experiment was conducted on an aberration-corrected JEOL-2100F microscope. The thickness along the incident probe direction is approximate 60 nm. An EELS collection angle of around 30 mrad and a probe convergent angle around 20 mrad were exploited with the probe current ~ 120 pA. All results were subject to principal component analysis (PCA) for removing the spectral random noise.

doi:10.6342/NTU202404787

4.3 Results and Discussion

4.3.1 Reduced Effective Mass (m*) and Enhanced Fermi Velocity (v_F) of the Te-p_x Light-Electrons below T_{CDW} and the BCS Weak Coupling CDW.

Fig. 4-1 shows the temperature-dependent plasmon dispersion of Te-p_x light-electron and Te-p_y heavy-hole plasmons. All the spectra are with ZLP removal in order to observe the plasmon peak clearly. The temperature-dependent plasmon dispersion have the temperature step with 50 K below the T_{CDW}, which is 335 K, and the temperature above T_{CDW} at 360 K, which is the limitation of the experimental instrument.

doi:10.6342/NTU202404787

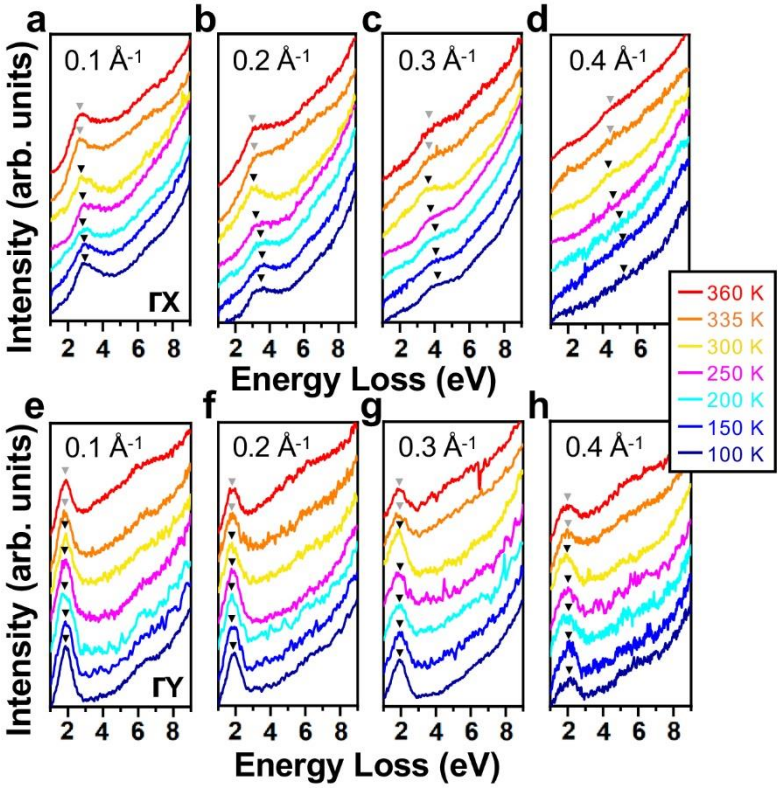

Figure 4-1 Plasmon dispersions across the CDW transition temperature at 335 K of Te-p_x light-electron and Te-p_y heavy-hole plasmons. (a)-(d) q-EELS spectra of the Te-p_x light-electron plasmons at q = 0.1, 0.2, 0.3, and 0.4 $Å^{-1}$ along ΓX as a function of temperatures at 100, 150, 200, 250, 300, 335, and 360 K. (e)-(h) q-EELS spectra of the Te-p_y heavy-hole plasmons at q = 0.1, 0.2, 0.3, and 0.4 $Å^{-1}$ along ΓY at the same temperature as ΓX direction. All spectra are with ZLP removal. The black and gray inversed triangles are the peak positions used by pseudo-Voigt fitted method. The error bars are neglected for clarity of the presentation.

doi:10.6342/NTU202404787

Below T_{CDW} (335 K), the Te-p_x light-electron plasmons at q = 0.1~0.3 $Å^{-1}$ demonstrates a obvious blueshift with decreasing temperatures (Fig. 4-1(a) to 4-1(c)). For example, the peak position of Te-p_x light-electron plasmon at 300 K is around 2.85 eV, and the peak position at 100K shifts to 3.06 eV. At q = 0.4 $Å^{-1}$ (Fig. 4-1(d)), the onset of Landau damping as descripted at the previous section damps the Te-p_x light-electron plasmon into broad, weak excitations, which are still well discernible from the spectral backgrounds and is enable to use the pseudo-Voigt fittings, as shown in the Fig. 4-2.

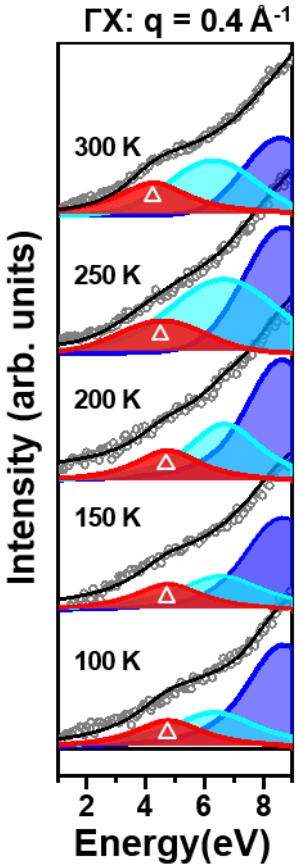

Figure 4-2 The pseudo-Voigt fitting of plasmon peaks of Te-p_x light-electron plasmon at q = 0.4 $Å^{-1}$ with different temperatures. The method is the same in the Fig. 3-17. The white triangle instructs the peak positions of the Te-p_x light-electron plasmon of different temperatures below T_{CDW}. The cyan and blue fitted peaks are the two high-energy interband transitions from the calculated dielectric functions. The black curves are the fitted spectra and the gray open dots are the experimental spectra. No constraint on the linewidth or positions of all the three spectral features (red, cyan, and blue) has been applied during the fitting.

doi:10.6342/NTU202404787

The readily fitted plasmon-peak positions (inversed black triangles, Fig. 4-1(d) and Fig. 4-2) also unveil a blueshift below T_{CDW}. In contrast, the Te-p_y heavy-hole plasmon is robust against temperatures, as the inverse triangles shown in Fig. 4-1(e) to 4-1(h). From the Fig. 3-7(b) to 3-7(e), we have known that the Te-p_y heavy-holes are irrelevant with the CDW modulation. The Te-p_x light-electrons along ΓX determine the CDW order and such a plasmon blueshift related to decreasing temperature in CDWs had not been thoroughly understood.

Fig. 4-3(a) exhibits the $\omega^2 - q^2$ scaling of the Te-p_x light-electrons plasmons dispersions across T_{CDW} in Fig. 4-1(a) to 4-1(d). In the Fig. 4-3(a), the blueshift of the Te-p_x light-electron plasmon with decreasing temperature and the plasmon dispersion above T_{CDW} are both shown clearly. The normalization to the respective excitations at $q^2 = 0.01$ $Å^{-2}$ facilitates a direct comparison across different temperatures. The blueshift phenomenon only appears at the temperatures below T_{CDW}. However, at the range above T_{CDW}, the plasmon-dispersion relations are not blueshift, neither redshift.

In Fig. 4-4, the blueshifts of the Te-p_x light-electrons plasmon with decreasing temperatures have been derived from the loss function using the DL modeling of equation (3.2) with increasing ω_Δ, and meanwhile, γ_Δ being kept constant for simplicity. The reason why using DL model to simulate the loss function is because it may be argued that the CDW-gap opening (Fig. 4-3(c)) can add on a single-particle transition to $\varepsilon(\omega)$ and pushes the Te-p_x light-electron plasmons to a higher energy, resulting in the blueshifts with decreasing temperatures in Fig. 4-3(d).

In Fig. 4-4, the calculated plasmon blueshifts with the gap Δ play the role as a tunable additional oscillator strength in equation (3.2). With different gap size, the related loss function calculated from DL model exhibits different degree of blueshifts comparing to the non-CDW state. When the gap size is above 0.7 eV, the corresponding induced

doi:10.6342/NTU202404787

blueshift in above 0.1 eV. However, from the Fig. 4-3(c), the gap size is no more than 0.2 eV that indicates that the blueshifts of the Te-p_x light-electron plasmons do not result from the gap-size opening effect.

Reminding the equation (3.4), the slope of $\omega^2 - q^2$ gives the important clue of v_F and we can also obtain the carrier density and effective mass as well. In order to calculate those important factors, we also need to recall the equation (3.3), and obtain the ε_∞ at different temperatures. Fig. 4-5 shows the calculated ε_∞ and $\omega_P^{q\to 0}$ at different temperature. We can recall the number of the respective Drude component,ω_p, which is 3.25 and 3.15 eV in the normal and CDW states in Table 3-1, respectively. Originally, we should fit the RPA calculated dielectric function and obtain the ε_∞ at each temperature. However, it is almost implausible to have the RPA dielectric function at each designated temperature. Hence, we use the Drude component 3.25 eV for the temperature above T_{CDW}, and the number of 3.15 eV for temperature below T_{CDW}, which are from 300K to 100K. Then, the number of $\omega_P^{q\to 0}$ can be obtained from the Fig. 4-3(a). The complete temperature-dependent result is shown in Fig. 4-5 After obtaining the ε_∞, the effective mass and carrier density are then resolved following the equation (3.4).

Fig. 4-3(b) shows the readily resolved effective mass and carrier density and, more noticeably, their remarkable agreements with an inverse BCS-related temperature dependence of the weak-coupling order below T_{CDW}. The BCS-related temperature dependence curve of the weak-coupling order comes from the formula (4.1)[62].

$$\frac{\Delta(T)}{\Delta(0)} \cong 1.74\left(1-\frac{T}{T_c}\right)^{0.5} \tag{4.1}$$

$\Delta(T)$represents the energy gap at the temperature T which is also the order parameter of CDW, and T_c is the transition temperature.

Nevertheless, there is a marginally small increase of effective mass across the T_{CDW},

doi:10.6342/NTU202404787

which is 0.28 m_0 at 300K and is 0.27 m_0 at 335K. Therefore, there is a tendency change across T_{CDW}, and the agreements with BCS-related temperature dependence of the weak-coupling order is violated when temperature is above T_{CDW}.

Fig. 4-3(c) indicates, below T_{CDW}, both the CDW order parameter Δ and q_{CDW} intensity at [0.4a*, 1b*, 0.5c*] evolve in accordance with the BCS scaling, shown in Fig. 4-3(c) and the weak-coupling CDW essence of $\Delta << E_F \sim 2.07$ eV (Table 3-2) is satisfied[53,62,137]. The CDW order parameter Δ is reproduced from the Ref. 103 and the q_{CDW}-superlattice intensity is normalized to the neighboring Bragg spots across T_{CDW}. The reason used the q_{CDW} at [0.4a*, 1b*, 0.5c*] instead of [0.4a*, 0b*, 0.5c*] is because the intensity of the (000) Bragg spot is too high to influence the q_{CDW} spots. The inset of Fig. 4-3(c) shows the robust commensurability of the CDW superlattice down to 100 K measured from the Fig. 3-7(a).

The CDW is steadily a weak-coupling Peierls instability (followed the weak-coupling CDW essence which the $\Delta << E_F$) within the BCS context[53,137], and impacts the plasmon dispersion (Fig. 4-1(a) to 4-1(d)) by decreasing effective mass and carrier density below T_{CDW} at the growth of the CDW order-parameter strength, which Δ is increasing following the BCS weak coupling curve at Fig. 4-3(c), instead of the notion of enhanced effective mass and reduced v_F upon increasing electronic correlations[112,138-139].

Fig. 4-3(d) exhibits the momentum- and temperature-dependent plasmon blueshsifts, which are derived from the pseudo-Voigt fitting of Te-p_x light-electron plasmon peak position of Fig. 4-1(a) to 4-1(c) with reference to the 300 K excitations with various q's. The solid dots represent the results from the experimental spectra. The theoretical counterparts, shown as open dots, are calculated by the equation (3.4) using the enhanced v_F below T_{CDW} toward 100K in Fig. 4-4(a).

doi:10.6342/NTU202404787

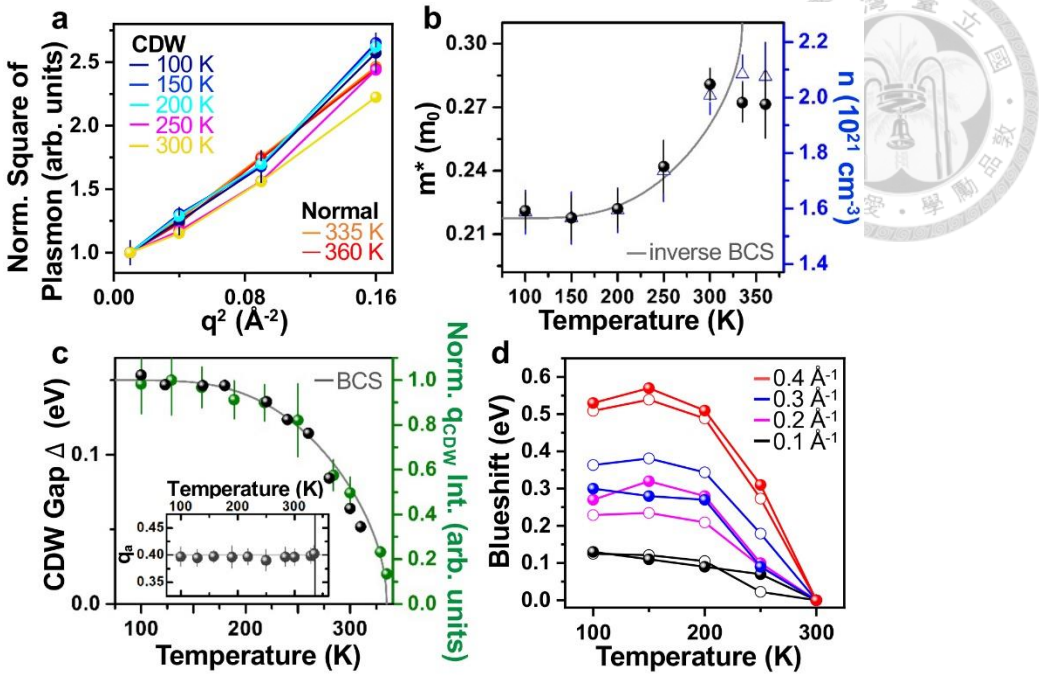

Figure 4-3 Deriving effective mass and carrier density of the CDW-related Te-p_x light-electrons and the BCS context of the weak-coupling CDW. (a) The $\omega^2 - q^2$ scaling of the dispersion of Te-p_x light-electron plasmons in Fig. 4-1(a) to 4-1(d). Error bars are the standard errors in the fitted plasmon peak and only shown for 100 K's for clarity of the presentation. (b) The resolved effective mass and carrier density of the light electrons from the linearly fitted slopes in (a). The gray curves is the inversed BCS-temperature dependence. Error bars are the standard errors upon the linear fitting. (c) Evolutions of the CDW-gap size (reproduced from the Ref. 119) and the q_{CDW}-superlattice intensity, which is normalized to the neighboring Bragg's spots, across the T_{CDW}. The inset figure shows the robust commensurability of the CDW superlattice from room temperature to 100 K. The gray curve is the BCS-temperature dependence curve. Error bars in the normalized q_{CDW}-superlattice intensity (green) and the commensurability (inset) are the standard deviation on the averaging over five diffraction patterns. (d) The temperature-dependent plasmon blueshifts at each q respect to the excitations at 300 K. The solid dots are the experimental results fitted from the Fig. 4-1(a) to 4-1(d), and the open dots are derived from the equation (3.4) as the theoretical counterparts.

doi:10.6342/NTU202404787

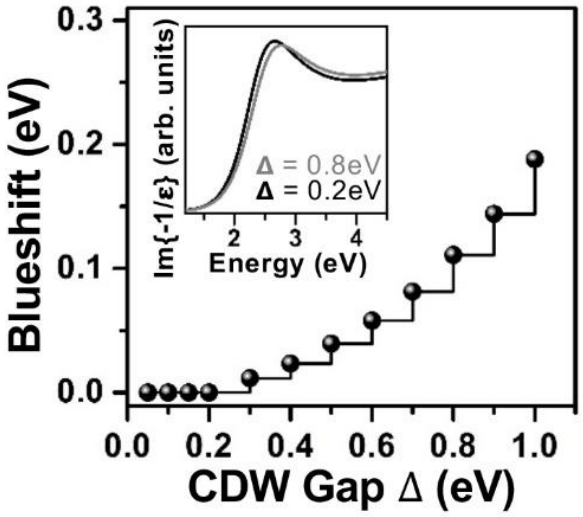

Figure 4-4 The DL modeling of plasmon blueshifts with different CDW gap opening. The calculated plasmon blueshift due to the CDW gap opening below T_{CDW}, which may produce an extra single-particle oscillator strength. The calculated blueshifts are defined as the difference from the plasmon-peak position with gap size of 50 meV, which is the gap size at room temperature in Fig. 4-3(c). The inset figure is the calculated EELS loss function from the DL modeling with gap size of 0.2 and 0.8 eV, respectively. In the DL modeling (from the equation (3.2)), the gap size needs to achieve more than 0.7 eV in order to cause a 0.1 eV blueshift in EELS loss function, which is way beyond the experimental observation in Fig. 4-3(c). The gap size only reaches to 0.15 eV at 100 K and the corresponding blueshift causing from the single-particle oscillator is almost 0 eV. In other hand, the blueshifts of the Te-p_x light-electron plasmon are all larger than 0.1 eV at every q. Therefore, the characteristically small gap-size opening of CuTe can barely affect the Te-p_x light-electron plasmon that sits at a much higher energy than the gap size.

doi:10.6342/NTU202404787

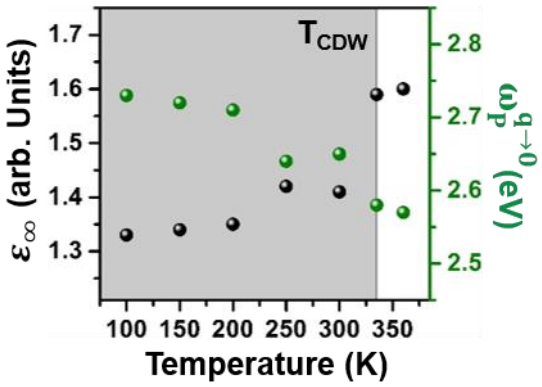

Figure 4-5 The temperature-dependent ε_∞ and $\omega_P^{q\to 0}$ across TCDW of CuTe. The ε_∞ (black) and the corresponding $\omega_P^{q\to 0}$ (green) are used in the effective mass and carrier density derivations in Fig. 4-3(b).

The DL simulations of the plasmon-dispersion maps of CDW-state and normal-state of CuTe are shown in Fig. 4-6(a) and 4-6(b), respectively. In Fig. 4-6(a) and 4-6(b), the dispersion maps of the Te-p_x light-electron plasmon are calculated using DL model from the equation (3.2) and Table 3-1, with the q dependence in the $\varepsilon(\omega)$ being approximated by a q dependence in the Drude term in accordance with equation (3.4). The gapping term in the equation (3.2) is obtained from the Fig. 4-3(c). For simplicity, the fourth term in the equation (3.2) has been assumed to be q-independent. The calculated maps show a great consistency with the superimposed experimental dispersions, with the incorporation of respective single-particle continua.

doi:10.6342/NTU202404787

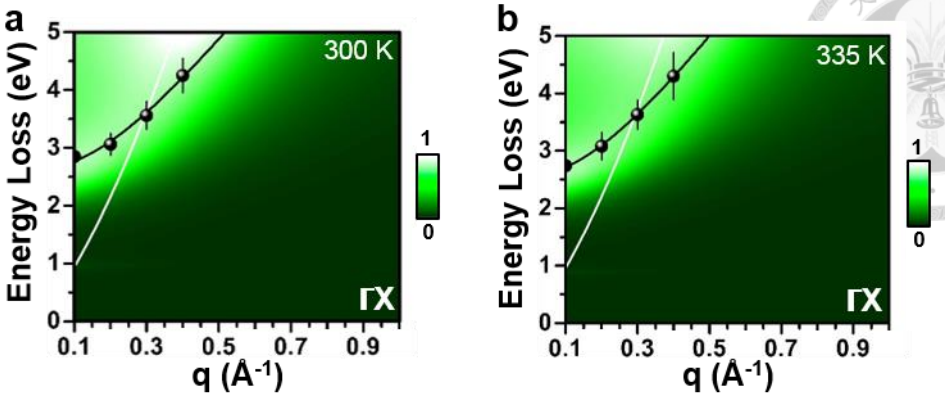

Figure 4-6 The DL simulations of the plasmon-dispersion maps at (a) CDW-state and (b) normal-state of respective Te-p_x light-electron plasmon. The black dots are the pseudo-Voigt fitted plasmon peak positions. The white curves are the respective single-particle continua. Error bars are the standard errors in the plasmon-peak fitting.

The consistency in the experimental and theoretical results (Fig. 4-1(d) and Fig. 4-6) confirms the central finding of our work, which indicates that the weak-coupling CDW of CuTe reduces effective mass and enhances the fermi velocity of the Te-p_x light-electrons below T_{CDW} by ~20%.

doi:10.6342/NTU202404787

4.3.2 The weak, frozen CDW potential below T_{CDW} and the linear-band renormalization in graphene.

The light effective mass of the CDW-related Te-p_x light-electrons, which is 0.22 m_0 at 100 K and 0.28 m_0 at room temperature, shown in Fig. 4-3(b), below T_{CDW} points out a weak correlation of the CDW order[98], which is anticipated for the weak electronic correlation inherent to linearly-dispersion bands and emphasizes the weak-coupling essence in Fig. 4-3(c)[139]. The weak-coupling nature of CuTe also features the phenomenon of the weak charge localization. Using STEM-EELS technique, we can address this charge problem and observe the charge distribution of CuTe accompanied by the CDW existence. The STEM-EELS elemental mapping of the CDW of CuTe at 300 K is shown in Fig. 4-8(b) and the core-level edges, which give hint on the charge-valence state, shown in Fig. 4-7, of the copper and tellurium atoms are exhibited in Fig. 4-8(c)[140-143]. All the Cu and Te atoms, shown in Fig. 4-8(c) and Fig. 4-7, show their respective edges compared to the edges of metallic Cu^0 and Te^0.

In Fig. 4-7, we can see the STEM-EELS spectra acquired in the CDW supercell at 300 K. In Fig. 4-7(a), the top panel is the Te M-edge EELS spectra consist of one single Te atom, all 20 Te atoms in the Fig. 4-8(c), and the metallic Te^0. The one single Te atom EELS spectrum comes from the Fig. 4-8(b) and all 20 Te atoms EELS spectrum is from the supercell. The metallic Te^0 is the reference spectrum acquired on a thin Te-metal foil. The bottom panel is the first derivative of the three Te M-edge spectra, with the onset energy of the metallic-Te^0 reference being denoted by a vertical line at around 595 eV.

The spectra in Fig. 4-7(b) is the counterparts of the Cu L-edge. We also acquired one single Cu atom, all 20 Cu atoms in CDW supercell, and the metallic Cu^0 EELS spectra in the Fig. 4-7(b) top panel. The one single atom spectrum and the all Cu atoms spectrum are obtained as the same method of Te M-edge EELS spectra. The reference-Cu^0 spectrum

doi:10.6342/NTU202404787

is taken on a thin Cu-metal foil. The bottom panel is the first derivative of three Cu L-edge EELS spectra, with the onset energy of the metallic-Cu^0 reference being denoted by a vertical line at around 930 eV.

Those six spectra have been subject to the random-noise reduction by the principle-component analysis and then using the power-law method to remove the background so that the Te M-edge and Cu L-edge peak becomes less affected. The spectra of one single Cu and Te atom are the respective integrals of 2*2 pixels underneath, which the pixel size is around 4 Å, and the spectra of all 20 Cu and Te atoms are the integrals of all the associated atoms in the 5a × 2c supercell of CDW, which is the rectangle region shown in Fig. 4-8(c).

doi:10.6342/NTU202404787

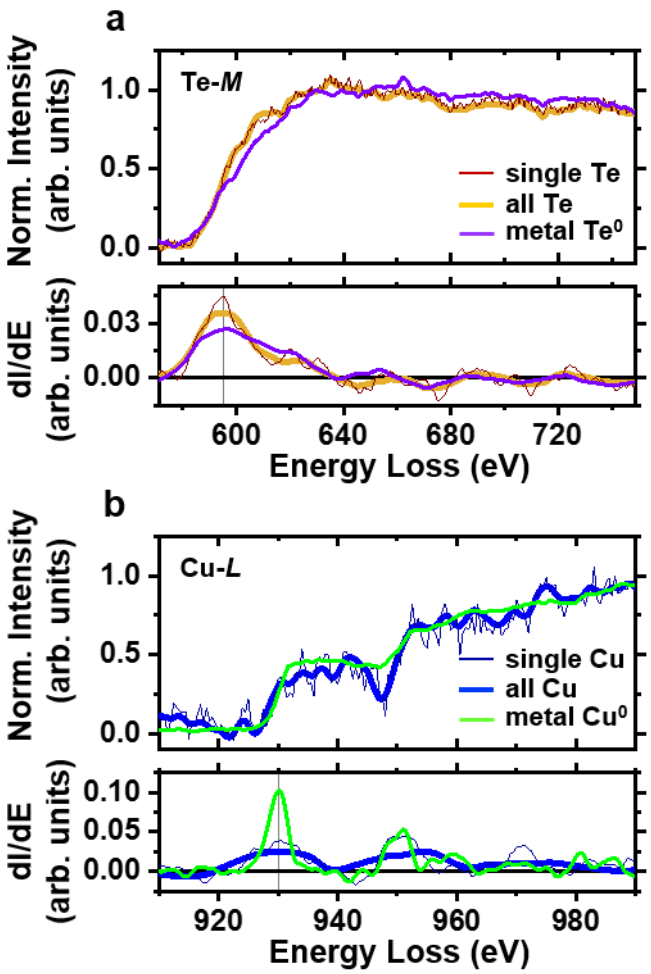

Figure 4-7 STEM-EELS spectra acquired in the CDW supercell at 300 K. (a) There are three Te M-edge EELS spectra consist of the top panel, which are the one single Te atom (thin dark red), all 20 Te atoms (thick yellow), and the reference metallic Te^0 (purple). The bottom panel consists of the first derivative of three spectra in the top panel. (b) There are three Cu L-edge EELS spectra consist of the top panel, which are the one single Cu atom (thin dark blue), all 20 Cu atoms (thick blue), and the reference metallic Cu^0 (green). The bottom panel consists of the first derivative of three spectra in the top panel.[48-50]

doi:10.6342/NTU202404787

In our STEM-EELS instrument setup, the electronic detection limitation is 0.03 e per unit cell so that the change of charge distribution can be observable[141-143]. The atom-by-atom charge variation across the CDW superlattice would then be within $Te^{\pm 0.03}$ and $Cu^{\pm 0.03}$, because we does not observe the clear enough peak variation of Te M-edge and Cu L-edge compared to the metallic EELS spectra in Fig. 4-7(a) and 4-7(b), respectively. The charge variation of CuTe CDW is appreciable smaller than the order of ±0.1 in localized, correlated charge orders[139,141]. The maximum of the general electrostatic potential of the weak-coupling CDW is approximate 0.02 eV[143], which is even smaller than our instrument detection limit.

The general electrostatic potential built across parallel charged sheets is evaluated by $V = \frac{n_{2D} ed}{\varepsilon_0 \varepsilon}$, where n_{2D} is the planar carrier concentration, e is the electron charge, and d is the distance between the parallel sheets. We use the classical formula to estimate the electrostatic potential of CDW. Considering the maximum charge variation ±0.03 in our CDW system (from Fig. 4-7 and Fig. 4-8(b) and 4-8(c)), the planar carrier concentration n_{2D} could correspond to $\frac{0.03}{bc}$, which b and c is the lattice parameter of CuTe. Assuming the sheets parallel sheets locate at the peak and valley of an individual sinusoidal CDW wave in Fig. 3-6(b), the distance of parallel sheets would be 2.5a, which a is also the parameter of CuTe. Following the planar carrier concentration just estimated, we can derive the electrostatic potential of CuTe CDW system is around 0.01 eV. Owing to the presence of the two anti-phase coupled sinusoidal CDW waves in the CuTe supercell, the characteristic electrostatic potential could increase to 2V, which is approximate 0.02 eV at maximum[144]. The potential barrier height of 0.02 eV is merely smaller than the thermal energy at room temperature, which is around 0.026 eV. The magnitude of the electrostatic potential comparing to the thermal energy provides the fluctuation near the

doi:10.6342/NTU202404787

T_{CDW} and the frozen-in CDW below 200 K, where the thermal energy is around 0.017 eV.

We address the coherence lengths of the CDW along a- (ξ_a) and c-axes (ξ_c) with decreasing temperature using the respective inverse width of the q_{CDW} at [0.4a*, 1b*, 0.5c*] along a* and c*, shown in Fig. 4-8(d). Below T_{CDW}, ξ_a remains robustly of around 55 Å, which is nearly 3.5 × 5a, on the other hand, ξ_c follows the BCS weak-coupling curve, where ξ_c is around 14 Å at room temperature and around 62 Å at 100 K. The weak-coupling CDW in CuTe is fluctuating along c-axis near the T_{CDW} and frozen into a growingly spatially coherent order at reduced temperatures. Therefore, the CDW potential becomes more coherent toward 100 K and causes a more smooth electrostatic potential background, which may reduce the electron scattering at low temperature and may have a chance to reduce the effective mass of Te-p_x light-electrons and increase the fermi velocity below T_{CDW}, as shown in Fig. 4-8(a)[115]. However, the electrostatic speculation of the reduced effective mass and enhanced fermi velocity should not be the most important factor, since the absence of the CDW potential above the T_{CDW} does not cause the even lighter effective mass, as shown in the Fig. 4-3(b), and faster fermi velocity, shown in Fig. 4-8(a). As prediction, without the fluctuation resulting from electrostatic potential of CDW above T_{CDW}, the effective mass should be lighter due to the less electron scattering and fermi velocity should be even higher than those properties at low temperature.

doi:10.6342/NTU202404787

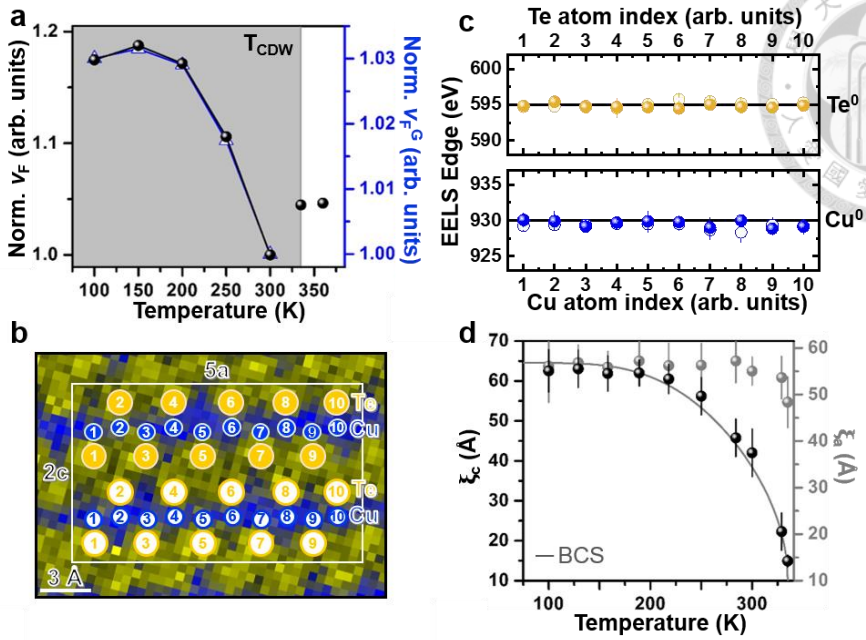

Figure 4-8 Fermi velocity of the Te-p_x light-electrons, STEM-EELS of the CDW at 300 K and the CDW coherence lengths with different temperature. (a) The calculated fermi velocity of the Te-p_x light-electrons. The Black dots are the fermi velocity calculated from the Fig. 4-3(a) using the equation (3.4) and temperature-dependent effective mass and carrier density in Fig. 4-3(b). Blue triangles are the calculated fermi velocity from equation (3.7) in the later content. For clarity, all results are normalized to the respective number at room temperature. (b) The STEM-EELS elemental mapping of the CDW superlattice, which is 5a × 2c. The yellow and blue solid dots represent the crystallographic Te and Cu atoms sites in the upper portion of the supercell, respectively. The yellow and blue open dots are the counterparts at the lower portion of the supercell. (c) STEM-EELS probing of the Cu and Te core-level edges peaks at each sites from b. Error bars are the standard error on the analyses of the first derivative of the STEM-EELS spectra. The black horizontal line shows the excitation core-level edges peaks of the metallic Te^0 and Cu^0. (d) The temperature-dependent coherence lengths of the CDW along c-axis (ξc) and a-axis (ξa). Gray curve is the temperature dependent accordance with the BCS weak-coupling theory. Error bars are the standard deviation on the averaging five diffraction patterns.

doi:10.6342/NTU202404787

Because the frozen electrostatic potential background is not the most essential factor to cause the reduced effective mass and enhanced fermi velocity, we then seek for another reason to explain the phenomenon. Therefore, we put our attention on the band structure in order to obtain some hints. Indeed, the reduced carrier density across T_{CDW} by CDW gapping (shown in Fig. 4-3(b)) of the practically linearly dispersing band along ΓX reminds us of the canonically reduced effective mass and enhanced fermi velocity by decreasing carrier density in gated suspended graphene[132]. The gated suspended graphene is subject to sole inherent electronic screening, for which the lower the gating-tunable carrier density, the weaker the screening[51,132]. The weak screening would result in an enhanced electron-electron interaction, which will renormalize the conical $\hbar v_F q$ linearly dispersing band near the fermi level by enhanced fermi velocity and reduced effective mass[132]. Equation (4.2) denotes the characteristic logarithmical dependence of the fermi velocity on carrier density and is borrowed to use on the situation of the Te-p_x light-electrons in the CDW state with the fermi velocity = 1.61×10^8 cm s^{-1} (300 K, Table 3-2)[2]. The fermi velocity of CuTe is distinctly compatible with the fermi velocity of the graphene, which is 1.5×10^8 cm s^{-1}[132].

$$v_F(n) = v_F(n_0)\left[1 + \frac{e^2}{8\varepsilon_G \hbar v_F(n_0)} ln\left(\frac{n_0}{n}\right)\right] \quad (4.2)$$

, where the n_0 and $v_F(n_0)$ are used from the result of the respective carrier density and fermi velocity of CuTe at 300K, the decreasing gating-tunable n is regarded as the temperature-dependent carrier density from Fig. 4-3(b), and the effective screening constant ε_G of graphene is replaced by the temperature-dependent ε_∞ in Fig. 4-5. In Fig. 4-8(a), we show the fermi velocity v_F^G, calculated from the equation (3.7), and superimpose the fermi velocity, v_F, we calculated using equation (3.4) with temperature dependent effective mass and carrier density. Surprisingly, the normalized temperature dependences of v_F^G and v_F below T_{CDW} are almost identical. The only difference

doi:10.6342/NTU202404787

between these two calculated fermi velocities are because of the small coupling term $\frac{e^2}{\hbar v_F(n_0)}$ in equation (3.7)[132]. Thanks to the similar result from the free-suspended graphene, we may consider the reason of reduced effective mass and enhanced fermi velocity at low temperature is because the band renormalization due to stronger electron-electron interaction resulting from the weaker screening effect of less carrier density.

doi:10.6342/NTU202404787

4.4 Conclusion

The q-EELS measurement in our experiment becomes an important tool to acquire effective mass and fermi velocity of the materials. Although the increased resistivity resulting from the CDW gap-opening effect would impede the quantum oscillatory measurements of effective mass, we are aware that the brilliant low resistivity of CDW-gapped CuTe has strengthen quantum oscillations and resulted in effective mass of ~0.13, ~0.23, and ~0.35 m_0, of which the respective electronic origins are unspecified[98]. At the same time, the obstacles toward lower temperatures and higher magnetic fields make heavier carrier in CuTe invisible. In our q-EELS setup, the heavier carrier, so as the Te-p_y heavy-holes, are capable of tackling. Meanwhile, we also resolve the effective mass, nearly 0.22 m_0 of the Te-p_x light-electrons at the BCS low-temperature limit, as shown in Fig. 4-3(b). The consistency with the reported effective mass ~ 0.23 m_0 at 2 K[98], inplies that the heavier ~0.35 m_0 electrons hereby may represent survived carriers from high temperatures, and their numbers could be so small that they are below our EELS detection limitation[141-142], hence it is unobservable in Fig. 4-1(a) to 4-1(d).

Certainly, there are more and more interests in plasmon dispersion in CDW systems of plenty of quantum materials and the q-EELS technique owns the unique advantages, which can directly obtain a broad range momentum that makes this measurement unparalleled for the subject[122-128]. The q-EELS measurement has been already used to study other CDW system such as 1T-$TiSe_2$. At the 1T-$TiSe_2$ system, it has been reported the softening and condensation of the plasmon at the characteristic modulation wave vector below T_{CDW}, which is contrast to the CuTe plasmon dispersion with quadratic relation and damped, vanishing excitations toward q_a. In the recent study of 1T-$TiSe_2$, the plasmon takes place at the energy closing to the opening CDW-gap size that is largely influenced by the gapping effect below T_{CDW}[114,123]. In another case of transition-metal

doi:10.6342/NTU202404787

dicahlcognide 2H-$NbSe_2$, a negative plasmon dispersion has been observed and attributed to the electronic impact of the CDW order[124-125]. However, the negative dispersion behavior has been irrelevant to the CDW instability and may cause from a band-structure effect that the persistence of an interband transition above the plasmon and screen the plasmon excitation down to a lower energy[126-127]. In addition, q-EELS probing for the collective magnetic excitations of magnons and EELS with only meV resolution become essential considering the typical few tens or meV similar to those of phonons.[144-146] The q-EELS probing of magnons dispersions is important comparing to the neutron scattering experiment with low scattering cross sections and deserves future devotions[146].

In this chapter, we use q-EELS to help us probe CuTe CDW system in various temperature. We used the plasmon dispersion equation to calculate the effective mass and the Fermi velocity from low temperature 100 K to 360 K, which is above the T_{CDW}. We found that the effective mass and the Fermi velocity show the contrast behavior to the examples we mentioned above. The effective mass went lighter and the Fermi velocity increased with CDW order growth. We ruled out the possibility from the single-particle transition coming from the gap-opening phenomenon. The reason may lie in the band renormalization due to the less screening effect resulting from the decreasing of carrier density. The practically linearly dispersing band of CuTe showed the similar behavior as suspended graphene with tunable carrier density control. The discovery of the reduced effective mass and enhance Fermi velocity deserves more attention to the similar system with Peierls CDWs of the weak-coupling BCS relation.

doi:10.6342/NTU202404787

Chapter 5 Conclusion

There are increasing interest in q-EELS probing of the collective excitation in the complicated material system, especially with CDWs. CuTe plays an important role in our experimental to open the door of exploring the dynamic plasmon behavior company with static CDW existence. The Peierls instability of CuTe fulfills both the classical BCS notion on weak-coupling CDWs system and the quantum ingredient of gapped, practically linearly dispersing band. The growing CDW order below T_{CDW} results in the reduction of effective mass of CDW corresponding Te-p_x light-electrons and enhancement of Fermi velocity. The phenomenon is stark contrast to the enhanced effective mass and reduced Fermi velocity on other correlated electronic orders.

We consider two possible reasons of leading to the result. The first one lies in the electrostatic-potential background becoming better distributed with decreasing temperature, which may reduce the scattering of Te-p_x light-electrons and cause the reduced effective mass and enhanced Fermi velocity. Another reason may hide in the analogue to the band-renormalized graphene system. With a tunable gap on the graphene, the carrier density has changed and the reduced effective mass and enhanced Fermi velocity appear on the system as well. The band renormalization results from the more strengthened electron-electron or electron-phonon interaction due to the less screening effect causing from lower carrier density. In our CuTe system, the carrier density decreasing with lower temperature and owning the similar practically linearly dispersion band make the suspended-graphene example shed essential light on our explorations.

The CuTe experiment gives us the implications on the timely open question of effective mass and Fermi velocity of relativistic fermions in a wide spectrum of CDW-gapped

doi:10.6342/NTU202404787

topological Dirac and Weyl semimetals with emergent quantum phenomena. Moreover, a pressurized superconducting cuprate has been shown to manifest reduced effective mass[55] and the superconductivity found in pressurized CuTe may be associated with our observation[56]. Whether our discovery of the reduced effective mass and enhanced Fermi velocity below T_{CDW} is general to all 1D or quasi-1D Peierls CDWs of the weak-coupling and gap opening effect on the practically linearly dispersing band needs more extensive inspections.

doi:10.6342/NTU202404787

Reference

[1] D. Hsieh, *et al.* A topological Dirac insulator in a quantum spin Hall phase. *Nature* **452***,* 970-974 (2008).

[2] M. Z. Hasan, & C. L. Kane, Colloquium: Topological insulators. *Rev. Mod. Phys.* **82**, 3045-3067 (2010).

[3] Y. Ando. Topological Insulator Materials. *J phys. Soc.Jpn.* **82**, 102001 (2013).

[4] D. Hsieh, *et al.* A tunable topological insulator in the spin helical Dirac transport regime. *Nature* **460**, 1101-1105 (2009).

[5] Z. Fan, *et al.* Superconductivity in nickelate and cuprate superconductors with strong bilayer coupling. *Phys. Rev. B* **110**, 024514 (2024).

[6] R. X. Zhang, & S Das Darma, Intrinsic Time-Reversal-Invariant Topological Superconductivity in Thin Films of Iron-Based Superconductors. *Phys. Rev. Lett.* **126**, 137001 (2021).

[7] R. X. Zhang, W. S. Cole, & S Das Darma, Helical Hinge Majorana Modes in Iron-Based Superconductors. *Phys. Rev. Lett.* **122**, 187001 (2019).

[8] B. R. Ortiz, *et al.* CsV_3Sb_5: A Z_2 Topological Kagome Metal with a Superconducting Ground State. *Phys. Rev. Lett.* **125**, 247002 (2020).

[9] S. Li, *et al*. Magnetic-Field-Induced Quantum Phase Transitions in a van der Waals Magnet. *Phys. Rev. X* **10**, 011075 (2020).

[10] P. A. McClarty. Topological Magnons: A Review. *Annu. Rev. Condens. Matter Phys.* **13**, 171-190 (2022).

[11] N, Nagaosa, T. Morimoto, & Y. Tokura, Transport, magnetic and optical properties

doi:10.6342/NTU202404787

of Weyl materials. *Nat Rev Mater.* **5**, 621–636 (2020).

[12] S. Nie, *et al*. Magnetic Semimetals and Quantized Anomalous Hall Effect in EuB_6. *Phys. Rev. Lett.* **124**, 076403 (2020).

[13] B. Zhang, *et al*. Quantum Wave-Particle Duality in Free-Electron--Bound-Electron Interaction. *Phys. Rev. Lett.* ***126***, 244801 (2021).

[14] N. Schwaller, M. A. Dupertuis, & C. Javerzac-Galy, Evidence of the entanglement constraint on wave-particle duality using the IBM Q quantum computer. *Phys. Rev. A* ***103***, 022409 (2021).

[15] L. Li, *et al*. Symmetry-Breaking-Induced Multifunctionalities of Two-Dimensional Chromium-Based Materials for Nanoelectronics and Clean Energy Conversion. *Phys. Rev. Appl.* ***18***, 014013 (2022).

[16] L. Fu, & C. L. Kane, Topological insulators with inversion symmetry. *Phys. Rev. B* **76**, 045302 (2007).

[17] T. L. Hughes, E. Prodan, & B. A. Bernevig, Inversion-symmetric topological insulators. *Phys. Rev. B* **83**, 245132 (2011).

[18] N. Rösch, Time-reversal symmetry, Kramers' degeneracy and the algebraic eigenvalue problem *chem. Phys.* **80**, 1-5 (1983).

[19] S. Lee, *et al*. Broken Kramers Degeneracy in Altermagnetic MnTe. *Phys. Rev. Lett.* **132**, 036702 (2024).

[20] R. Ramazashvili, Kramers degeneracy in a magnetic field and Zeeman spin-orbit coupling in antiferromagnetic conductors. *Phys. Rev. B* **79**, 184432 (2009).

[21] N. Sai, *et al.* Compositional Inversion Symmetry Breaking in Ferroelectric Perovskites. *Phys. Rev. Lett.* **84**, 5636-5639 (2000).

[22] M. P. Warusawithana, Asymmetric ferroelectricity by design in atomic-layer superlattices with broken inversion symmetry. *Phys. Rev. B* **104**, 085103 (2021).

doi:10.6342/NTU202404787

[23] S. Hashemizadeh, *et al.* Symmetry breaking in hexagonal and cubic polymorphs of BaTiO3. *J. Appl. Phys.* **119**, 094105 (2016).

[24] A. Karvounis, *et al.* Barium Titanate Nanostructures and Thin Films for Photonics. *Adv. Opt. Mater.* **8**, 2001249 (2020).

[25] P. Perna, *et al.* Interfacial exchange-coupling induced chiral symmetry breaking of spin-orbit effects. *Phys. Rev. B* **92**, 220422 (2015).

[26] Y. Fukaya, *et al.* Interorbital topological superconductivity in spin-orbit coupled superconductors with inversion symmetry breaking. *Phys. Rev. B* **97**, 174522 (2018).

[27] H. Ishizuka, & Y. Motome, Spontaneous spatial inversion symmetry breaking and spin Hall effect in a spin-ice double-exchange model. *Phys. Rev. B* **88**, 100402 (2013).

[28] Y. Zhou, *et al.* Topological Spin Textures: Basic Physics and Devices. *Adv. Mater.* 2312935 (2024).

[29] Bode, M. *et al.* Chiral magnetic order at surfaces driven by inversion asymmetry. *Nature,* **447**, 190-193 (2007).

[30] S. Mühlbauer, *et al.* Skyrmion Lattice in a Chiral Magnet. *Science* **323**, 915-919 (2009).

[31] J. S. W. Lamb, & J. A. G. Roberts, Time-reversal symmetry in dynamical systems: A survey. *Phys. D: Nonlinear Phenom.* **112**, 1-39 (1998).

[32] C. Herring, Effect of Time-Reversal Symmetry on Energy Bands of Crystals. *Phys. Rev.* **52**, 361-365 (1937).

[33] S. U. Piatrusha, *et al.*Topological Protection Brought to Light by the Time-Reversal Symmetry Breaking. *Phys. Rev. Lett.* **123**, 056801 (2019).

[34] S. Hayami, & H. Kusunose, Spin-orbital-momentum locking under odd-parity magnetic quadrupole ordering. *Phys. Rev. B* **104**, 045117 (2021).

doi:10.6342/NTU202404787

[35] C. Z. Chang, P. Wei, & J. S. Moodera, Breaking time reversal symmetry in topological insulators. *MRS Bull*. **39** (2014).

[36] I. N. Karnaukhov, Spontaneous breaking of time-reversal symmetry in topological insulators. *Phys. Lett. A* **381**, 1967-1970 (2017).

[37] C. Z. Chang, & M. Li, Quantum anomalous Hall effect in time-reversal-symmetry breaking topological insulators. *J. Phys.: Condens. Matter.* **28**, 123002 (2016).

[38] Y. Yang. *et al.* Time-Reversal-Symmetry-Broken Quantum Spin Hall Effect. *Phys. Rev. Lett.* **107**, 066602 (2011).

[39] X. L. Qi, & S. C. Zhang, The quantum spin Hall effect and topological insulators. *Phys. Today* **63**, 33–38 (2010).

[40] K. Sun, & E. Fradkin, Time-reversal symmetry breaking and spontaneous anomalous Hall effect in Fermi fluids. *Phys. Rev. B* **78**, 245122 (2008).

[41] L. Šmejkal *et al.* Crystal time-reversal symmetry breaking and spontaneous Hall effect in collinear antiferromagnets. *Sci. Adv.* **6**, eaaz8809 (2020).

[42] N. Stefanakis, Charge current in a ferromagnet-superconductor junction with the pairing state of broken time-reversal symmetry. *Phys. Rev. B* **64**, 224502 (2001).

[43] S. Das Sarma, & E.H. Hwang, Collective Modes of the Massless Dirac Plasma. *Phys. Rev. Lett.* **102**, 206412 (2009).

[44] N. P. Armitage, E. J. Mele, & A. Vishwanath, Weyl and Dirac semimetals in three-dimensional solids. *Rev. Mod. Phys.* **90**, 015001 (2018).

[45] O. Vafek, & A. Vishwanath, Dirac Fermions in Solids: From High-Tc Cuprates and Graphene to Topological Insulators and Weyl Semimetals. *Annu. Rev. Condens. Matter Phys.* **5**, 83-112 (2014).

[46] H. Weyl, Elektron und Gravitation. *Z. Phys.* **56**, 330–352 (1929).

[47] Y. Zhang, *et al.* First-principles study of the low-temperature charge density wave

doi:10.6342/NTU202404787

phase in the quasi-one-dimensional Weyl chiral compound. *Phys. Rev. B* **101**, 174106 (2020).

[48] S. M. Huang, *et al.* A Weyl Fermion semimetal with surface Fermi arcs in the transition metal monopnictide TaAs class. *Nat. Commun.* **6**, 7373 (2015).

[49] B. Q. Lv, *et al*. Observation of Weyl nodes in TaAs. *Nature Phys*. **11**, 724–727 (2015).

[50] C. C. Lee, *et al*. Fermi surface interconnectivity and topology in Weyl fermion semimetals TaAs, TaP, NbAs, and NbP. *Phys. Rev. B* **92**, 235104 (2015).

[51] N. W. Ashcroft & N. D. Mermin, *Solid State Physics*. (Chapter 17, Beyond the Independent Electron Approximation; Brooks/Cole Cengage Learning, Belmont USA, 1976)

[52] G. Y. Hu, & R. F. O'Connell, Generalization of the Lindhard dielectric function to include fluctuation effects. *Phys. Rev. B* **40**, 3600-3604 (1989).

[53] G. Grüner, *Density waves in solids* (Perseus Publishing, Cambridge, Massachusetts, 1994).

[54] K. Rossnagel. On the origin of charge-density waves in select layered transition-metal dichalcogenides. *J. Condens. Matter Phys.* **23**, 213001 (2011).

[55] C. Chen. *On the Nature of Charge Density Waves, Superconductivity and Their Interplay in 1T-TiSe2*. Springer Nature (2019).

[56] D. I. Khomskii. *Basic aspects of the quantum theory of solids: order and elementary excitations.* Cambridge University Press (2010).

[57] R. E. Peierls. *Quantum theory of solids*. oxford UP. London, England, (1955).

[58] S. Hellmann, *et al*. Ultrafast Melting of a Charge-Density Wave in the Mott Insulator 1T-TaS_2. *Phys. Rev. Lett.* **105**, 187401 (2010).

[59] H. Fröhlich. On the theory of superconductivity: the one-dimensional case.

doi:10.6342/NTU202404787

Proceedings of the Royal Society of London. Series A. Mathematical and Physical Sciences **223**, 296–305, (1954).

[60] E. J. Woll Jr & W. Kohn. Images of the Fermi surface in phonon spectra of metals. *Phys. Rev.* **126**, 1693 (1962).

[61] M. D. Johannes, I. I. Mazin, & C. A. Howells, Fermi-surface nesting and the origin of the chargedensity wave in NbSe2. *Phys. Rev. B* **73**, 205102 (2006).

[62] J. Bardeen, L. N. Cooper, & J. R. Schrieffer, Theory of superconductivity. *Phys. Rev.* **108**, 1175 (1957).

[63] W. L. McMillan, Transition temperature of strong-coupled superconductors. *Phys. Rev.* **167**, 331 (1968).

[64] W. L. McMillan, Collective modes of a charge-density wave near the lock-in transition. *Phys. Rev. B* **16**, 4655, (1977).

[65] B. I. Halperin, & T. M. Rice, Possible anomalies at a semimetal-semiconductor transistion. *Rev. Mod. Phys.* **40**, 755 (1968).

[66] I. Langmuir, *Proc. Nat. Acad. Sci* **14**, 627 (1926).

[67] D. Pines, *Elementary Excitations in Solids*, Benjamin (1964).

[68] D. Pines, & Ph. Nozieres, *The Theory of Quantum Liquids*, Benjamin (1966).

[69] H. Raether, *Excitations of Plasmons and Interband Transitions by Electrons*. (Springer-Verlag, Berlin Heidelberg New York, 1980).

[70] J. Hunt, EELS imaging and analysis school 2003.

[71] L. V. Keldysh, D. A. Kirshnits, & A. A. Maradudin, *The dielectric function of condensed systems*, North Holland (1989).

[72] M. Dressel, & G. Grüner, *Electrodynamics of Solids: Optical Properties of Electrons in Matter*. (CambridgeUniversity Press, Cambridge, 2002).

[73] P. Drude, Zur Elektronentheorie der Metalle. *Ann. Phys.* **306**, 566-613(1900).

doi:10.6342/NTU202404787

[74] M. Dressel, & M. Scheffler, Verifying the Drude response. *Ann. Phys.* **518**, 535-544 (2006).

[75] C, John. "Lorentz Oscillator Model". Brigham Young University, Department of Physics & Astronomy. Brigham Young University (2020).

[76] A. F. J. Levi, *The Lorentz oscillator model, Essential Classical Mechanics for Device Physics* (2016).

[77] C. F. Bohren, & D. R. Huffman, *Absorption and Scattering of Light by Small Particles* (Wiley, New York, 1983), Chap. 9.

[78] G. Botton, & J.C.H. Spence. *Science of microscopy* (Springer Science+Business Media, LLC, 2007).

[79] D. Stroppa, *et al*. High-Resolution Scanning Transmission Electron Microscopy (HRSTEM) Techniques: High-Resolution Imaging and Spectroscopy Side by Side. *Chemphyschem*. **13**, 437 (2012).

[80] C. Jeanguillaume, & C. Colliex, Spectrum-image: The next step in EELS digital acquisition and processing. *Ultramicroscopy* **28**, 252 (1989).

[81] G. Balossier *et al*. Parallel EELS elemental mapping in scanning transmission electron microscopy: use of the difference methods. *Microsc. Microanal. Microstruct.* **2**, 531 (1991).

[82] P.E. Batson, Simultaneous STEM imaging and electron-loss spectroscopy with atomic-column sensitivity. *Nature* **366**, 727 (1993).

[83] O. Scherzer Optil 2, 114 (1947).

[84] M.Haider *et al*. A spherical-aberration-corrected 200 kV transmission electron microscope. *Ultramicroscopy* **75**, 53 (1998).

[85] R. Leary, & R. Brydson. Chromatic Aberration Correction: The Next Step in Electron Microscopy. *Adv. Imaging Electron Phys.* **165**, 73-130 (2011).

doi:10.6342/NTU202404787

[86] B. DiBartolo, *et al*. Collective Excitation in Solids, *Nato ASI Series B* **88**, Plenum (1981).

[87] J. Fink, Recent Developments in Energy-Loss-Spectroscopy. *Adv. in Electronics and El. Physics*. **75**, Academic Press, (1985).

[88] S.E. Schnatterly, Inelastic electron scattering spectroscopy. *Solid State Physics* **34**, 275 (1979).

[89] S. Wang, *et al*. Pressure-induced superconductivity in the quasi-one-dimensional charge density wave material CuTe. *Phys. Rev. B* **103**, 134518 (2021).

[90] H. Zhong, *et al*. Hidden charge density wave induced shadow bands and ultrafast dynamics of CuTe investigated using time-resolved ARPES. *Phys. Rev. B* **109**, 165411 (2024).

[91] R. S. Li, *et al*. Optical spectroscopy and ultrafast pump-probe study of a quasi-one-dimensional charge density wave in CuTe. *Phys. Rev. B* **105**, 115102 (2022).

[92] X, Zhu, *et al*. Classification of charge density waves based on their nature. *Proc. Natl. Acad. Sci.* **112**, 2367-2371 (2015).

[93] M.D. Johannes, & II Mazin, Fermi surface nesting and the origin of charge density waves in metals. *Phys. Rev. B* **77,** 165135 (2008).

[94] M.D. Johannes, II Mazin, & C.A. Howells, Fermi-surface nesting and the origin of the charge-density wave in NbSe2. *Phys. Rev. B* **73**, 205102 (2006).

[95] C. N. Kuo, *et al*. Transport and thermal behavior of the charge density wave phase transition in CuTe. *Phys. Rev. B* **102**, 155137 (2020).

[96] K. Zhang, *et al*. Evidence for a Quasi-One-Dimensional Charge Density Wave in CuTe by Angle-Resolved Photoemission Spectroscopy. *Phys. Rev. Lett.* **121**,206402 (2018).

[97] K. Stolze, *et al*. CuTe: Remarkable Bonding Features as a Consequence of a Charge

doi:10.6342/NTU202404787

Density Wave. *Chem. Int. Ed.* **52**, 862 (2013).

[98] Tsui, Y. K. *et al*. Current direction dependent magnetotransport in CuTe. *Phys. Rev. B* **108**, 115162 (2023).

[99] M. Nord, *et al*. Atomap: a new software tool for the automated analysis of atomic resolution images using two-dimensional Gaussian fitting. *Adv Struct Chem Imag.* **3**, 9 (2017).

[100] J.M. LeBeau, *et al*. Standardless atom counting in scanning transmission electron microscopy. *Nano. Lett.* **10**, 4405–4408 (2010).

[101] S.M. Anthony, & S. Granick, Image analysis with rapid and accurate two-dimensional Gaussian fitting. *Langmuir* **25**, 8152–8160 (2009).

[102] S. Kim, B. Kim, & K. Kim, Role of Coulomb correlations in the charge density wave of CuTe. *Phys. Rev. B* **100**, 054112 (2019).

[103] N. N. Quyen, *et al*. Three-dimensional ultrafast charge-density-wave dynamics in CuTe. *Nat. Commun.* **15**, 2386 (2024).

[104] S. Wang, *et al*. Observation of room-temperature amplitude mode in quasi-one-dimensional charge-density-wave material CuTe. *Appl. Phys. Lett.* **120**, 151902 (2022).

[105] K. Stolze, *et al*. CuTe: Remarkable Bonding Features as a Consequence of a Charge Density Wave. *Chem. Int. Ed.* **52**, 862 (2013).

[106] P. Cudazzo, & L. Wirtz, Collective electronic excitations in charge density wave systems: The case of CuTe. *Phys. Rev. B* **104**, 125101 (2021).

[107] E. Runge. & E. K. U. Gross, Density-function theory for time-dependent systems. *Phys. Rev. Lett.* **52**, 997 (1984).

[108] G. Onida, L. Reining, & A. Rubio, Electronic excitations: density-functional versus many-body Green's-function approached. *Rev. Mod. Phys.* **74**, 601 (2002).

doi:10.6342/NTU202404787

[109] W. Kohn, & L. J. Sham, Self-consistent equations including exchange and correlation effects. *Phys. Rev.* **140**, A1133 (1965).

[110] M. Campetella, *et al*. Electron-phonon driven charge density wave in CuTe. *Phys. Rev. B* **108**, 024304 (2023).

[111] S. Pezzini, *et al*. Unconventional mass enhancement around the Dirac nodal loop in ZrSiS. *Nat. Phys.* **14**, 178-183 (2018).

[112] Y. Shao, *et al*. Electronic correlations in nodal-line semimetals. *Nat. Phys.* **16**, 636 (2020).

[113] P. M. latzman, & P. A. Wolff, *Waves and Interactions in Solid State Plasma*. (Academic Press, New York and London, 1973).

[114] Z. Lin, *et al*. Dramatic plasmon response to the charge-density-wave gap development in 1T-$TiSe_2$. *Phys. Rev. Lett.* **129**, 187601 (2022).

[115] G. Li, *et al*. Anomalous metallic state of $Cu_{0.07}TiSe_2$: an optical spectroscopy study. *Phys. Rev. Lett.* **99,** 167002 (2007).

[116] P. Lambin, J. P. Vigneron, & A. Lucas, Computation of the surface electron-energy-loss spectrum in specular geometry for an arbitrary plane-stratified medium. *Comput. Phys. Commun*. **60**, 351 (1990).

[117] G. Campagnoli, *et al*. Plasmon behavior at the charge-density-wave onset in 2H-$TaSe_2$. *Phys. Rev. B* **20**, 2217-2227 (1979).

[118] N. Nücker, *et al*. Long-wavelength collective excitations of charge carriers in high-Tc superconductors. *Phys. Rev. B* **44**, 7155-7158 (1991).

[119] A. Politano, *et al*. 3D Dirac plasmons in the type-II Dirac semimetal $PtTe_2$. *Phys. Rev. Lett.* **121**, 086804 (2018).

[120] S. Xue, *et al*. Observation of nodal-line plasmons in ZrSiS. *Phys. Rev. Lett.* **127**, 186802 (2021).

doi:10.6342/NTU202404787

[121] N. Nücker, *et al*. Plasmons and interband transitions in $Bi_2Sr_2CaCu_2O_8$. *Phys. Rev. B* **39**, 12379-12382 (1989).

[122] Sing, M. et al. Plasmon excitations in quasi-one-dimensional $K_{0.3}MoO_3$. *Phys. Rev. B* 59, 5414-5425 (1999)

[123] A. Kogar, *et al*. Signatures of exciton condensation in a transition metal dichalcogenide. *Science* **358**, 1314-1317 (2017).

[124] R. Schuster, *et al*. Negative plasmon dispersion in the transition-metal dichalcogenide 2H-$TaSe_2$. *Phys. Rev. B* **79**, 045134 (2009).

[125] J. Van Wezel, *et al*. Effect of charge order on the plasmon dispersion in t ransition-metal dichalcogenides. *Phys. Rev. Lett.* **107**, 176404 (2011).

[126] P. Cudazzo, M. Gatti, & A. Rubio, Plasmon dispersion in layered transition-metal dichalcogenides. *Phys. Rev. B* **86**, 075121 (2012).

[127] P. Cudazzo, *et al*. Negative plasmon dispersion in 2H-NbS_2 beyond the charge-density-wave interpretation. *New J. Phys.* **18**, 103050 (2016).

[128] M. Sing, *et al*. Unusual plasmon dispersion in the quasi-one-dimensional conductor (TaSe4)2I: experiment and theory. *Phys. Rev. B* **57**, 12768-12771 (1998).

[129] N. Nücker, *et al*. Symmetry of holes in high-T_c superconductors. *Phys. Rev. B* **36**, 6619 (1989).

[130] S Das Sarma, & Hwang, E. H. Collective modes of the massless Dirac plasma. *Phys. Rev. Lett.* **102**, 206412 (2009).

[131] L. P. He, *et al*. Quantum transport evidence for the three-dimensional Dirac semimetal phase in Cd3As2. *Phys. Rev. Lett.* **113**, 246402 (2014).

[132] D. C. Elias, *et al*. Dirac cones reshaped by interaction effects in suspended graphene. *Nat. Phys.* **7**, 701-704 (2011).

[133] Reimer, L. *Transmission Electron Microscopy* (Chapter 7, Theory of Electron

doi:10.6342/NTU202404787

Diffraction; 4th edition, Springer, Berlin, 1997).

[134]K.A. Mkhoyan, *et al*. Separation of bulk and surface-losses in low-loss EELS measurements in STEM. *Ultramicroscopy* **107**, 345-355 (2006).

[135]A. Gloter, *et al*. Improving energy resolution of EELS spectra: an alternative to the monochromator solution. *Ultramicroscopy* **96**, 385-400 (2003).

[136] K. Ishizuka, K. Kimoto, & Y. Bando, Improving energy resolution of EELS spectra by deconvolution using maximum-entropy and Richardson-Lucy algorithms. *Microsc. Microanal.* **9** (Suppl. 2), 832-833 (2003).

[137] S. A. Kivelson, *et al*. How to detect fluctuating stripes in the high-temperature superconductors. *Rev. Mod. Phys*. **75**, 1201-1241 (2003).

[138] C. Monney, *et al*. Dramatic effective mass reduction driven by a strong potential of competing periodicity. *Europhysics Lett*. **92**, 47003 (2010).

[139] M, Imada, A. Fujimori, & Y. Tokura, Metal-insulator transitions. *Rev. Mod. Phys.* **70**, 1039-1263 (1998).

[140] I. C. Lin, *et al*. Atomic-scale observation of spontaneous hole doping and concomitant lattice instabilities in strained nickelate films. *New J. Phys*. **24**, 023011 (2022).

[141]M. -W. Chu, *et al*. Probing charge order and hidden topology at the atomic scale by cryogenic scanning transmission electron microscopy and spectroscopy. *Phys. Rev. B* **103**, 115130 (2021).

[142]C.-P. Chang, *et al*. Atomic-scale observation of a graded polar discontinuity and a localized two-dimensional electron density at an insulating oxide interface. *Phys. Rev. B* **87**, 075129 (2013).

[143] P.-W. Lee, *et al*. Hidden lattice instabilities as origin of the conductive interface between insulating $LaAlO_3$ and $SrTiO_3$. *Nat. Commun.* **7**, 12773 (2016).

doi:10.6342/NTU202404787

[144]K. Lyon, *et al*. Theory of magnon diffuse scattering in scanning transmission electron microscopy. *Phys. Rev. B* **104,** 214418 (2021).

[145] B. G. Mendis, Quantum theory of magnon excitation by high energy electron beams. *Ultramicroscopy* **239**, 113548 (2022).

[146] J. A. Do Nascimento, *et al*. Theory of momentum-resolved magnon electron energy loss spectra: the case of yttrium iron garnet. Preprint at https://doi.org/10.48550/arXiv.2401.12302 (2024)

doi:10.6342/NTU202404787